Treatment planning strategies for proton therapy in the presence of a cranial fixation clip

Master Thesis Biomedical Engineering

Iris Kuitems

Treatment planning strategies for proton therapy in the presence of a cranial fixation clip

by

Iris Kuitems

To obtain the degree of Master of Science at the Delft University of Technology, to be defended publicly on Tuesday December 12, 2023 at 15:00 PM.

Thesis committee:		
	Dr. A.L. Wolf,	HollandPTC, supervisor
	Prof. Dr. M.S. Hoogeman,	TU Delft, supervisor
	Dr. Ir. D. Lathouwers,	TU Delft, committee member

Cover: The Flapfix fixation system produced by DePuy Synthes, the orthopedics company of Johnson & Johnson

Preface

Iris Kuitems
Delft, December 2023

This thesis outlines the project conducted at HollandPTC for the Master Biomedical Engineering, track Medical Physics, at Delft University of Technology.

I want to thank the supervisors of my project. A special thanks to Anne Lisa Wolf for her guidance during the entire project and for making this project possible. Thank you for regularly allocating time for meetings, for assisting me in determining the right way forward, and for consistent patience throughout the entire process. Also, I would like to thank Mischa Hoogeman. I appreciate your thoughtful questions and insights that assisted in guiding the project.

Additionally, I would like to thank the employees of the R&D department; Marta Rovituso, Ernst van der Wal, and Thomas Toet. With a special thanks to Marta, who guided me with the experiments. I appreciate the explanations, which have enhanced my understanding and contributed to my learning process and the development of this work.

Furthermore, I would like to thank the KFM department. Specifically Paul van Beers, who dedicated a lot of time to assisting me with the experiments. Also, he brought valuable contributions to the preparation and methodology of the study.

Finally, thanks to my family, friends, and Caspar for being there and helping out when needed.

Summary

Purpose: Metal implants create dosimetric uncertainties in treatment planning and delivery for proton therapy. The purpose of this thesis is to determine the most suitable treatment planning strategy for proton therapy in the presence of cranial fixation clips.

Literature review: Prior to this thesis, a literature review was conducted to gain a broader understanding of the effects of metal implants on proton therapy and to determine what treatment planning strategies are applied. The four main concepts that were identified to have potential effectiveness in addressing cranial fixation clips for brain cancer were: implementing a density override on the implant, employing either a single-field optimization (SFO) or multi-field optimization (MFO) technique, implementing beam-specific margins or not, and adding an avoidance margin on the implant.

Methodology: A phantom was designed and imaged using computed tomography. Subsequently, base experiments were performed on a mono-energetic proton beamline to investigate the dose perturbation caused by the clip and determine the experimental setup and methods to be employed for the experiments performed on the clinical treatment gantry. It was found that the presence of the clip in the radiation field created by a 150 MeV mono-energetic proton beam produces a measurable signal perturbation: a signal reduction caused by the clip was detected, along with a local signal elevation, created by the sharp edges of the clip. The uniformity of the field was reduced by 1 to 2% for most experimental setups. It was concluded that the Lynx detector was the most suitable to use in the experiments in this thesis: it has a high submillimeter resolution and allows for quick, on-site analysis.

The second set of experiments investigated a total of seven different planning strategies, based on the four main concepts identified from the literature review. All strategies, except for the one including an avoidance margin around the implant, were successfully implemented into the treatment planning system Raystation. The plans were robustly optimized (±3mm / ±3% uncertainty) and met the clinical goals regarding clinical target volume (CTV) coverage (at least 98% of the target volume receives 95% of the maximum dose (47.88 Gy)) and organ at risk (OAR) sparing (as low as reasonably achievable). The experiments were conducted in a clinical treatment room by irradiating the phantom and measuring the signal at 3 depths inside a spherical CTV and distal to the CTV, inside an OAR.

Results: The measured signal in the CTV was evaluated by extracting line profiles through the center of the field. The data from the treatment planning system (TPS) presented a high, uniform signal at all depths throughout the CTV. From the measured signals from the experimental data, it was found that the signal levels decreased at greater depths. Additionally, for all strategies, the homogeneity index (HI) calculated from the experimental data was worse than the TPS data and differed per measured depth. The average calculated HI was best at 10 mm (mean HI = 0.98), and decreased when measured at 30 mm (mean HI = 0.86), and 50 mm depth (mean HI = 0.89). The strategies employing MFO techniques produced a more inhomogeneous signal in the CTV than those employing SFO methods. Furthermore, when evaluating the measurements inside the OAR, it was found that in the strategies that employed an MFO technique were best able to spare the OAR.

Conclusion Based on the results of the conducted experiments, there is a strong indication that the field homogeneity inside the target volume gets perturbed by the clip. This indicates a high need to investigate the clinical implications of this further. The main limitation of this project is that the Lynx detector was currently not able to detect the measured signal in dose in Gray. Therefore, further work should elaborate on using detection methods for absolute dosimetry.

Contents

Appendices

1

Introduction

1.1. Brain cancer treatment

Brain cancer is a complicated disease that is not yet fully understood. Every year, approximately 1400 people in the Netherlands are diagnosed with brain cancer [1]. The disease can emerge from a primary tumor, which is a benign or malignant tumor that arises from within the brain tissue itself, or from a secondary tumor, which are metastases from cancer in another part of the body [2], [3]. There are over 120 distinct kinds of brain tumors [2], [4]. A few of the most prevalent ones are depicted in Figure 1.1. Diagnoses can be difficult since their related symptoms, such as headaches or cognitive impairments, are frequently linked to milder, non-cancerous diseases [5]. After the patient's diagnosis, the appropriate treatment method is determined. Treating brain cancer provides several challenges, primarily because it is a vital organ and due to the diverse range of tumor types [6], [7]. Often, a combination of different treatment modalities is applied, which may include surgery, radiation therapy, or chemotherapy.

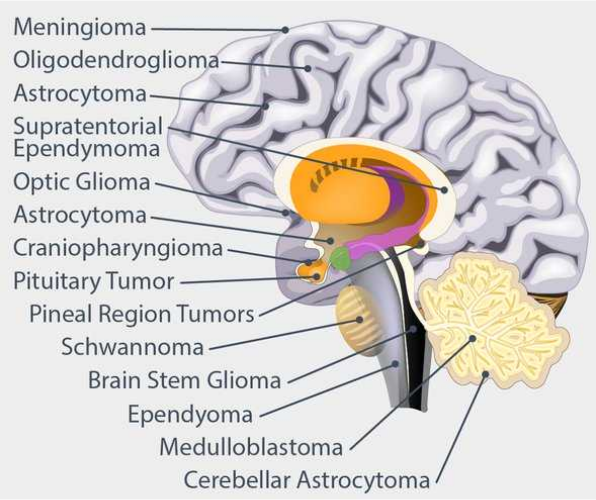

Figure 1.1: An overview of the most common types of brain tumors [4].

The majority of patients first undergo brain surgery to resect the brain tumor [8]. During surgery, a craniotomy is performed, involving the creation of a small aperture in the skull to expose the brain tissue. Hereafter, the skull requires fixation, achieved by utilizing a fixation device consisting of metal components [9], [10]. Figure 1.2 illustrates such a fixation device: the Flapfix fixation system produced by DePuy Synthes, the orthopedics company of Johnson & Johnson. This implant will serve as the main focus of this thesis. Hereafter, it will be referred to as 'clip'. More information on the clip and the detailed material compositions is presented in Section 3.1.

Figure 1.2: The Flapfix Cranial Fixation Clip, manufactured by DePuy Synthes, a Johnson & Johnson company.

Radiation therapy can be applied as the main treatment modality or as a palliative treatment method to relieve a patient's symptoms. Additionally, it is often used as an additional treatment method to kill the remaining cancer cells not removed during surgery. [11]. Therefore, radiation therapy is a crucial component in brain tumor treatment. Radiation therapy has been a great objective of research in the scientific and medical fields, with ongoing developments to the present day. Recent progress in radiation methods, such as intensity-modulated radiotherapy (IMRT) and volumetric-modulated arc therapy (VMAT), enable the administration of increased radiation doses to the tumor tissue while decreasing the radiation dose to healthy tissues [12].

In addition to the conventional types of radiation therapy, which are applied by the usage of photon irradiation, proton therapy can be used as an alternative type of external radiation treatment. The main difference between proton and photon therapy relies on the difference in dose distribution. In photon therapy, the photons that traverse the tissue, are gradually decelerated, whereby the dose is administered to all cells along the beam path. This affects also the healthy, non-cancerous tissues. In proton therapy, on the other hand, the particle's energy is released toward the end of its trajectory, leading to the absence of an exit dose. Due to this, the healthy tissue distal from the tumor is better preserved. An image of the difference between a photon and proton therapy treatment plan is provided in Figure 1.3. Further explanation of the specific characteristics of proton therapy is provided in Chapter 2.

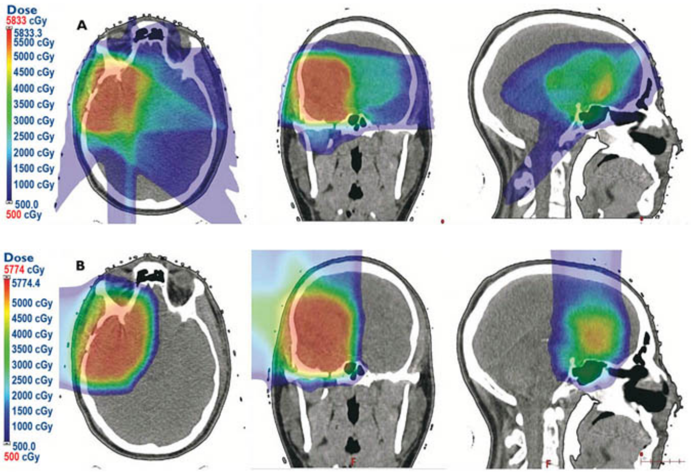

Figure 1.3: Figure 1.3a, presents an IMRT photon therapy treatment plan. Figure 1.3b presents a pencil beam scanning proton therapy treatment plan [13].

When surgery is followed by proton therapy, metal cranial fixation clips can be present in the radiation field. The effects of metal implants on proton therapy have been a topic of research in the past decades. Researchers have shown that metal implants inside the body can lead to artifacts or distortions for imaging purposes, mainly when computed tomography (CT) is being used. Artifacts occur primarily around the implants and cause inaccuracies in determining the size and geometry of the implant [14], [15], [16], [17]. Subsequently, this leads to clinical uncertainties and errors in the delineation of the clinical target volume (CTV) and organs at risk (OARs) [14], [18]. Additionally, the implants cause problems in the dose calculation process because the interactions with the proton beam and the implant are not always incorporated into the dose calculation system [16], [17]. This can result in an underdose of the CTV and treatment failure or an overdose of the OARs and unnecessary side effects. This indicates a need to understand the impact of metal implants on proton therapy.

1.2. Goal and objectives

The presence of metal surgical fixation clips presents a challenge in treatment planning and delivery for proton therapy due to dosimetric uncertainties. Therefore, the main goal of this thesis is to determine the most appropriate treatment planning strategy for patients with these metal implants.

The following research question will guide the investigation in this thesis: What is a suitable treatment planning strategy for proton therapy in the presence of a cranial fixation clip?

To answer this question, the following subquestions will be addressed:

1. What treatment planning strategies are used for proton therapy in the presence of metal implants?
2. What is the agreement between the prescribed dose from the treatment planning system and the signal measured in the experiments?
3. What are the dosimetric consequences of the usage of these strategies for the clinical target volume and organs at risk?

The first subquestion will be answered through a comprehensive literature review, attached in Appendix A. This literature review will present an overview of the general characteristics of proton therapy and the effects of metal implants in general. Hereafter, the currently applied strategies for delivering proton therapy to patients with metal implants will be evaluated. The second and third subquestions are evaluated in this thesis. Different treatment planning strategies will be created, and experiments will be conducted to assess the most adequate way to incorporate the cranial fixation clip into the treatment plan. The thesis will focus on developing a treatment strategy that can be applied with pencil beam scanning proton therapy in combination with robust optimization methods.

1.3. Format of thesis

First, in Chapter 2, relevant background information for this thesis is provided. Hereafter, in Chapter 3, the process of designing a phantom for the experiments will be described. The phantom will mimic a clinical situation in which a clip is placed on a patient's skull. Additionally, imaging of the phantom will be performed to determine sufficient imaging protocol and create an adequate measurement setup for the following experiments. After this, an investigation of the clip's effect on the proton's irradiation field is presented in Chapter 4. This is researched by conducting experiments on the phantom. The aim is to assess the influence of the clip on the dose distribution within and surrounding the field. Based on these base experiments, the methodology and experimental setup for the last experiments will be determined. The second set of experiments, presented in Chapter 5, will investigate several planning strategies. The main goals of these experiments are twofold. First, the aim was to find the most adequate treatment planning strategy regarding treatment outcomes; optimizing the dose to the CTV and minimizing the dose to an OAR. Secondly, the dose calculated by the treatment planning system (TPS) was compared to the signal measured in the experiments to gain information on how the TPS can incorporate the dose perturbations caused by the clip. Hereafter, in Chapter 7, a discussion is outlined, involving the interpretations, implications, and limitations of this work. Thereafter, recommendations for future research and a conclusion are presented.

2

Background Information

As a preparation for this thesis, a literature review was written, attached to Appendix A. In part 1 of the literature review, the basic principles of proton therapy are explained, and in part 2, strategies to handle metal implants are investigated. This chapter elaborates on the most relevant aspects of the literature review for this thesis. First, a small introduction to the research facility where this thesis is conducted is presented. After that follows an explanation of the basic principles of proton therapy. Finally, the contribution of the literature review to the determination of the strategies is highlighted.

2.1. Holland Particle Therapy Centre

This study is conducted at Holland Particle Therapy Centre (HollandPTC). This is an outpatient facility located in Delft, where patients are treated for cancer with proton therapy. At HollandPTC, a cyclotron is present that is able to accelerate the protons, which are retrieved from hydrogen atoms, to energies in the range of 70 MeV to 250 MeV. The protons are transported from the cyclotron to the treatment rooms via large steering magnets. In each treatment room, a treatment gantry is present. This is the beam delivery system, which can rotate up to 360 degrees. This allows it to rotate around the patient and irradiate from various angles. In addition to patient care, HollandPTC focuses on conducting scientific research. The building facilitates an R&D bunker, in which a fixed beamline is present. Here, only experiments are conducted, and no patients are treated. An overview of the layout of a multiroom system, developed by Varian [19], is depicted in figure 2.1. The cyclotron is shown in the right room, the other rooms serve as treatment rooms. In this thesis, experiments are performed in both the treatment room and the R&D facility.

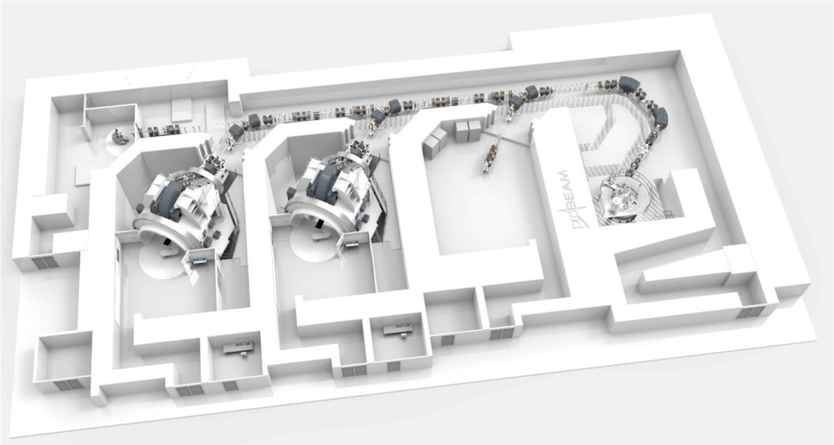

Figure 2.1: The layout of a multiroom system developed by Varian, a Siemens Healthineers company. The cyclotron is in the far-right room, the other rooms serve as treatment rooms [19].

2.2. Basic principles of proton therapy

This section explains the basic physical principles of proton therapy as additional information already provided in the literature review. Proton therapy is a type of ionizing radiation. It relies on the interaction of the protons with the medium they traverse through. As the particles traverse a medium, they will gradually lose their energy, whereby the goal is to damage the cancerous cells and spare normal tissue. How the particles decelerate and lose their energy can be characterized by their stopping power, which can be described in a simplified way as

$$\frac{S}{\rho} = -\frac{\mathrm{d}E}{\rho \mathrm{dx}}, \tag{2.1}$$

where S is the stopping power, ρ is the density of the material the protons traverse through, E the energy, and x the traveled distance [20]. As can be derived from the equation, the energy and traveled distance are inversely related. Furthermore, the density of the medium also impacts the energy distribution, with a higher-density medium leading to an earlier energy deposition than a lower-density medium.

Several theories have investigated the stopping power in the context of radiation therapy. One of these theories focuses on approximating the stopping power by making assumptions about the energy ranges and materials applicable in proton therapy. The Bethe equation presents this as

$$-\frac{\mathrm{d}E}{\mathrm{d}x} = \frac{4\pi n z^2}{m_e c^2 \beta^2}\left(\frac{e^2}{4\pi\epsilon_0}\right)^2\left(ln\frac{2m_e c^2\beta^2}{I(1-\beta^2)} - \beta^2\right), \tag{2.2}$$

where n is the medium's electron density, e and m_e are the electron charge and mass respectively, I is the mean ionization energy of the medium, z is the multiple of electron charge, β is described as v/c with v being the speed of the projectile and c the speed of light in a vacuum, and ϵ_0 the vacuum permittivity [21].

The parameters presented in equation 2.2 describe how the protons will dissipate their energy when they travel through the medium. From the formula, the stopping power increases as the protons slow down in the medium. This pertains to the characteristic Bragg curve, depicted in Figure 2.2a, which relates the deposition of the proton's energy to the traveled distance [21]. The figure shows that the highest amount of energy is deposited in the last part of the trajectory, also called the Bragg Peak. Adding multiple Bragg Peaks results in a spread-out Bragg peak (SOBP), as depicted in Figure 2.2b. This is useful when aiming to deposit energy over a larger area, as in cancer therapy.

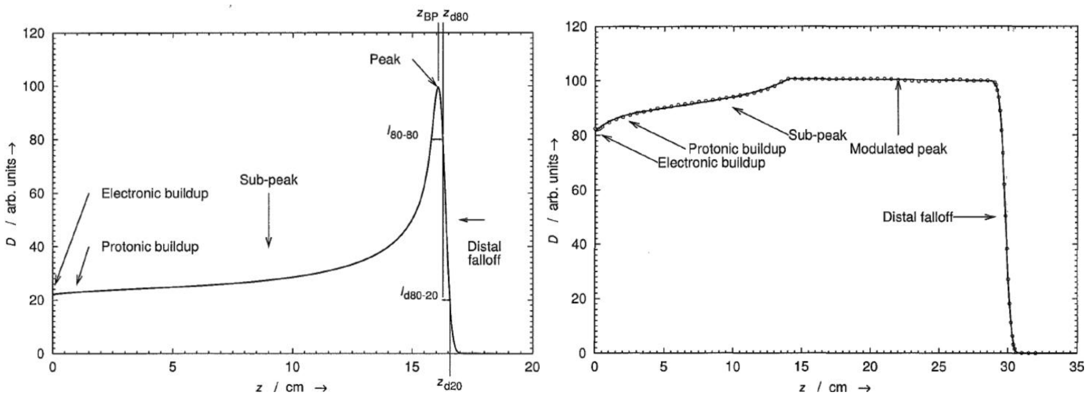

(a) **(b)**

Figure 2.2: In figure 2.2a, the characteristic Bragg curve is depicted, and in figure 2.2b a visualisation of the SOBP. The graphs are displayed as absorbed dose with respect to depth [21].

Proton therapy at HollandPTC is delivered by using Pencil Beam Scanning (PBS) techniques. This method uses small pencil beams to irradiate the target layer by layer. Here, the pencil beams are modulated, by which the location and intensity of the beams can be precisely adjusted, which provides high accuracy levels [22].

2.3. Strategies to manage metal implants

As was enlightened in Chapter 1 and the literature review, the presence of metal implants in the radiation field presents several uncertainties. One challenge impacting the CT imaging process is the occurrence of artifacts, which can lead to inaccuracies in the delineation process. Another challenge arises from the interactions of protons with implants, which are not consistently integrated into the dose calculation algorithm. If these issues are not appropriately addressed, this could lead to under- or overdosage of tissue, potentially resulting in treatment failure.

The literature review aimed to outline various strategies that address these uncertainties for metal implants in general. In this thesis, the investigation will focus on strategies that exhibited potential effectiveness in addressing cranial fixation clips for brain cancer. This includes the following strategies: applying density overrides to the implant material, adding an avoidance margin around the implant, the usage of beam-specific adjustments and the comparison between different optimization techniques.

2.3.1. Density overrides

A technique focussing on managing implants in the radiation field is using a material overwrite on the implant's material. This technique was adopted in several of the included articles in the literature review [23], [24], [25], [26], [27], [28], [29], [30], [31], [32]. The main goal of applying a density override is to ensure a more accurate dose calculation in the treatment planning process. Proton therapy dose calculation relies on the conversion of Hounsfield units (HU) from the CT scan to relative stopping power. If the implant is not correctly imaged due to for example artifacts, partial volume effect, or intensity saturation, the dose calculation will be performed based on incorrect stopping power. Articles included in the literature review showed that including density override provides better modeling of the interactions with the implant and subsequently a more accurate treatment plan. Therefore, this approach is implemented in some of the strategies investigated in this thesis.

2.3.2. Avoidance of implant

Another technique that was presented in the literature review as a way to manage metal implants in the radiation field is by avoiding the implant [24], [28], [30], [33], [34]. This can be implemented by preventing the beam from entering directly through the implant. Additionally, considering an avoidance margin around the entire implant through which the beam is not allowed to pass could be an extension of this approach. The objective of this technique is to accommodate for setup uncertainties. Articles in the review included this technique in their approach and showed successful results. The articles presented in the review included research on breast cancer, prostate cancer, or experimental studies on phantoms. However, it must be noted that this approach depends on the type and location of the cancer being treated and the ability to choose beam angles that can avoid the implant.

This approach is incorporated into the treatment planning strategies in this thesis; in the setup of the beam geometry, it is aimed to avoid the incidence of the beams crossing the implants. In addition to this, a treatment planning strategy in which an avoidance margin around the implant is set will be applied.

2.3.3. Beam-specific margins

Another approach that will be included in this thesis is the application of beam-specific margins [27]. The aim of this method is to include the range uncertainty only locally around the clip and not in the entire plan. This is done by creating a shadow area in the beam line that crosses the implant and expanding the CTV with a margin dependent on the amount of implant it traverses. This approach is applied in the current clinical practice at HollandPTC and will be further investigated in this thesis.

2.3.4. Optimization techniques

Single-field and multi-field optimization

Articles included in the literature review also focussed on investigating different optimization techniques in the presence of a metal implant within the radiation field [24], [26], [30], [16]. In the case of a multibeam treatment plan, there are two ways for optimization: single-field optimization (SFO) and multi-field optimization (MFO) [22]. When using an SFO technique, the treatment plan is optimized by creating a uniform dose for the target with every single field. This means that the optimization of one field does not depend on the optimization of the other field(s). This makes this technique more robust against setup and range uncertainties. However, this also makes it less capable of sparing OARs. When using MFO techniques, all beams in the treatment plan are optimized simultaneously. Therefore, throughout the optimization process, the optimization of one beam is based on the optimization of other beams. This allows for more modulation, making it better capable of sparing OARs. However, the inhomogeneous dose distribution also results in an increased sensitivity to setup and range errors. The choice of using an SFO or MFO technique is based on the complexity of the target volume, clinical goals for the target and OARs, and the presence of implants can influence the choice of optimization technique. This thesis incorporated both SFO and MFO techniques into different treatment planning strategies.

Robust Optimization

In addition to SFO and MFO techniques, there are other optimization methods that can be applied during proton therapy treatment planning. As was emphasized by the literature review, the success of proton therapy treatment delivery relies on accurately determining the proton's range and properly managing setup uncertainties [35]. Range uncertainties can arise when converting the HU from the CT scan to the stopping power during dose calculation. Additionally, artifacts and anatomical variations can cause range errors, and the uncertainties introduced by the presence of metal implants further complicate the correct prediction of the proton's range [36], [24], [37]. Setup uncertainties primarily arise during the patient setup process and due to anatomical variations [35]. These uncertainties impact the correct delivery of proton therapy and introduce challenges in the treatment planning procedure.

The literature review highlights a technique that aims to incorporate range and setup uncertainties during treatment planning: robust optimization [26], [38], [24], [32], [28], [31], [23], [16], [33], [30]. This technique computes deviations from the nominal treatment plan, which incorporates potential errors [39], [40], [25]. The setup uncertainties are calculated by defining a setup error, which is the maximum distance that the isocenter can shift for each scenario. By including isotropic setup uncertainties, 21 error scenarios are computed. The range uncertainty is incorporated into the optimization as a maximum density shift. After the optimization process, the scenarios are evaluated.

In this thesis, an evaluation protocol will be followed to evaluate the robust optimization. This protocol is in accordance with the Dutch Proton Therapy group guidelines [41]. A total of 28 scenarios are evaluated, resulting from adding positive and negative range error scenarios to the setup error scenarios [41]. To evaluate the clinical goals of the treatment plan, the voxelwise minimum and maximum scenarios can be analyzed. The voxelwise minimum scenario includes the minimum dose value per scenario for each voxel, and the voxel-wise maximum scenario includes the maximum dose value. The voxelwise minimum is used to assess the dose in the target area, while the voxelwise maximum is used to evaluate the dose in the neighboring tissues and organs at risk. Applying robust optimization and evaluation creates treatment plans that are robust against the predefined range and setup uncertainties. This method is incorporated into all treatment planning strategies in this thesis.

3

Designing the Phantom and Imaging

This chapter is divided into two subsections. First, the process of designing the phantom is described. Thereafter, the imaging procedure is explained.

3.1. Designing the phantom

The experiments in this thesis are performed on a phantom. The primary objective was to design a phantom that mimics the characteristics of a human brain with a surrounding layer resembling the skull. Additionally, it must be ensured that the clip can be attached to the skull layer.

Brain tissue equivalent material

The human brain is primarily composed of water (approximately 80%) [42]. Therefore, to resemble the brain tissue, it was chosen to use the water-equivalent material RW3. This is a white polystyrene that is commercially available [43], [44] and often used for dosimetric purposes [45], [46]. The RW3 slabs have a density of 1.045 g/cm^3. This closely resembles the average density of brain tissue which is 1.046 g/cm^3 [47]. A total of ten 1 cm thick RW3 slabs with a 30 x 30 cm^2 area were placed on top of each other to create a 10 x 30 x 30 cm^3 volume.

Skull equivalent material

The skull is mimicked by using a slab of skull-equivalent material with the properties of cortical bone (Gammex). The water equivalent thickness (WET) of the slab is ±1.6 cm, which resembles the cortical bone's WET value of 1.704 cm. The slab has a 20 x 20 cm^2 surface and is 1 cm thick. This is slightly thicker than an average human skull (6.5 mm for men and 7.1 mm for women [48]).

Clip

There exist several different types of cranial fixation systems. In this thesis, the Flapfix cranial fixation system produced by DePuy Synthes, the Orthopaedics company of Johnson & Johnson is investigated.

Composition

The clip is composed of a titanium alloy. The exact composition of the clip was requested from Johnson & Johnson and is depicted in figure 3.1. The clip that is researched in this thesis is classified as grade 4. The mass density of the material is 4.51 g/cm^3 [49].

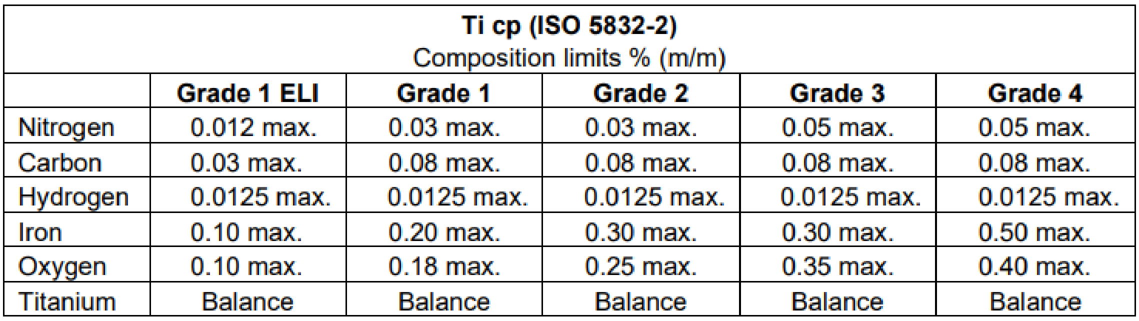

Ti cp (ISO 5832-2) Composition limits % (m/m)					
	Grade 1 ELI	**Grade 1**	**Grade 2**	**Grade 3**	**Grade 4**
Nitrogen	0.012 max.	0.03 max.	0.03 max.	0.05 max.	0.05 max.
Carbon	0.03 max.	0.08 max.	0.08 max.	0.08 max.	0.08 max.
Hydrogen	0.0125 max.	0.0125 max.	0.0125 max.	0.0125 max.	0.0125 max.
Iron	0.10 max.	0.20 max.	0.30 max.	0.30 max.	0.50 max.
Oxygen	0.10 max.	0.18 max.	0.25 max.	0.35 max.	0.40 max.
Titanium	Balance	Balance	Balance	Balance	Balance

Figure 3.1: The flapfix cranial fixation clip that is used in this thesis is classified under Titanium cp (commercially pure) Grade 4 (source: DePuy Synthes, a Johnson & Johnson company).

Dimensions and components
The clip consists of 3 main components: two disks connected with a hollow pin. The bottom disk is positioned underneath the skull and can have a textured surface to provide friction for stability. The pin connects the bottom and top disk and is placed in between two parts of the skull. During surgery, the extending part of the pin is cut off, so that it does not protrude the skin. The top disk is placed on the outer surface of the skull. It has a flower-shaped design, which enables the implant to conform to the shape of the skull.

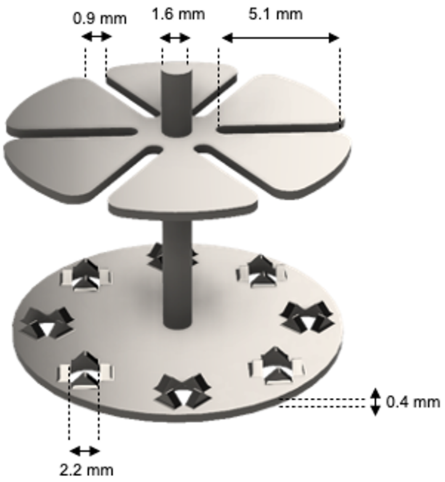

Figure 3.2: A digital drawing of the cranial fixation clip with corresponding dimensions.

Configurations
There are several different types of Flapfix Cranial Fixation system clips, with a distinction in shape and size: 11, 13, 18, and 22 mm diameter are available. Next to that, some clips have a textured, and others have a non-textured surface. The clip used for these experiments has a diameter of 18 mm and has a bottom disk with a textured surface.

Final design

The final design of the phantom is depicted in figure 3.3. In the skull equivalent slab, a ± 1.8 mm diameter hole is drilled. Through this hole, the clip can be attached. The pin of the clip was cut off, just like in the clinical situation.

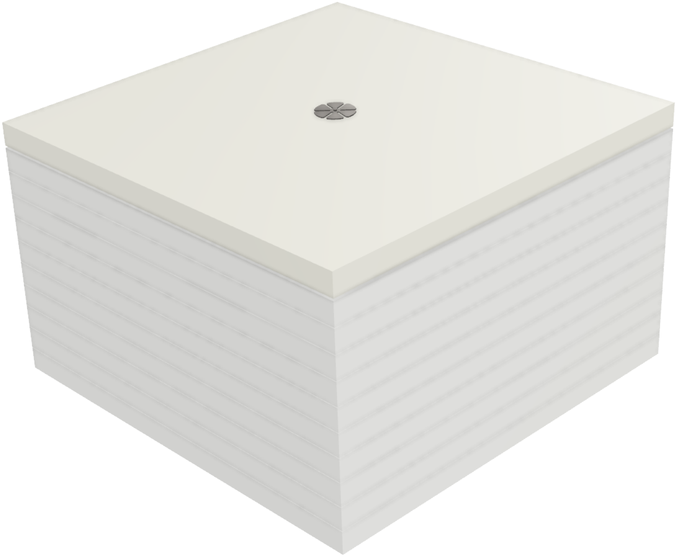

Figure 3.3: A digital drawing of the phantom. On the top slab, the clip is attached. Beneath that, several layers of RW3 slabs are placed.

3.2. Imaging

All imaging in this thesis was performed by using CT. In clinical practice, CT is used as the main imaging modality to perform treatment planning, because most treatment planning systems depend on the HU scale in this imaging system to perform dose calculation [50]. As an addition to CT, Magnetic Resonance Imaging (MRI) can be used to provide enhanced tissue contrast, so more accurate delineation of anatomical structures is possible [51]. Since this was not necessary for this project, the usage of CT was considered to be sufficient.

3.2.1. Experimental setup

A Siemens SOMATOM Definition Edge scanner was used to make the CT scans. Reconstruction of the scans was performed by using a soft-tissue kernel (Qr40). The phantom was placed at different positions and angles, to determine the appropriate setup for the experiments conducted in this thesis. Additionally, different scans were made to determine the appropriate scanning protocol and artifact correction algorithm.

Positioning of phantom

In the experiments, the phantom will be placed in the treatment gantry or at the fixed research beamline. The gantry is able to rotate and irradiate the phantom from different angles. The phantom must be irradiated from the side with the skull equivalent slab and clip to mimic a clinical situation. Additionally, there must be enough space for the detector to be positioned on the table, behind the phantom. The phantom was therefore placed on its side at the center of the CT scanner as depicted in figure 3.4.

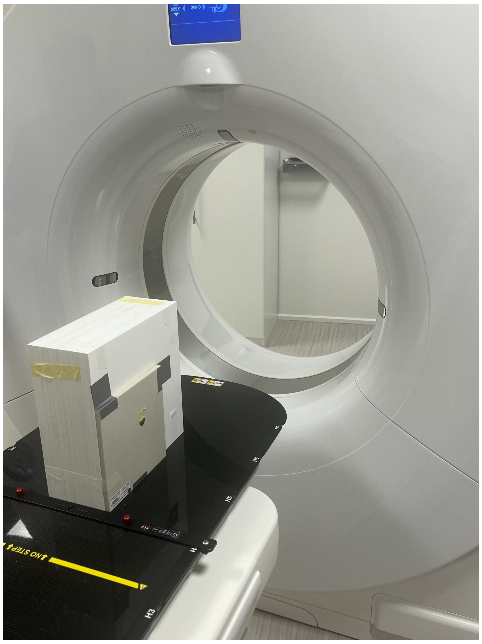

Figure 3.4: Visualization of the phantom's positioning during CT imaging.

3.2.2. Scanning protocol

Three different in-house scanning protocols were applied:

1. LWK protocol: LWK stands for *Lumbale Wervelkolom*, translated to lumbar spine.
2. KNO protocol: KNO stands for *Keel-Neus-Oo*r, translated to throat, nose, and ear.
3. Neuro protocol: used for neurology patients.

The main difference between these protocols is the slice thickness of the acquisition. The LWK protocol scans with a slice thickness of 3 mm, the KNO protocol with 2 mm, and the Neuro protocol with 1 mm.

In figure 3.5, the top and bottom disks of the pin are displayed when the scans were made according to different scanning protocols, and an iterative Metal Artifact Reduction (iMAR) algorithm was used for all three scans. These figures were made with a window/level preset setting of bone (W/L: 450/1600). In the left column, a Neuro scanning protocol was used. This results in a clear image, where the shape of the clip is evidently visible. When measuring the length of the clip according to the presets of Figure 3.5, this results in a diameter of 18.3 mm, which closely matches the actual dimensions of the clip (18 mm). For the other two protocols, the quality of the image degrades quickly, and measuring the diameter of the clip becomes more difficult and inaccurate: 19.6 mm for the KNO protocol and 20.1 mm for the LWK protocol.

An explanation of the reduction in quality can be the occurrence of the partial volume effect. This is the phenomenon that occurs when imaging an object that is smaller than the resolution of the imaging system [52]. In CT, every pixel corresponds to one HU value. This value is assigned, according to the attenuation of the object that is being imaged. If one pixel consists of more than one type of material, the corresponding HU value is displayed by an average of the HU values, corresponding to the different types of matter. This results in less detail and makes it difficult to distinguish different objects. The partial volume effect increases when the voxel dimensions exceed the dimensions of the object being imaged. This explains why this effect is more prominent in protocols with a lower resolution [53]. Based on these results, the Neuro scanning protocol will be used for the experiments.

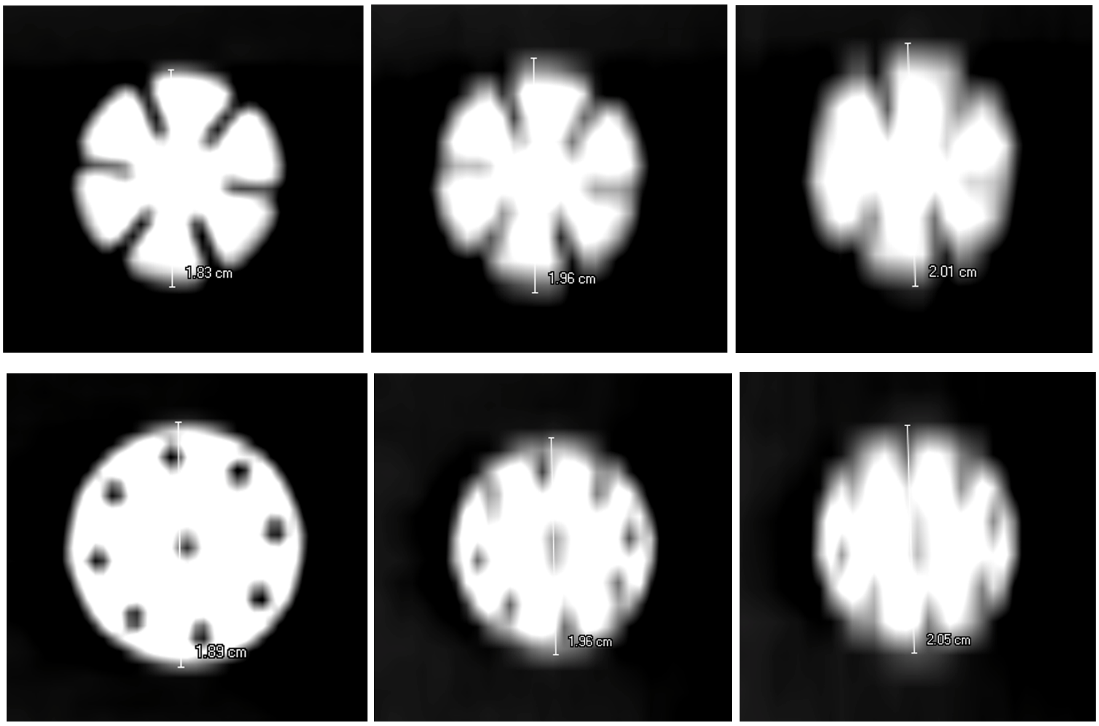

(a) Neuro **(b)** KNO **(c)** LWK

Figure 3.5: On the top row, the top disk of the clip is displayed, and on the bottom row the bottom disk. The resolution decreases from 1 mm for the neuro protocol, to 2 mm for the KNO protocol to 3 mm for the LWK protocol. This goes at the expense of image quality.

3.2.3. Metal induced artifacts

To correct for possible artifacts created by the clip, an iterative Metal Artifact Reduction (iMAR) algorithm was applied (Siemens). Two scans were acquired; one with and one without an artifact reduction algorithm. The algorithm that was used was the iMAR correction for extremities implants [54].
The two scans are depicted in figure 3.6. Distal from the pin, an artifact caused by the clip is visible. As is visible in Figure 3.6a, the size of the artifact is minimally reduced by the iMAR algorithm. The difference in measured HU values between an iMAR and non-iMAR CT scan is depicted in Table 3.1. The difference in HU values in the RW3 plate was measured in one slice and the comparison was made between a 0.1 cm^3 area directly distal from the clip and 1 cm next to that, see Figure 3.6.

From the table, it is observed that the addition of the algorithm does not result in a reduction of the artifact. A potential cause for this observation is the underlying working principle of the algorithm: the ability of the algorithm to correct for artifacts is on one hand based on the implants's composition and dimensions. Furthermore, the patient's size and anatomical structures present in the image play a role in the working principle. Since this scan is performed on a phantom without differences in tissue densities and anatomical structures, this could possibly decrease the effectiveness of the artifact reduction algorithm [54].

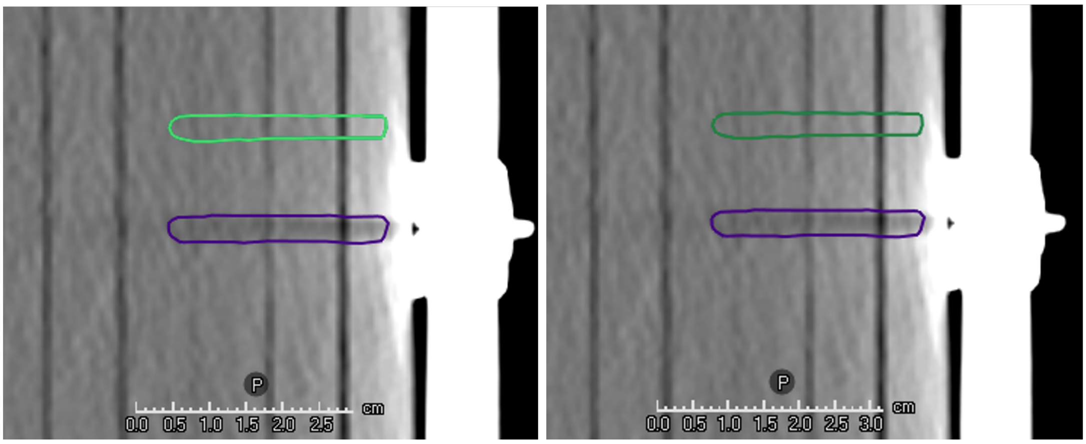

(a) With iMAR algorithm (EI) **(b)** Without iMAR algotithm

Figure 3.6: Figure 3.6a represents a CT scan with an iMAR algorithm and figure 3.6b without iMAR algorithm. In both scans, artifacts remain visible. The purple delineation covers the area of the artifact and the green delineation covers an artifact-free area.

Table 3.1: Comparison between HU values in an iMAR and non-iMAR CT. The area of the artifact is compared to an artifact-free area.

	Min Intensity [HU]	Average Intensity [HU]	Max Intensity [HU]
Without iMAR: artifact area	-113	26.33	136
Without iMAR: artifact-free area	-75	47.48	151
With iMAR: artifact area	-116	26.09	139
With iMAR: artifact-free area	-78	47.48	151

Another way to correct metal-induced artifacts is by applying a density override to the material that is affected by the artifacts. The recommendation at HollandPTC is to always apply a density override to an artifact when the difference in HU value at the artifact compared to the expected HU value is larger than 100 HU. When the difference lies between 50-100 HU, one should consider if a density override is necessary. A consideration here may be the size of the artifact. From Table 3.1, is observed that the difference lies in a range lower than 50-100 HU. The further away from the clip, the smaller this difference becomes. Since the area of the artifact does affect the position where the CTV will be delineated (further explanation on this in Section 5.2.2) and the size of the artifact will cover a substantial part of the CTV, it was decided to apply a density override on the RW3 plates. The density override that was applied contains a mass density of 1.045 [g/cm^3].

4

Dose perturbation caused by the clip

This chapter is written with the goal of identifying the dose perturbation caused by the presence of a cranial fixation clip in the proton beams radiation field. This was accomplished by investigating multiple experimental setups and using three different types of dose detection methods: the Lynx detector, the OCTAVIUS 1500XDR detector, and radiochromic films. The outcomes of these experiments will determine the experimental setup and methods to be employed in the second set of experiments, presented in Chapter 5.

4.1. Experimental method

All experiments presented in this chapter are conducted in the R&D facility at HollandPTC. At this facility, a stationary horizontal proton beamline is present, supplying a proton pencil beam with energy levels from 70 MeV to 250 MeV. The experiments are conducted using a 150 MeV mono-energetic proton beam, with a dose rate of 1.5 Gy/min.

A graphical representation of the experimental setup is depicted in Figure 4.1. The proton beam first traverses a scattering foil and a beam monitor. Hereafter, a dual-ring passive scattering system was placed (in the figure presented as ‘thick ring’), which creates a uniform dose field [55].

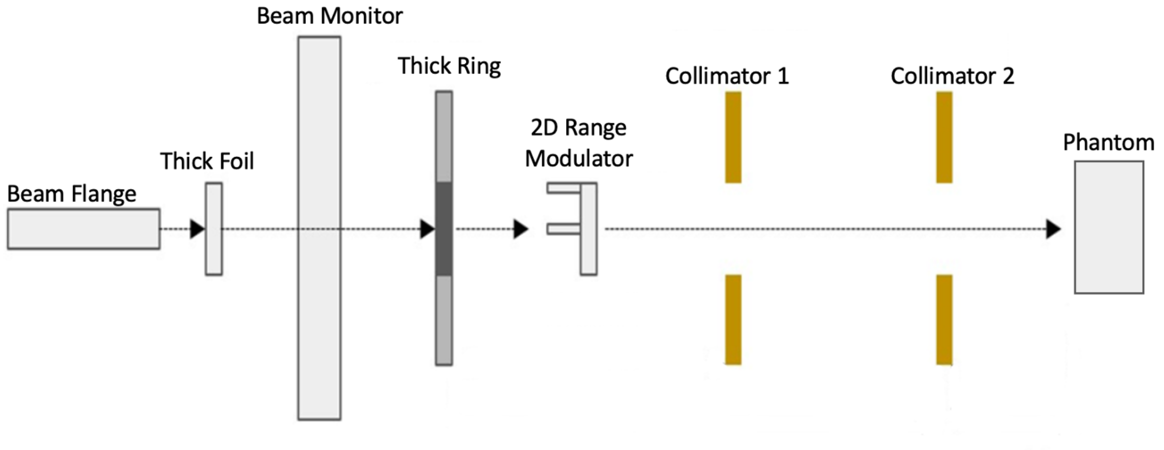

Figure 4.1: The setup that was utilized in the conducted experiments in the experimental bunker. The protons leave the exit window on the left and traverse the setup from left to right [55].

A 2D range modulator was positioned behind the ring, with the aim of creating a spread-out Bragg Peak (SOBP). Figure 4.2 illustrates an example of a 2D range modulator, as described by Holm et al. [56]. The working principle is as follows: a mono-energetic beam is directed towards the modulator, which comprises multiple pins shaped like pyramids. Due to its shape, protons crossing the material will traverse varying amount of distances. Protons that traverse through the entire pyramid, will decelerate more than protons that will travel only through the base of the pyramid. This consequently affects the range of each proton. The summation of all protons will create an SOBP. The 2D range modulator used in the experiments was custom-made for the facility and has a similar working principle. The uniformity of the established SOBP for the experimental setup in this thesis was previously characterized and is assumed to be 98±1% [55].

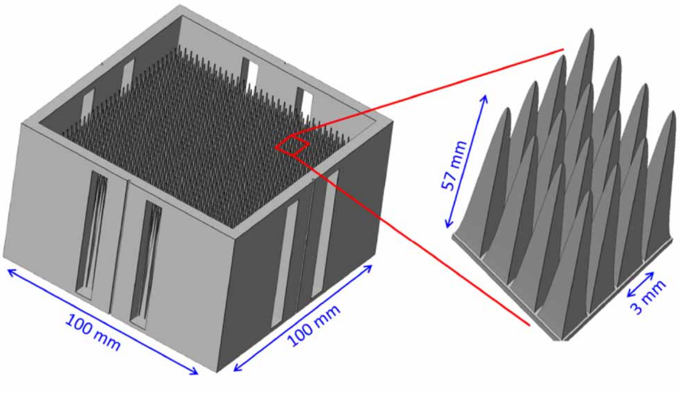

Figure 4.2: A 2D range modulator [56].

After passing the 2D range modulator, the beam traverses a square collimator, creating a 10 x 10 cm^2 field. This field will cover a sufficiently large part of the phantom presented in Section 3.1. An image of the experimental setup, containing the collimator, phantom, and detector is depicted in figure 4.3.

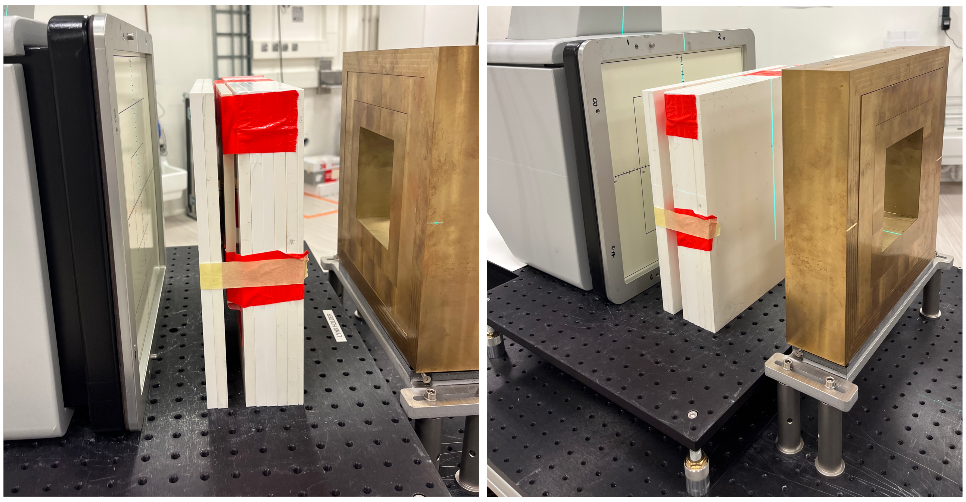
(a) (b)

Figure 4.3: This image captures the experimental setup used in one of the experiments. The proton beam passes the collimator on the right before it traverses the phantom. Preceding the beam's passage through the phantom, there are 55 mm of RW3 slabs in front of the phantom and 20 mm of RW3 slabs after the phantom. On the left, the Lynx detector is positioned.

As the proton beam traverses the phantom, the protons will decelerate, following the characteristic Bragg curve presented in Figure 4.4. This depth dose distribution was previously characterized for the experimental setup used in this thesis [55]. The experiments aimed to determine whether placing the clip at varying positions along the Bragg curve would lead to different effects on the dose distribution. To achieve this, varying amounts of RW3 slabs are placed in front of and after the phantom, effectively shifting the clip's location along the Bragg curve.

When determining the clip's location along the Bragg curve, an important note to make is that the phantom also consists of a plate of bone-equivalent material, which has a WET value of ±1.6 cm.

Therefore an additional 1.6 cm needs to be added to the position of the phantom when shifting the clip's location along the Bragg curve.

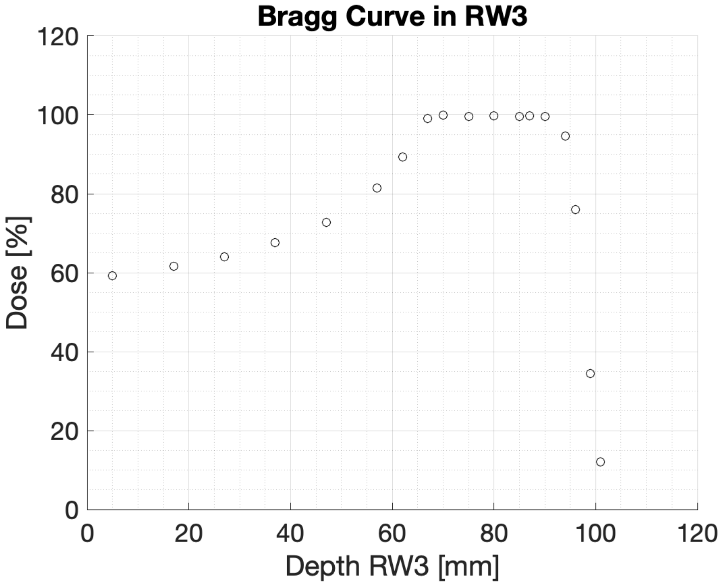

Figure 4.4: The Bragg curve of a fixed proton beam line measured in RW3. The curve is normalized with respect to the maximum value [55].

4.1.1. Lynx detector

The first detector selected for the experiments was the Lynx detector, primarily chosen for its high 0.5 mm resolution. A picture of the used Lynx Detector (IBA Dosimetry [57]) is displayed in Figure 4.5a. The Lynx detector is a detector that can be used for machine quality assurance in proton therapy. It consists of a scintillating screen that transfers the energy from the proton beam into photons, which subsequently are detected by a CCD camera [57]. This detector can measure the beam's width, range, and uniformity [58]. Russo et al. [59], investigated the linearity of the detector in a research where they characterized the Lynx detector for 2D dosimetry. Their research showed a linear correlation between the number of protons and the retrieved signal, dependent on the iris aperture setting. This setting must be set prior to each measurement. The iris represents a collimator system, which can be set to determine the light that will be received by the CCD camera [59]. Additionally, to correct for background noise, the detector has a built-in background correction system, which automatically corrects for background noise prior to each measurement.

The detector's signal is characterized by a 10-bit digitization depth. This means that the measured signal can be digitized into 1024 different signal levels. The digitization depth affects the resolution of the measured signal and therefore introduces an uncertainty margin. The detector presents its output as 2-dimensional data, which was analyzed using Matlab. An advantage of the Lynx detector is that it allows for quick analysis: the data from the detector can be transferred to the computer and analyzed directly by using the provided Lynx software. A downside of this detector is that it does not provide output in terms of dose in Gray but as a signal intensity value.

4.1.2. OCTAVIUS 1500XDR detector

The second detector that was selected for the experiments was the OCTAVIUS detector 1500XDR (PTW Dosimetry [60]). The detector is depicted in Figure 4.5b. The detector has a 27 x 27 cm^2 matrix design, consisting of ionization chambers [60]. It has a resolution of 5 mm and can provide signal output in terms of dose in Gray. The Octavius detector presents its output as 2-dimensional data and allows for quick, on-site analysis, just like the Lynx detector. After the experiments, the data is analyzed using Matlab. In the experiments that involved the OCTAVIUS detector, the phantom was irradiated for 60 seconds, leading to a total dose of 1.5 Gy (considering the dose rate is 1.5 Gy/min).

4.1.3. Gafchromic films

Gafchromic films (EBT3 [61]) are often used in dosimetry and have a very fine resolution (0.2 mm [62]). The films are thin and flat sheets that react to ionizing radiation. The process relies on chemical reactions inside the films; the films consist of crystals made out of monomers. When exposed to irradiation, the monomers are polymerized, which results in a darker appearance of the films. The amount of polymerization is directly dependent on the applied dose [61], [63]. After irradiation, the films can be digitized by using a scanning system (EPSON Expression 12000XL(USB) scanner)). The colorization can be detected by the scanning system and evaluated with the Epson Scan 2 software program. After this, the images can be processed and analyzed which is done by using ImageJ.

To evaluate the outcomes in terms of dosage in Gray, the results need to be calibrated. For the calibration, nine film sheets were previously irradiated with varying dose levels between 0.5 and 10 Gy to create a calibration curve. An important note to make is that the films that are irradiated for calibration, are taken from the same batch as the films used for the measurements to avoid differences between batches. Additionally, the timeframe between irradiation and scanning of the films should be kept constant for the calibration films and the films used in the experiments[64]. The calibration graph used for the experiments is provided in Appendix C. After calibration, each film provides a 2-dimensional representation of the dose distribution.

Film dosimetry also presents several disadvantages. A downside is that the films cannot be analyzed directly after the experiments, but that it requires additional time and workload. The films will continue to undergo coloration, even after radiation, which can introduce significant inaccuracies [64]. Additionally, the films are characterized by a linear-energy transfer (LET) dependent reaction, which is often accompanied by a quenching effect. This is the phenomenon in which a non-linear response occurs for low-energy protons [65].

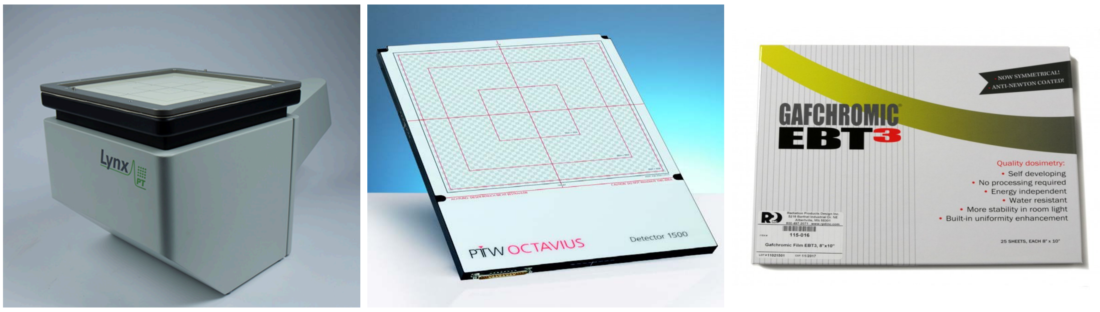

(a) (b) (c)

Figure 4.5: Figure 4.5a: Lynx detector [57], Figure 4.5b: OCTAVIUS detector [60], and Figure 4.5c: Gafchromic films [61].

4.1.4. Analysis

To get a better understanding of how the presence of the clip affects the radiation field, the field uniformity is investigated. This is calculated by using the following equation:

$$\text{Uniformity} = 100\% \cdot \frac{I_{\text{max}} - I_{\text{min}}}{I_{\text{max}} + I_{\text{min}}}, \tag{4.1}$$

in which I_{max} represents the maximum intensity in the measured field and I_{min} the minimum intensity. An example of a 2D dose graph is provided in figure 4.6a. The signal uniformity is measured within a specific radius around the center of the field, in either the x- or y direction. It is calculated by comparing the intensities over this range. In the absence of the clip, the uniformity in the field is measured to be 98±1% [55]. In order to assess the uniformity in the presence of the clip, a range of plus and minus 50 mm around the clip is evaluated. Note that the clip in the experiments is always placed in the field's center unless stated otherwise. An example of a line profile along the x- and y-direction is presented in Figure 4.6b. The graphs are normalized to the maximum measured value. This will be done for all graphs presented in this Chapter unless stated otherwise.

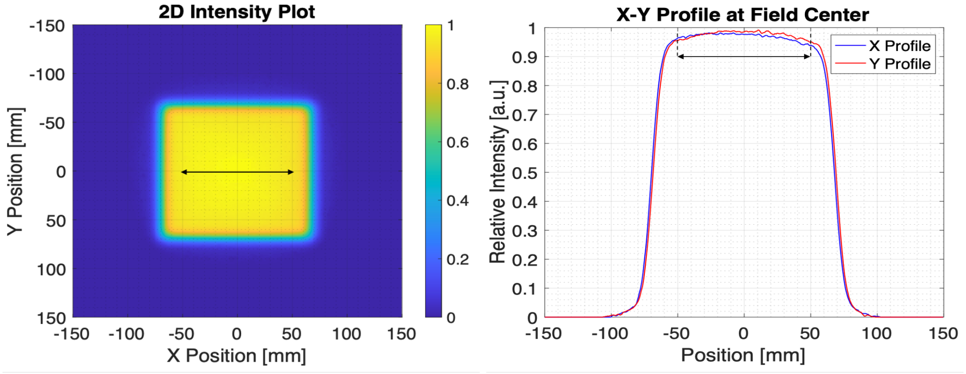

(a) (b)

Figure 4.6: Figure 4.6a depicts an example of a 2D dose graph when no clip is presented. Figure 4.6b visualizes a line profile along the x- and y-direction, in a cross-section without a clip.

In the next sections, the results of the conducted experiments are presented. The first evaluation covers experiments using the Lynx detector. Hereafter follows an assessment of the OCTAVIUS detector. Lastly, an examination of the experiments involving Gafchromic films is presented.

4.2. Base experiments

To start with, three base experiments were conducted to analyze if the presence of the clip in the radiation field leads to a measurable effect. In these experiments, the clip was attached to the skull equivalent material plate and positioned on the table in the R&D room. Proximal to the skull equivalent plate, a diverse range of RW3 plates were positioned, consisting of a total thickness of 55, 60, or 70 mm RW3. Behind the RW3 plates and bone-equivalent plate, at the distal end, the Lynx detector was placed. In this way, the dose is measured at different depths along the plateau of the SOBP.

The results of the first experiments are presented in Figure 4.7. All graphs in the figures are normalized to their maximum value. As is visible in the 2D graphs, a signal reduction is visible in the field center. Line profiles through the field center are extracted and presented. The uniformity along the line profiles is calculated and presented in Table 4.1. As can be observed, the clip causes a reduction in field uniformity of about 1-2 %

In base experiment 3, a larger uniformity reduction is found in comparison to the other two experiments. A possible cause for this is that the clip and detector were placed after 70 mm of RW3 plates, shifting it to the distal end of the SOBP. This results in an overall lower intensity signal, both at the clip's location and in the region surrounding the clip. This is displayed in Figure 4.8, where the line profiles along the x-direction are plotted without applying normalization. In the following experiments, this effect was further investigated.

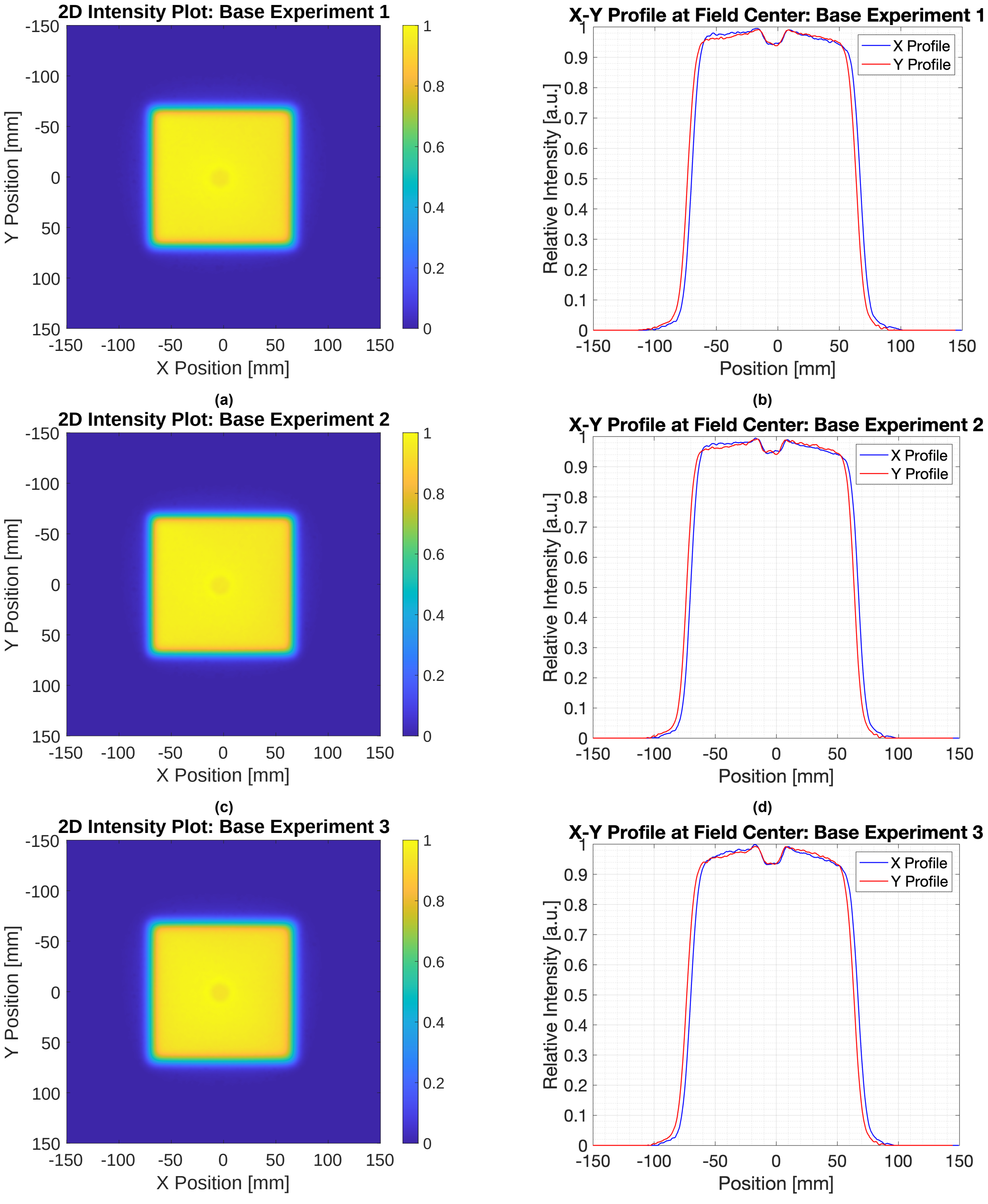

(a) (b) (c) (d) (e) (f)

Figure 4.7: Overview of the results of the base experiments. In the left column, the 2D intensity plots are visible, and in the right column, the line profiles through the field's center. In figure 4.7a and 4.7b, 55 mm of RW3 plates were positioned before the clip and bone equivalent material. In Figure 4.7c and 4.7d, the addition of RW3 plates added up to 60 mm and in figure 4.7e and 4.7f this was 70 mm. In all graphs, a dose reduction at the field's center is measured.

Table 4.1: Uniformity along x- and y-direction for the base experiments.

	Base exp 1	Base exp 2	Base exp 3
Configuration: RW3 before clip [mm]	55	60	70
Uniformity x direction [%]	97.3	97.2	96.4
Uniformity y direction [%]	97.2	97.4	96.9

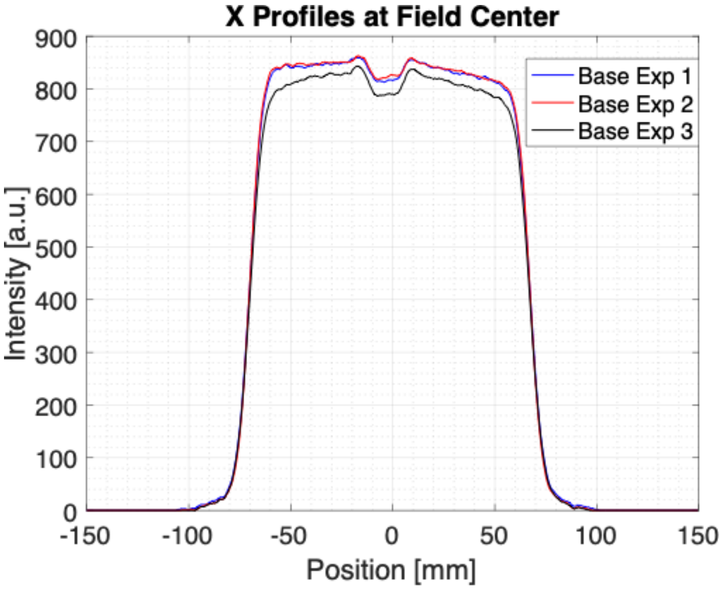

Figure 4.8: Line profiles along the y-direction for all three base experiments. A signal reduction caused by the clip is present in all profiles. An overall signal reduction is observed for base experiment 3.

In Figure 4.9, the y-profile through the center of the field of base experiment 2 is displayed. The black asterisks represent the geometrical boundaries of the clip, i.e. the center of the field ± 9 mm. As is visible, the observed dip in the intensity approximates the dimensions of the clip. An elevation in intensity is visible on the boundary sites. This is probably caused by multiple Coulomb scattering at the sharp edges of the clip [66], [67]. This creates difficulties in the dose calculation process since modeling of the Coulomb scattered particles is not well incorporated into dose calculation algorithms [68], [69]. This problem is elaborated on in the literature review, see Appendix A.

Additionally, in the middle of the field, at the supposed center point of the clip, a small intensity elevation is visible. This was not evenly pronounced in every experiment, see Figure 4.7. It was questioned why this effect occurred and whether this was caused by the pin that is situated in between the disks of the clip, or if it was merely a distortion in the radiation field or an artifact. The following experiments seek to find an answer to this question.

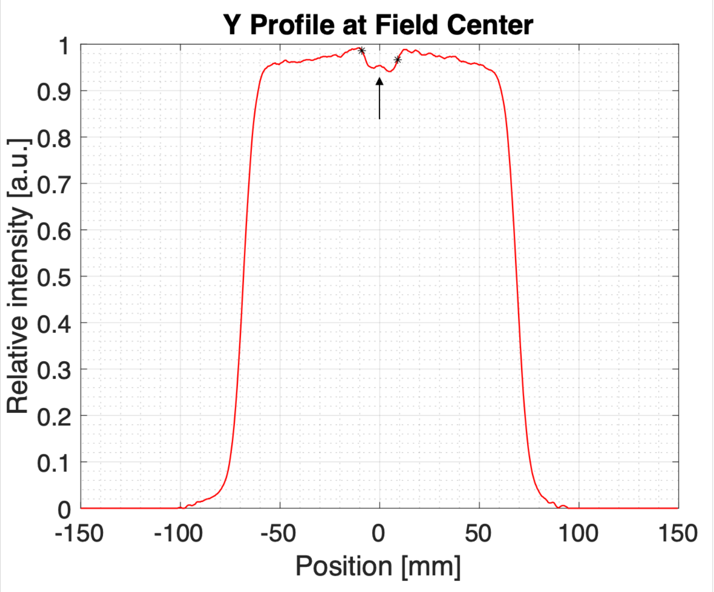

Figure 4.9: The black asterisks represent the geometrical boundaries of the clip; i.e. the center of the field ± 9 mm. The black arrow points out an elevation in the center of the clip. The cause of this elevation is further investigated in the following experiments.

4.3. Clinical scenario experiments

In the next experiments, several scenarios were investigated, which involved the placement of RW3 slabs both before and after the clip. This was done to explore a more clinical situation, where the region of interest, i.e. the tumor, is not located directly distal to the clip, but further away. Additionally, by varying the amount of RW3 plates in front of and after the clip, it was investigated if the location of the clip with respect to the SOBP influences the amount of field perturbation.

Table 4.2, provides an overview of the different configurations per scenario and their corresponding uniformity values across line profiles drawn through the center of the irradiation field. The reduction in field uniformity remains constant at a value of ±1% for all experimental setups, except for scenario 2.5. This phenomenon was previously observed in Base Experiment 3. The 2D intensity plot and line profiles through the center of the radiation field for scenarios 2.1 and 2.5 are depicted in Figure 4.10. An overview of the 2D intensity plots and line profiles for the other experiments is provided in Appendix B.

Table 4.2: Uniformity along x- and y-direction for the clinical scenario experiments.

Scenario	**1**	**2.1**	**2.2**	**2.3**	**2.4**	**2.5**	**3**
RW3 before clip [mm]	10	55	55	55	55	55	40
RW3 after clip [mm]	60	1	2	5	10	20	20
Uniformity x direction [%]	96.9	97.0	97.2	97.2	96.9	90.4	97.0
Uniformity y direction [%]	97.4	97.3	97.2	97.1	97.4	91.1	97.3

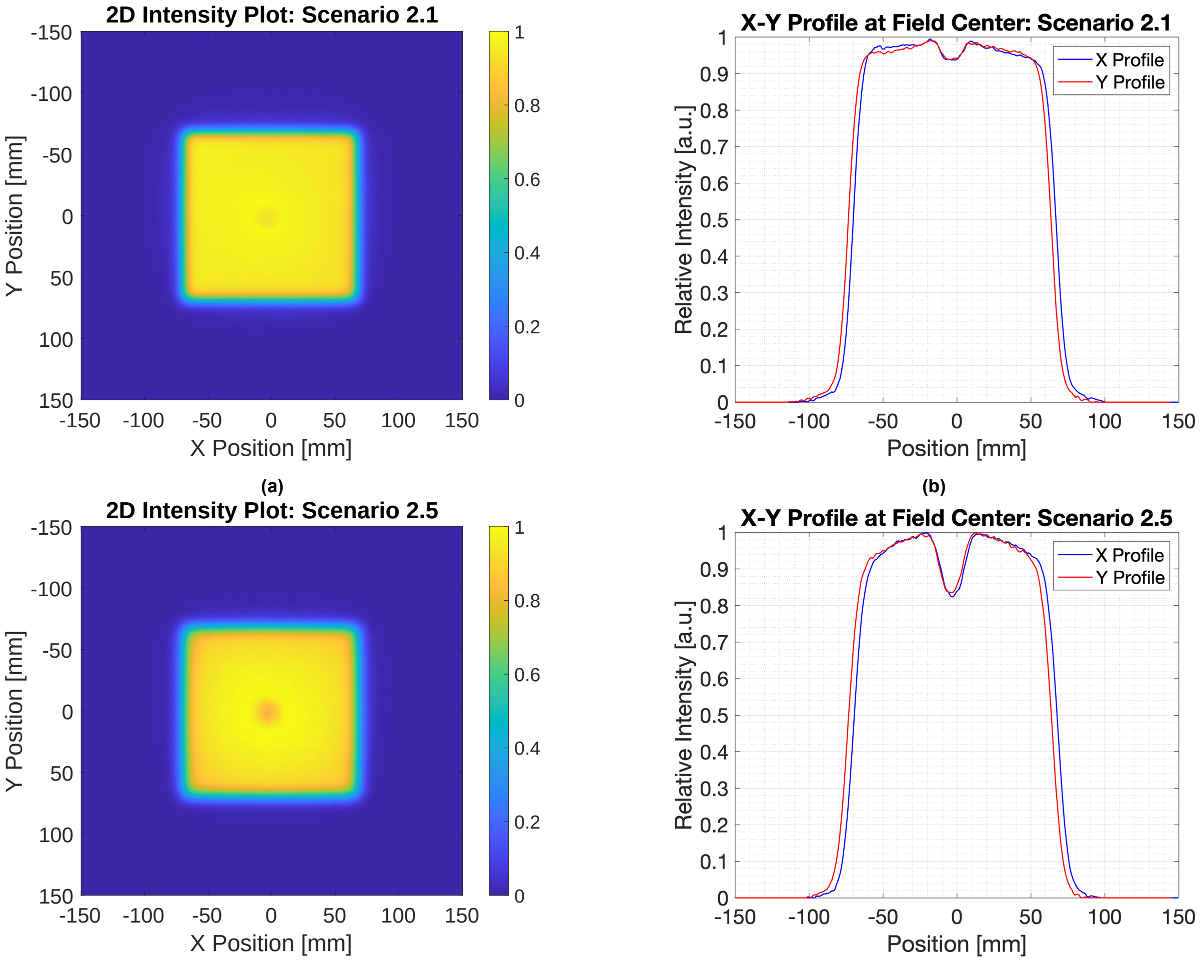

(a) (b) (c) (d)

Figure 4.10: Figure 4.10a and 4.10b correspond to clinical scenario experiment 2.1 and 4.10c and 4.10d to experiment 2.5. A difference in the amount of signal reduction between the two experiments is observed.

4.4. Additional configurations

4.4.1. Orientation of clip

In a clinical context, the clip is often not situated perpendicular to the treatment beam and not irradiated precisely at its center point. It is more common for the clip to be positioned off-center with respect to the proton beam or to be tilted. Therefore, two additional configurations were tested. In the first configuration, the clip was displaced 4 cm along the x-direction. The second configuration involves rotating the clip 90 degrees relative to the beam.

Clip positioned 4 cm off-beam

For this experiment, Base Experiment 1 was repeated. The clip was kept attached to the bone-equivalent plate and was shifted such that the center of the clip was positioned 4 cm away from the center of the beam. The uniformity was calculated as 98.2% along the y-direction in a range of 50 mm around the clip and 97.8% along the x-direction in a range of 20 mm around the clip (since the clip was positioned at the side of the irradiation field, the uniformity could only be calculated up to 20 cm around the clip). This indicates that moving the clip off-center has no effect on the field modulation caused by the clip. This implies that in the subsequent experiments presented in Chapter 5, the positioning of the clip at the center to the field center is not a restriction. The 2D intensity plot and corresponding line profile are provided in Appendix B.

Clip rotation

In this experiment, the clip was rotated 90 degrees with respect to the beamline. To rotate the clip, it was detached from the bone-equivalent plate and positioned at the field center of the beamline. The uniformity calculated along the x-direction is lowered to 96.0 %, which can be explained because the presence of the rotated clip causes two areas of signal reduction in the radiation field (one for the bottom and one for the top disk), see Figure 4.11.

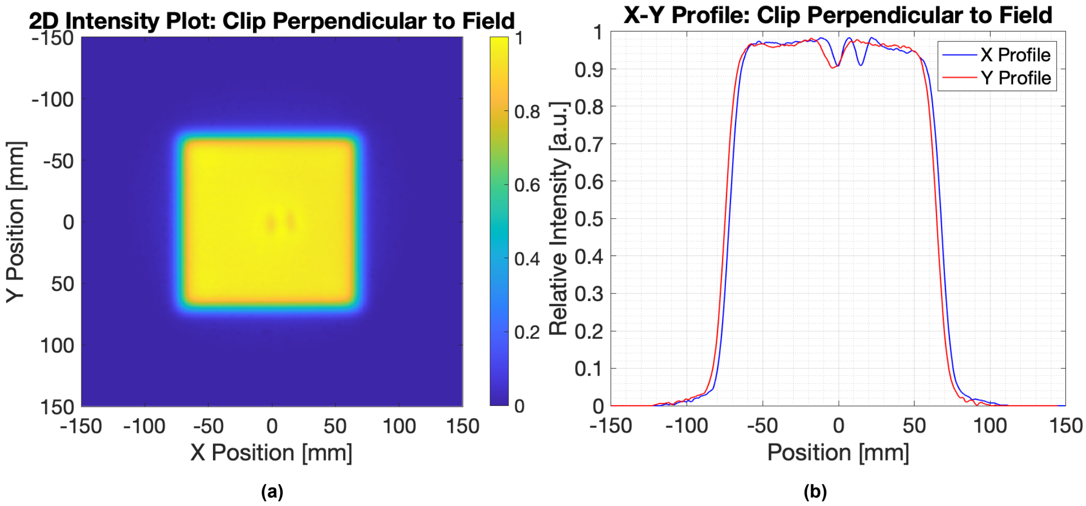

(a) (b)

Figure 4.11: The clip is positioned perpendicular to the field (90 degrees rotation with respect to the beamline) and it was detached from the bone-equivalent plate. In the setup there was 55 mm RW3 placed in front of the clip and no RW3 after the clip.

4.4.2. Separate components

To examine the contribution of the pin on the dose modulation and to investigate whether the characteristic shape of the bottom and top disk of the clip has an influence on the dose perturbation, a last experiment was performed. Here the different components of the clip were tested separately. First, the top disk was irradiated, followed by the irradiation of the bottom disk along with the pin, see figure 4.12. In both experiments, 55 mm of RW3 plates were placed proximal to the clip, which was attached to the bone-equivalent plate, and no RW3 was placed distally from the clip.

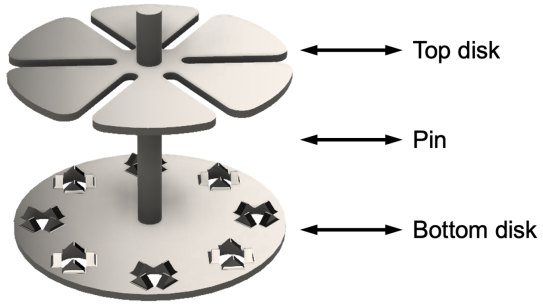

Figure 4.12: The 3 components of the clip: the bottom disk (this is placed underneath the skull), the tube (this is placed vertically between the skull segments), and the top disk (this is placed on top of the skull).

The results are depicted in Figure 4.13. In Figure 4.13b, a signal reduction similar to the previous experiments was measured. However, at the center of the signal reduction, a small elevation is visible, which can be caused by the hole in the top disk. In Figure 4.13d, the bottom disk in combination with the pin is measured. The results imply that the pin does not cause an additional field modulation. The uniformity for both experiments is calculated and presented in Table 4.3. The results show comparable results for both configurations. It was not possible to measure an effect caused by the holes in the bottom disk or the incisions in the top disk of the pin in the radiation field.

Table 4.3: Uniformity along x- and y-direction for experiments where the components of the clip were irradiated separately.

	Top disk	Bottom disk and pin
Uniformity x direction [%]	97.5	97.4
Uniformity y direction [%]	98.5	98.0

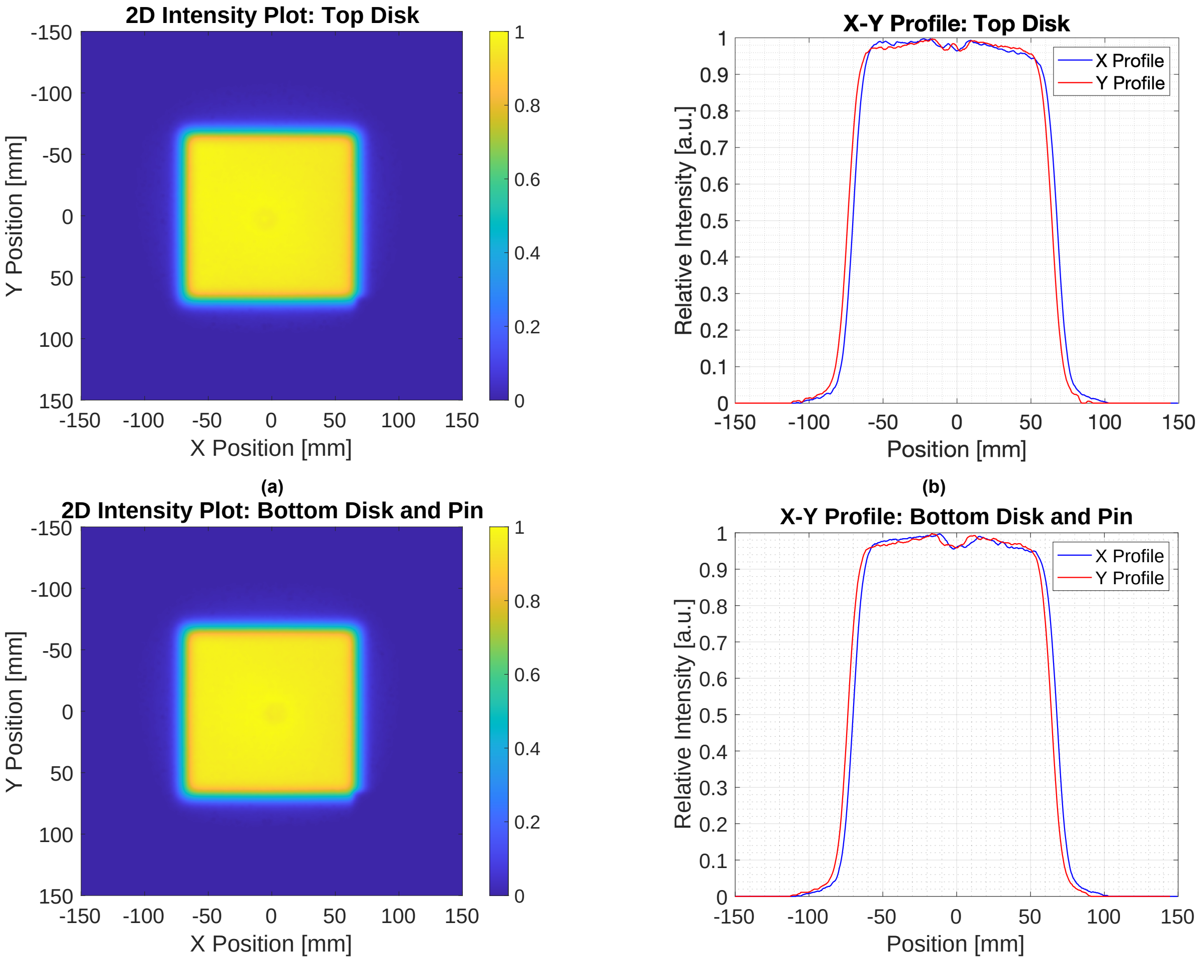

(a)

(b)

(c)

(d)

Figure 4.13: In figure 4.13a and 4.13b, the results of the experiments where the top disk was irradiated are displayed. In figure 4.13c and 4.13d, the results of the experiments involving the bottom disk in combination with the pin are presented.

4.5. OCTAVIUS detector

After the experiments with the Lynx detector were finished, the OCTAVIUS detector was utilized. First, base experiment 1 was repeated, which included placing 55 mm RW3 in front of the clip. The aim was to investigate if it was able to detect the dose modulation caused by the clip with the OCTAVIUS detector, which has a 5 mm resolution. Hereafter, scenario 2.5 was repeated, including 55 mm RW3 in front of the clip and 20 mm RW3 after the clip. Given that this scenario exhibited the most substantial reduction in uniformity in the previous experiments, the objective was to determine whether this effect was also measurable when utilizing the OCTAVIUS detector.

The results are depicted in Figure 4.14, in which the line profiles are normalized with respect to their maximum value. The detector's reduced resolution has reduced the measurement quality, the measurements could only be taken at a few points along the clip. In Figure 4.14c the signal reduction caused by the clip is less pronounced than in the experiments using the Lynx detector. Additionally, in Figure 4.14d, the dose reduction caused by the clip is enlarged, just like in the experiments conducted by the usage of a Lynx detector.

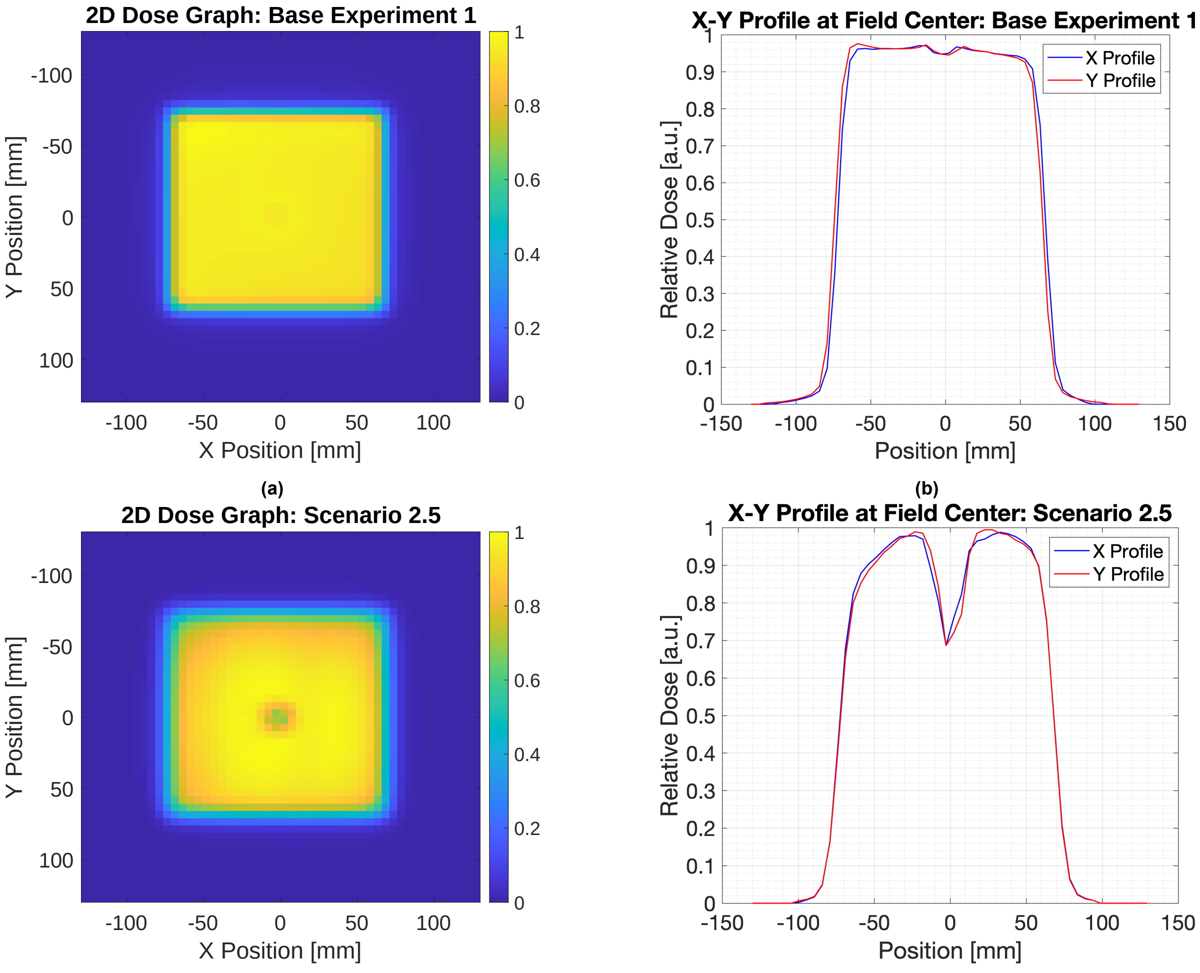

(a)

(b)

(c)

(d)

Figure 4.14: Base experiment 1 is presented in figures 4.14a and 4.14b and scenario 2.5 in figures 4.14c and 4.14d. An increased dose reduction is observed in the graphs corresponding to experiment 2.5. The line profiles are normalized with respect to their maximum value

4.6. Gafchromic films

In addition to conducting experiments by using the Lynx and OCTAVIUS detector, the usage of Gafchromic films was investigated. For these experiments, a film was attached to one of the detectors used in the previous experiments, to fixate it at the center of the radiation field. In this experiment, 55 mm of RW3 was placed in front of the clip and 20 mm RW3 after the clip. The main goal was to investigate if the usage of the films was of added value to the other detectors. The results are depicted in Figure 4.15. In Figure 4.15a, a picture of the irradiated film is displayed. The film was scanned after 120 hours. The film shows a clear colorization, presented as a darkened square in the figure. The film was analyzed in the software program ImageJ. Here, the calibration data was used to convert the data to dose in Gray. Additionally, the data was inverted before the plots were created. A vertical line profile was drawn through the center of the irradiation field and normalized to its maximum value, depicted in Figure 4.15b. The line profile demonstrates a dose reduction, caused by the clip, visible in the center of the radiation field.

There is no measurable effect found of the pin in between the disks of the clip, or the holes in the bottom disk and inceptions on the upper disk of the clip, regardless of the submillimeter resolution of the films.

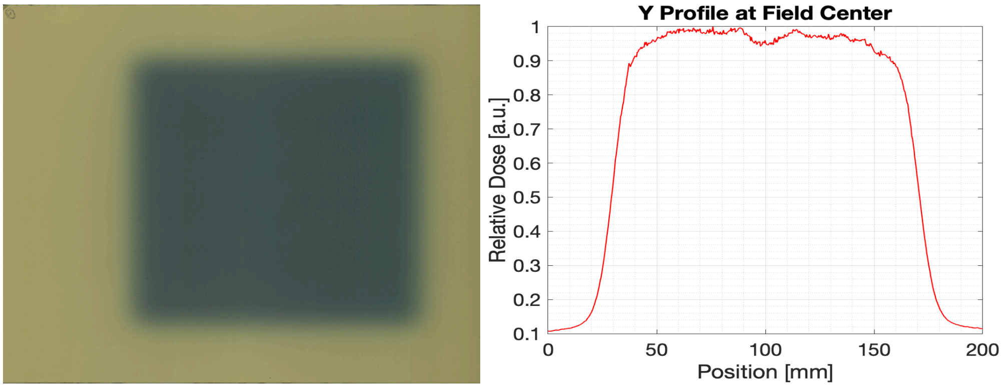

(a)

(b)

Figure 4.15: In Figure 4.15a, an image of the scanned film is displayed. In Figure 4.15b, a vertical line profile through the center of the radiation field is depicted. Note that the line profile is normalized with respect to its maximum value.

4.7. Conclusion on experiments

The presence of a titanium clip in a radiation field created by a 150 MeV mono-energetic proton beam produces a measurable signal perturbation. The effect varies among different scenarios when the clip and detector are positioned at different locations along the SOBP. Additionally, the measured size of the signal perturbation corresponds to the dimensions of the clip. From these experiments, the contribution of the pin, that connects the lower and upper disks of the clip, on the dose perturbation is minimal. Therefore, no additional measures concerning field modulation induced by the pin will be implemented during the determination of the treatment planning strategies. The sharp edges of the clip created a local signal elevation, probably caused by multiple Coulomb scattering. Surrounding the edges of the clip, there were no additional scattering effects observed.

The conducted experiments serve as a basis for the subsequent experiments conducted in Chapter 5. Based on the presented findings, it was chosen to use the Lynx detector in the following experiments. The resolution of the Lynx detector was adequate to capture the perturbation induced by the clip. It also provides a correct representation of the dimensions of the clip. Additionally, the Lynx detector is easy to use and provides on-site direct information of the data. Gafchromic films presented similar results as the Lynx detector. However, the films require an increased workload and induce several uncertainties, as presented in Section 4.1.3. Moreover, the Gafchromic films are expensive to use. Since it provided no additional crucial information on the dose perturbation, it was chosen not to use them. The OCTAVIUS detector's resolution is significantly worse than the other two detection methods. The reduced resolution becomes problematic when imaging small features, as is the case in this thesis. The lateral penumbra measured with the OCTAVIUS were significantly less sharp than the measurements involving the Lynx detector and films. Therefore, the subsequent experiments will not involve the use of this detector.

5

Treatment planning strategies

This chapter covers the second set of experiments that were conducted in this thesis. These experiments will be performed in one of the clinical treatment rooms of HollandPTC and involve the use of the treatment gantry. The objective of these experiments was to determine an adequate treatment planning strategy to handle the presence of the metal clip in the irradiation field. First, an overview of the treatment planning strategies, their integration into the treatment planning system Raystation (RaySearch Laboratories, Raystation 10B), and the methodology of conducting the experiments is provided. Subsequently, in Chapter 6 ‘Results’, the outcomes of the experiments are presented.

5.1. Treatment planning strategies

Based on the literature review, presented in Appendix A, and the first set of experiments, a total of seven strategies were created, each encompassing a way to handle the presence of metal implants in the treatment field. The strategies are based on three main concepts: applying a density override on the clip, using either a single-field optimization (SFO) or multi-field optimization (MFO) technique, and the difference between including beam-specific margins or not. Additionally, in strategy 7, an avoidance margin was set around the clip. Note that the beam-specific margins were only added to SFO techniques and not to MFO techniques. This is attributed to the fact that in SFO, the optimization of one field does not depend on the optimization of the other field(s), which is why beam-specific margins are allowed. In MFO techniques all beams in the treatment plan are optimized simultaneously. More information on the basic principles of these methods is provided in Chapter 2. An overview of the seven strategies is depicted in Figure 5.1. The strategy that is currently employed at HPTC is strategy 4.

In the following subsections, the implementation of these strategies in the treatment planning system will be explained. Here, the basic aspects of treatment planning in Raystation will be encompassed, emphasizing the employed strategies. After this, the experimental setup for the experiments and the analysis methods will be presented.

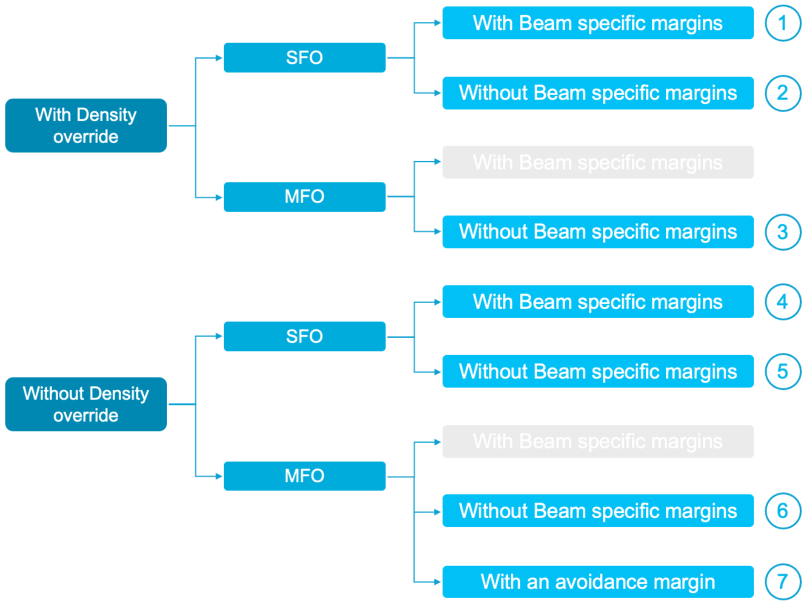

Figure 5.1: An overview of the treatment planning strategies that each encompass a way to handle the titanium clip.

5.2. Treatment planning in Raystation

At HollandPTC, the treatment planning system Raystation (RaySearch Laboratories, Raystation 10B) is utilized to develop proton therapy treatment plans. The interface comprises seven categories of tabs; see Figure 5.2. This guides the user through developing a treatment plan. The categories that are used for creating the treatment plans for this thesis are enlightened in the following subsections.

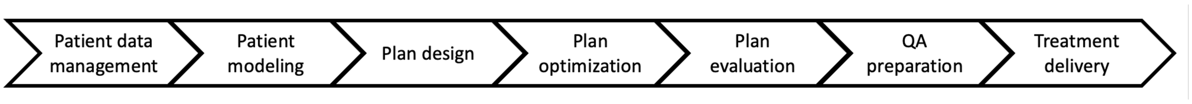

Figure 5.2: The different division tabs in Raystation. Each tab is implemented to cover a part of the treatment planning process.

5.2.1. Patient data management

The first category is the patient data management tab. Here, information on the patient, or in this case, the phantom, is provided, and it allows you to select the correct image set. The choice of CT scan was made based on recommendations of the literature review and according to the findings presented in Chapter 3.

5.2.2. Patient modeling

When commencing the treatment planning procedure, an important step is to define the regions of interest (ROIs). This is done under the subtab ‘structure definition’. In this experiment, this entails delineating the clip, bone-equivalent plate, and RW3 plates. Additionally, to facilitate creating a treatment plan, a CTV and one OAR were delineated. The delineation was done using the ‘smart brush’ tool in Raystation or by using a predetermined shaping template.

One crucial aspect to consider when delineating ROIs is adjusting the level/window settings of the CT image. The window represents the range of HUs present within the displayed CT scan. The level represents the center of the window. By adjusting these values, the user can modify the contrast of the CT scan [70]. There are predefined settings that can be implemented for the visualization of different types of tissues. The Raystation settings that are important to use in this thesis are the bone preset (L 450 / W 1600), used for the visualization of the bone-equivalent plate, and the soft tissue (L 40 / W

350), used for the visualization of the RW3 plates.

In addition to the predefined settings, one can also manually adjust the level/window values. This is done by inspecting the gray value histogram, which is CT-scan specific; see Figure 5.3. In this histogram, the x-axis presents the gray values in the image and ranges from -1024 to 260 HU. The y-axis presents the number of pixels that correspond to a specific gray value. A homogeneous object is represented by a peak. This is because a homogeneous object consists of a narrow range of HU values. Non-homogeneous objects are more difficult to distinguish in the histogram due to a wider variety of HU's in such an object. When the HU range of a structure in the image is known, this knowledge can be used to adjust the level/window settings to enhance visualization.

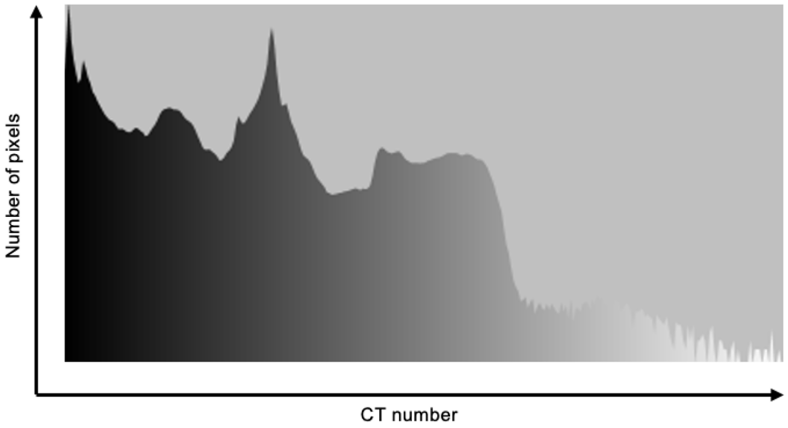

Figure 5.3: The gray value histogram of the CT scan of the phantom. On the x-axis, the CT number, also the HU's, is depicted. On the y-axis, the number of pixels.

When defining the ROIs, several properties can be adjusted. This includes setting the organ type, e.g., CTV or OAR, and a possible density override. With a density override, the mass density of an ROI can be overwritten with a mass density preset of a type of organ structure or material. This technique will be used in some of the treatment strategies.

The following ROIs were created and a 2D overview of the delineated ROIs is depicted in Figure 5.4:

- **Clip**: The delineation of the clip is difficult due to several factors. First, the HU values of titanium can exceed the measurable limit of the CT scanner (which is 3070 HU for the imaging system used). Secondly, since the clip is relatively small and has fine structures present on its surface, partial volume effects can occur. Lastly, the presence of artifacts makes proper delineation a difficult task. This is why special attention was taken to ensure the clip was drawn correctly.

  Several different level/window settings were investigated for the delineation of the clip, and also the knowledge of the size of the clip was used. An extended overview of the procedure to delineate the clip is provided in appendix E.

  The application of a density override is based on the type of strategy; see Figure 5.1. If a density override on the clip was applied, this was done using the predefined Raystation material settings for titanium, with a mass density of 4.540 [g/cm^3].

- **Bone-equivalent plate**: The bone-equivalent plate was delineated with a level/window preset of bone (L 450 / W 1600). No material override was applied on the plate.

- **RW3 plates**: The RW3 plates were delineated with a level/window preset soft tissue (L 40 / W 350). The delineation was performed by setting a rectangular box around the RW3 plates. To correct the scattering artifacts caused by the clip and the air gaps between the plates, a density override was applied to the box, with a mass density of 1.045 [g/cm^3].

- **CTV**: The CTV was contoured as a 5 cm diameter sphere and placed at approximately 3/4 mm distal to the clip. The size of the CTV was based on the geometry of the phantom. It was verified if the dimensions were clinically representative based on research conducted at HollandPTC by Rojo-Santiago et al. [71]. In this article, research was conducted on patients who received treatment for brain tumors at HollandPTC in 2018 and 2019. The largest number of patients (15) in their cohort had a median tumor volume of 96.0 cm^3 (between a range of 39.7-340.1 cm^3). The delineated sphere in this project has a volume of 65.45 cm^3.

  For some strategies, the CTV will be expanded to create a beam-specific margin. This will be explained in the following paragraph.

- **OAR**: An OAR was delineated to compare the strategies based on OAR sparing. The OAR has a 4.1 g/cm^3 volume and is irregularly shaped. The aim was to place the OAR near the CTV and within the beamline.

- **External**: An external ROI must be delineated as a volume surrounding all other ROIs. Only the volume inside this external ROI will be included in the dose calculation. The remaining volume outside this ROI, will be interpreted as a vacuum.

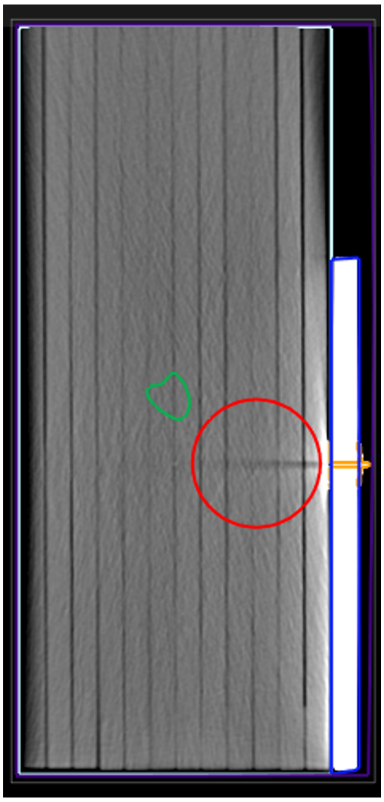

Figure 5.4: A 2D representation of a transversal slice of the delineated ROIs is presented: the clip (orange), the CTV (red), the OAR (green), the bone-equivalent plate (dark blue), the RW3 plates (light blue), and the external (purple).

Beam-specific margins

The clips create a range uncertainty in the beam path. In some strategies, a beam-specific CTV is involved with the aim of including the range uncertainty only locally around the clip and not in the entire plan. This is done by adding distal, proximal, and lateral margins around the clip. After the clip is delineated, the beam-specific CTV is created using a script developed at HollandPTC. The following steps are included in the process:

1. Shadow: An ROI is created with a distal extent that goes far beyond the CTV (at least 10 cm), and a lateral extent of 0.2 cm is applied. This creates a shadow behind the clip in the path of the beam. See Figure 5.5a.

2. Beam-specific margin: An ROI is created with a distal and proximal extension of 0.5 cm per 1 cm path length. The lateral extension is set to 0 cm (because this is already incorporated in the previous step). See Figure 5.5b.
3. Beam-specific CTV: Creating the final beam-specific CTV includes two steps. First, the union of the original delineation of the CTV and the shadow of the clip is calculated. This is a temporary CTV, which indicates where the CTV must be expanded. Secondly, the intersection of the temporary CTV from the previous step and the CTV containing the beam-specific margin is computed. This results in a CTV with an expanded margin that is beam-specific; see Figure 5.5c

An aspect that needs to be considered is the path length of the beam through the clip, which is an input parameter for the script. After the beams are set up, which is explained in Section 5.2.3 'Plan design', the path length of the beam through the clip can be measured with a measuring tool included in Raystation. Here, the path length through the pin is not included since no effects of the pin are found in the first series of experiments. Another precaution that must be considered is that the new beam-specific CTV may not intersect with an OAR. This is not the case, as is depicted in Figure 5.6.

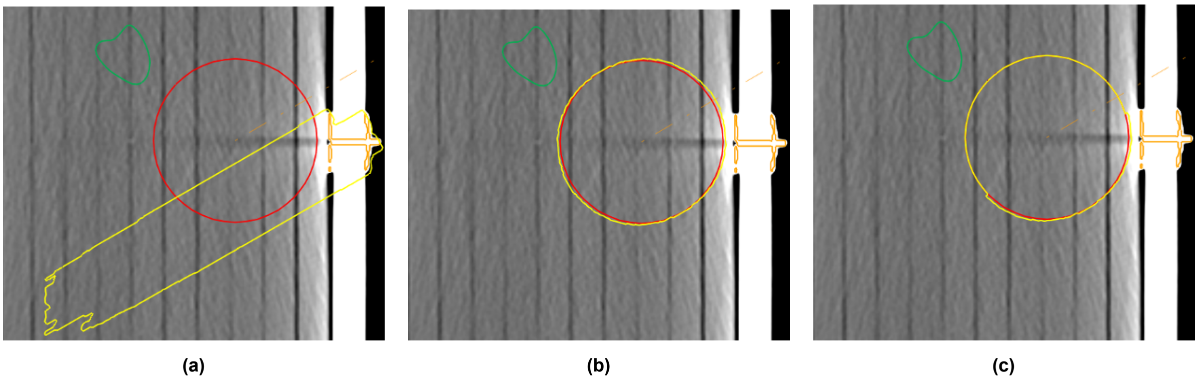
(a) (b) (c)

Figure 5.5: In figure 5.5a a shadow region (yellow) for one beam is depicted. In Figure 5.5b the CTV is expanded with a beam-specific margin (yellow). In Figure 5.5c the beam-specific CTV is visible (yellow).

Implementing this for both beams results in the configuration as depicted in Figure 5.6. Note that this method is only applied to the strategies that implement beam-specific margins. For all the other strategies, the plan is calculated based on the initial CTV.

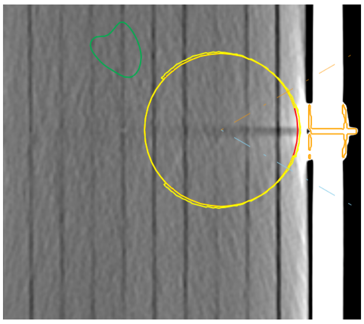

Figure 5.6: The two superimposed beam-specific CTVs, for the 2 incorporated beams.

5.2.3. Plan design

After all the ROIs are created, the next step in the process can be commenced: designing a treatment plan. In that step, the primary setup of the treatment plan is defined, encompassing elements like the choice of treatment modality, treatment technique, patient treatment position, number of fractions, beam specifications, and isocenter localization.

For all treatment plans in the experiments, the following settings are applied:

- Modality: Protons
- Treatment technique: Pencil beam scanning
- Patient treatment position: Head first supine (HFS)
- Fractions: 28 fractions of 1.8 Gy (total dose = 50.4 Gy)
  The dose prescription is based on the dose prescription for low-grade gliomas [72], which is also adapted at HPTC.

Beam settings

After a plan is created, the beam settings need to be specified. First, the number of beams and their angles are defined. In all treatment plans, two beams are utilized to deliver the dose, to mimic a realistic treatment plan. The beams are aimed at the center of the CTV ROI and are positioned under a 60- and 120-degree angle, which is achieved by rotating the gantry.

After this, there are several parameters that can be adjusted for each beam. This includes the possible usage of a range shifter (RS) and adjusting the size of the air gap. A typical proton therapy pencil beam scanning setup, involving an RS, airgap, and transferable snout, is depicted in Figure 5.7.

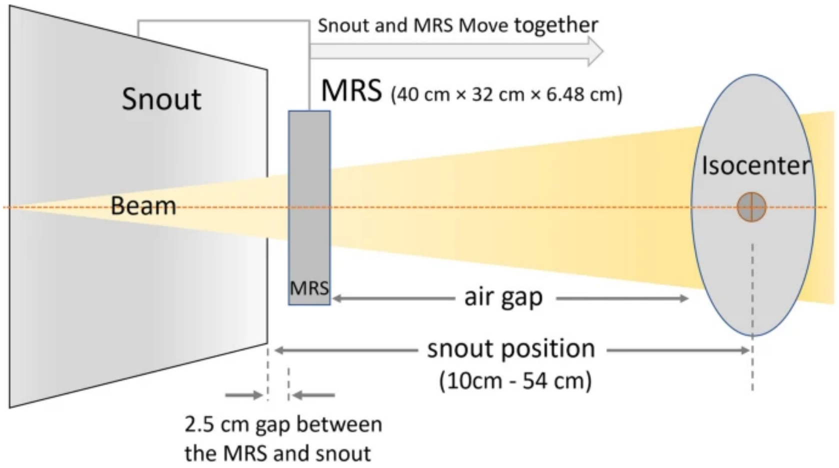

Figure 5.7: A visual representation of a PBS setup. On the left, the snout is visible with a machine-related range shifter (MRS) next to it. The snout and MRS can move together towards the isocenter of the target. The air gap is defined as the space between the MRS and the isocenter [73].

The Probeam treatment delivery system can deliver proton therapy with an energy range of 70 MeV to 250 MeV. In pencil beam scanning, the spots that fill the more superficial areas are filled with low-energy protons, and vice versa, the deeper spots are filled with high-energy protons. When tumors are situated near the surface, it may be necessary to use low energy values to provide effective irradiation, which can potentially fall below the system's minimal limit. To overcome this limitation, a range shifter (RS) can be placed between the treatment head and the patient [74]. This is a piece of material, that functions as an energy absorber and thus shifts the range of the proton beam [75]. For the experiments conducted in this thesis, there is a need to use an RS when, after a treatment plan has been optimized, the lower energy layers contain spots of 70 MeV.

The RS's that can be added in Raystation are 2, 3, or 5 cm, but only the latter two can be clinically implemented. First, it was investigated if the usage of an RS was necessary. When no RS was added, the lowest energy layers did include several spots of 70 MeV. Therefore, an RS of 3 and 5 cm were applied and their results were evaluated. A 3 cm RS resulted in sufficiently high energy layers. Therefore, a 3 cm RS is applied to both beams for all experiments. The usage of an RS is however accompanied by a disadvantage. The protons that traverse the RS will scatter, which as a result will enlarge the lateral penumbra of the beam [75]. This effect should be considered when an RS is used.

In addition to the usage of an RS, the air gap can be adjusted when designing the treatment plan. The air gap defines the space between the treatment head and the phantom. When an RS is added, this distance is measured from the end of the RS to the patient. Evidence shows that a larger air gap enlarges the spot size, potentially undermining dose precision [76]. Thus, in pencil beam scanning proton therapy, it is desired to place the treatment head as close to the patient as possible, to mitigate the mentioned disadvantages. This can be obtained by moving the snout towards the patient.

Dose calculation

To perform dose calculation, the HU values extracted from the CT scan need to be mapped to relevant material properties. This is done per voxel by determining three aspects: the mass density, the mass fraction of the atomic elements, and the mean ionization energy.

The mass density in g/cm^3 is determined by using an HU to mass density table or graph, depicted in Figure 5.8. A mass density of 0.00118 g/cm^3 is applied for all HU values below -1000, and 3.0206 g/cm^3 for values above 3070 HU.

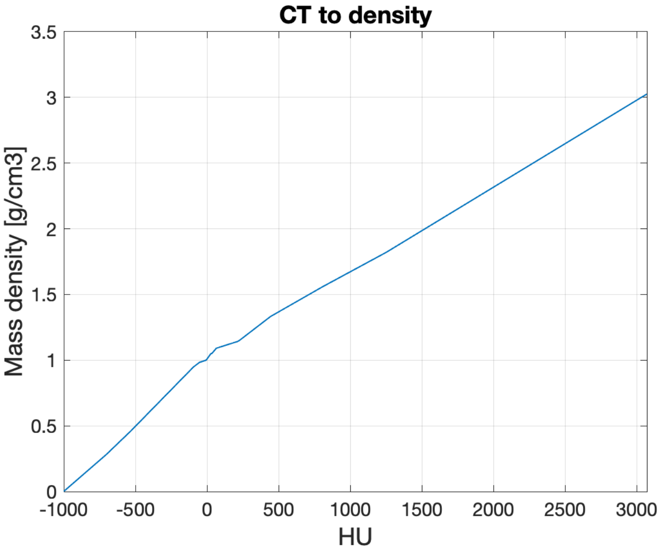

Figure 5.8: The CT to density definition that is applied by the treatment planning system Raystation.

Additionally, it is necessary to get insights into the mass fraction of the atomic elements and the mean ionization energy. If a material override is applied to a structure, this information is obtained from the characteristics of the overridden material. If no material override is applied, this information is extracted from the HU values. A material reference list is provided by the treatment planning system to extract the other relevant parameters. This is a list that consists of several predetermined materials, that encompass the materials that can be present within a patient. Per material, the mass density, the mass fraction of the atomic elements, and the mean ionization energy [eV] are provided.

There are two types of dose calculation algorithms that can be implemented in Raystation. Based on the findings of the literature review, a Monte Carlo dose calculation algorithm was employed in all treatment plans. When using an MC algorithm for dose calculation, a few parameters can be adjusted. First, the uncertainty of the dose calculation can be set. This represents the statistical uncertainty of the dose calculation per beam. It is set as a threshold, governing what remains within the bounds of clinical acceptability. Its calculation is based on the assessment of every voxel, wherein the radiation dose exceeds 50% of the dose maximum. A 1% uncertainty was set based on literature [77] and HollandPTC guidelines.

In addition to this, the amount of ions per spot during optimization can be adjusted in the treatment plan. Enlarging the number of ions per spot will result in a more precise dose calculation. However, it enlarges the system's computational demands and time [78]. The minimum amount of ions per spot was first set to 4000 based on HollandPTC guidelines. The accuracy of the system can be evaluated by comparing the amount of ions per spot before and after the final dose calculation. It is desired to have a minimal difference between these two values. After comparing several levels of ions per spot (4000, 6000, 8000, and 10000), 8000 ions per spot was considered to be a good compromise for the experiments conducted in this thesis.

Dose grid

Prior to commencing dose calculation, the dose grid needs to be set. This is the 3D volume on which the dose calculation will be performed. The parameter that is being adjusted here is the dose grid resolution. Changing this parameter has an influence on the dose output. The Monte Carlo dose algorithm calculates the average dose per voxel. This implies that a fluctuation in dosage at a smaller detail than the current dose grid resolution, will not be accounted for in the dose calculation. However, a disadvantage is that setting a higher-resolution dose grid requires more computational time. Based on HollandPTC guidelines for dose planning on neuro patients with clips, a dose grid of 0.1 cm was adopted.

5.2.4. Plan optimization

After all aspects of the plan design are set, the plan optimization can begin. Here, treatment objectives and constraints are defined, which will function as a basis for the optimization process. The aim is to create a plan in which a sufficiently high dosage is provided to the CTV, while optimally sparing the OAR. Targeting the CTV is considered to be the highest priority in this thesis. Therefore, the optimization function regarding the CTV is set up first. The optimization functions regarding the CTV and OAR are presented in this section. An overview of the additional applied optimization settings is provided in Appendix D.

Optimization functions: CTV

For the CTV, an optimization function in terms of the prescribed dose level is implemented. The total prescribed dose for the CTV is 50.4 Gy [72]. The dose objectives differ to create an SFO or MFO strategy. A broader explanation of the difference between SFO and MFO techniques is provided in Chapter 2. In the case of an SFO technique, the beams are optimized independently, and therefore, the dose objectives are restricted per beam. To achieve this, the minimum and maximum dose objectives are established for both beam 1 (B1) and beam 2 (B2). The specified objectives for each beam encompass half of the total prescribed dose, e.g. 0.5 x 50.4 = 25.2 [Gy]. In the case of the MFO technique, all beams are optimized simultaneously, therefore one objective is defined for the minimum and one for the maximum dose. An overview of the objectives per optimization technique is provided in Table 5.1.

Table 5.1: The dose objectives per beam, based on either an SFO or MFO technique.

	Objective	Beams	Dose [Gy]	ROI	Weight
SFO	Minimum dose	B1	25.2	CTV	100
	Maximum dose	B1	25.2	CTV	50
	Minimum dose	B2	25.2	CTV	100
	Maximum dose	B2	25.2	CTV	50
MFO	Minimum dose	B1 & B2	50.4	CTV	200
	Maximum dose	B1 & B2	50.4	CTV	100

In the case of a beam-specific CTV, the dose objective is set to this beam-specific CTV, and thus the ROI in Table 5.1 will be adjusted. Further explanation on the application of beam-specific margins is given in Section 5.2.2.

In addition to the dose objectives for the CTV, objectives are also applied to decrease the dose to the other structures. First, a dose fall-off function is incorporated into the optimization parameters. This function operates to minimize the dose around the target, not only in the OARs but also in other normal tissues. Simultaneously, it permits the establishment of a build-up region directly surrounding the target. In this region, the dose can increase up to the maximum dose required for the CTV. The result is a more conformal dose at the boundaries of the CTV.

The function is set up in the plan optimization tab in Raystation and is applied to the external ROI. The high dose level is set at the maximum dose of 50.4 Gy, and the low dose level at 0. Additionally the ‘low dose distance’ needs to be defined, which corresponds to the build-up region. In this region, the dose reduces linearly from the high dose level to the low dose level. The parameter’s value was adjusted by experimenting with various values between 1 and 3 cm. The most balanced setting was found to be 2.7 cm and was applied to all strategies.

Optimization functions: OAR

Lastly, an optimization function is introduced to decrease the dose to the OAR. The system will try to optimize the treatment plan so that every goal is met. However, this often can lead to trade-offs between the different goals. Because the CTV coverage is determined to be of more importance than the OAR sparing, the weight of the OAR objective is set to 20, in comparison to the larger weight applied to the CTV as is depicted in Table 5.1. The value of the OAR objective dose is determined in an iterative manner. In this way, potential tradeoffs are examined, and a well-optimized plan is selected.

To determine the OAR optimization function, the following steps are pursued:

1. The plan with only the optimization functions for the CTV and dose fall-off is optimized and a final dose is calculated. Hereafter, robust optimization is applied (more information on robust optimization is provided in the next paragraph).
2. It is checked whether the dose calculation leads to a sufficiently high coverage of the CTV. This is done in two ways:

    - Firstly, it is checked whether at least 98% of the target volume receives 95% of the maximum dose (47.88 Gy) (for more explanation about this clinical goal, see Section 5.2.5). This goal is required to be met for the voxelwise minimum scenario after robust optimization.
    - Secondly, the incorporation of an OAR dose optimization function can result in a significant underdosing in the region adjacent to the OAR. This aspect is established as a limiting factor in the process of optimizing the dose for the OAR. This phenomenon is illustrated in Figure 5.9. Although the voxel-wise minimum value remains above 98% (specifically, 98.28%), a notable underdosing issue emerges in the vicinity of the OAR, which may not be clinically desirable. To address this concern, it is recommended that the region receiving 95% of the maximum dose remains within a ±1 mm margin of the CTV border.

      This was integrated into this procedure in the following approach: the primary focus was on preventing any local underdosing within a ±1 mm radius in the region adjacent to the OAR. Additionally, as a secondary consideration with slightly less strict criteria, the presence of underdosages in alternative regions was evaluated.

    If both requirements are met, the next step is initiated.
3. In the dose statistics tab, the calculated dose levels for the current plan are displayed. Check what the near maximum dose to the OAR is. For this purpose, D1 is read out, which represents the dose at 1% of the OAR volume and is close to the maximum dose. 90% of the maximum dose is taken, which creates a new dose level that will be used as a maximum dose objective for the OAR.
4. Define a new or adjust an optimization function for the OAR. The function type is defined as a maximum dose. The dose level is defined in the previous step. The weight of the optimization function is set to 20.

5. These steps are repeated until the requirements in step 2 are no longer fulfilled. In that case, the optimization function from the last iterated step is adopted.

In Table 5.2, the implemented dose objectives for the OAR are displayed in the second column. The third, fourth, and fifth columns present the target coverage levels.

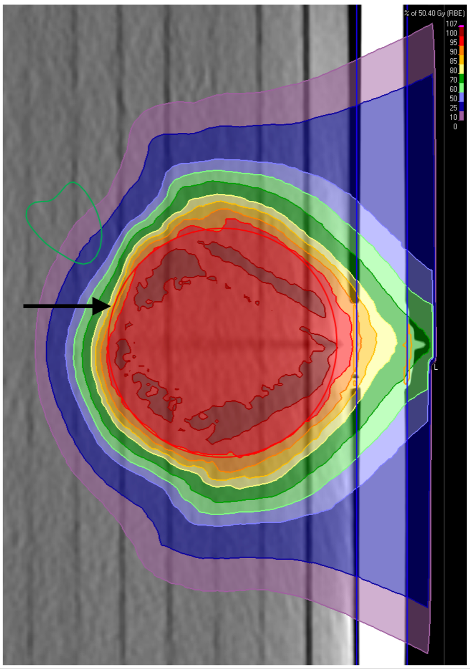

Figure 5.9: The black arrow depicts a dose reduction in the region adjacent to the OAR. The reduction is caused by setting a higher dose objective for the OAR.

Table 5.2: Overview of OAR dose objectives, applied as optimization functions for the plan optimization, and corresponding target coverage levels.

	Dose objective OAR: max dose [Gy]	Target coverage: Nominal plan [%]	Target coverage: Voxel-wise minimum [%]	Target coverage Voxel-wise maximum [%]
Strategy 1	33.29	100	98.57	100
Strategy 2	31.85	100	98.27	100
Strategy 3	27.43	100	98.32	100
Strategy 4	33.26	100	98.76	100
Strategy 5	31.97	100	98.40	100
Strategy 6	33.00	100	98.60	100

Robust optimization

Raystation has a built-in Robust Optimization tool. When determining the optimization functions, each function can be set to be robustly optimized or not. When robust optimization is applied, the determination of boundaries for setup and range uncertainties needs to be set. The optimization process is then carried out within these established boundaries, ensuring that the plan is robust to the set errors. The robustness settings in this thesis are based on the clinical protocol for neurological patients at HollandPTC [71].

The position uncertainty was set at 3 mm, for all dimensions (6 in total: left-right, inferior-superior, and anterior-posterior) and both beams. The setup uncertainty is selected as systematic, implying that the uncertainty is treated as a systematic error. The density uncertainty was set to 3%. This involves a stopping power range error. Combining the setup and range uncertainties, led to a total of 28 scenarios which are evaluated. These settings are applied in all treatment plans to all optimization functions for the CTV. More explanation on Robust Optimization techniques is provided in Chapter 2.

5.2.5. Plan evaluation

The last part of the treatment planning process is treatment plan evaluation. In this part of the process, it is determined if the treatment plan achieves all predetermined goals or if further optimization is required.

Clinical goals

The treatment plans are evaluated by predefined clinical goals, depicted in Table 5.3 These are based on clinical guidelines for neurological patients at HollandPTC. In the plan evaluation tab, every goal is presented, and the outcomes are illustrated as percentages.

Table 5.3: The clinical goals that were set for the target volume.

ROI	Clinical goal	Dose [Gy]
CTV	$D_{98}\% > 95\% * D_{\text{prescribed}}$	47.88
CTV	$D_{2}\% < 107\% * D_{\text{prescribed}}$	53.93
OAR	D_{1} As low as reasonably achievable	-

Robust evaluation

In addition to the nominal plan, the voxelwise minimum and voxelwise maximum plan can be evaluated if robust optimization is performed. The voxelwise minimum plan represents the minimum dose for every voxel, after evaluation of all scenarios, and the voxelwise maximum the maximum dose. These parameters serve as an effective tool for assessing the achievement of clinical goals. The achieved clinical goals in the voxelwise minimum scenario are established as a requirement for adequate CTV dose coverage. On the other hand, the voxelwise maximum can be employed to assess possible clinical goals concerning the OAR. The objective is then to maintain the voxelwise maximum scenario within the clinical limits. In Figure 5.10, an example of the cumulative dose volume histograms (DVHs) for the CTV (red) and OAR (green) are displayed. The nominal plan is depicted by a solid line, the voxelwise minimum by a dotted line, and the voxelwise maximum by a dashed line.

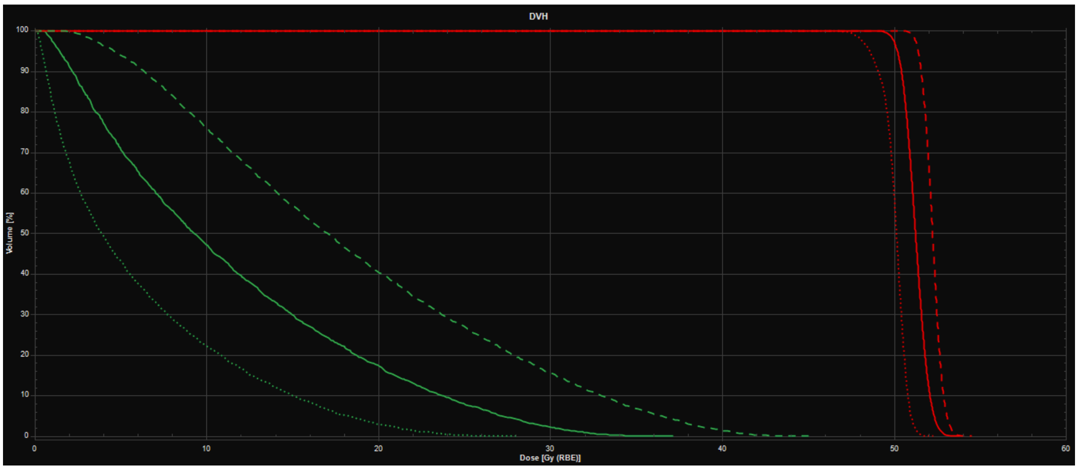

Figure 5.10: The solid line represents the nominal plan, the dotted line the voxelwise min and the dashed line the voxelwise max. In red, the curves for the CTV are presented and in green, the curves for the OAR.

5.3. Implementation of strategies

The methods described in this section are implemented in Raystation to create the different treatment planning strategies presented in Section 5.1. Strategies 1 to 6 were successfully implemented in Raystation: it was achieved to create treatment plans that met the clinical goals regarding CTV coverage and all plans showed good results on the robust evaluation.

However, strategy 7 was not included in the experiments. Strategy 7 was created based on the results of the literature review. It includes placing a 'block' around the implant. This block was created by adding an avoidance margin around the clip ROI. Fellin et al. [24] investigated the ability to avoid metal implants and their experiments included an MFO technique with the addition of an avoidance margin between 0.9–1.3 cm.

The treatment planning process for this strategy was carried out in the same manner as in strategy 6 (an MFO technique), with the addition of a 0.9 cm margin around the implant. However, this strategy showed suboptimal results for the 98% dose at 95% volume clinical goal: a voxel-wise minimum dose coverage of 95.76% was found, even when no dose objectives were applied regarding OAR sparing. The results of the dose distribution are depicted in Figure 5.11. It was concluded that this strategy is inadequate for the plan setup in this thesis and therefore, it was not included in the experiments.

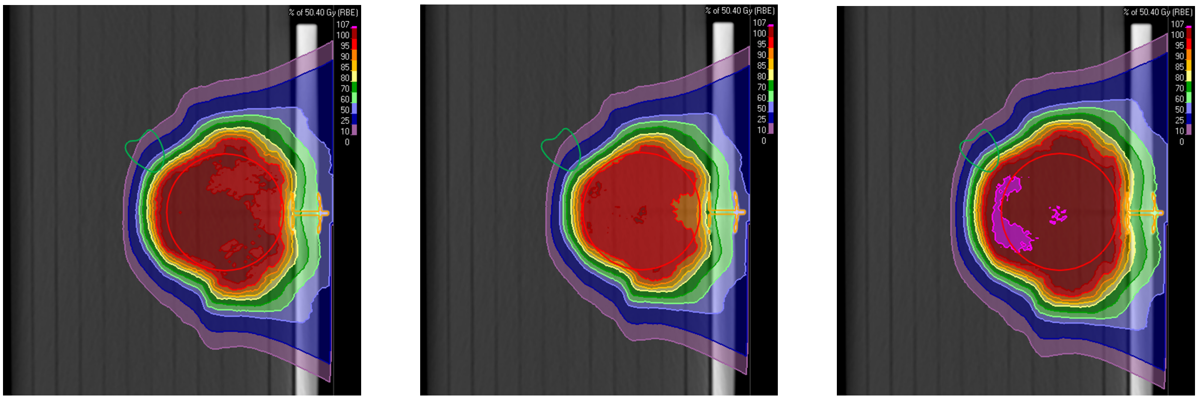

(a) (b) (c)

Figure 5.11: An MFO treatment plan with a 0.9 cm margin around the implant. 5.11a: the nominal plan, 5.11b: the voxel-wise minimum plan, and 5.11c: the voxelwise maximum plan.

5.4. Experimental setup

The experiments presented in this chapter are performed in one of the clinical treatment rooms at HollandPTC. The measurement setup is depicted in Figure 5.12. The six treatment plans based on the strategies outlined in Section 5.1, were implemented. Each strategy included two beam angles: 60 degrees and 120 degrees. The phantom is positioned at the center of the detector. The isocenter is aligned using the gantry's laser beams. Throughout all experiments, the distance between the detector and the phantom was kept constant.

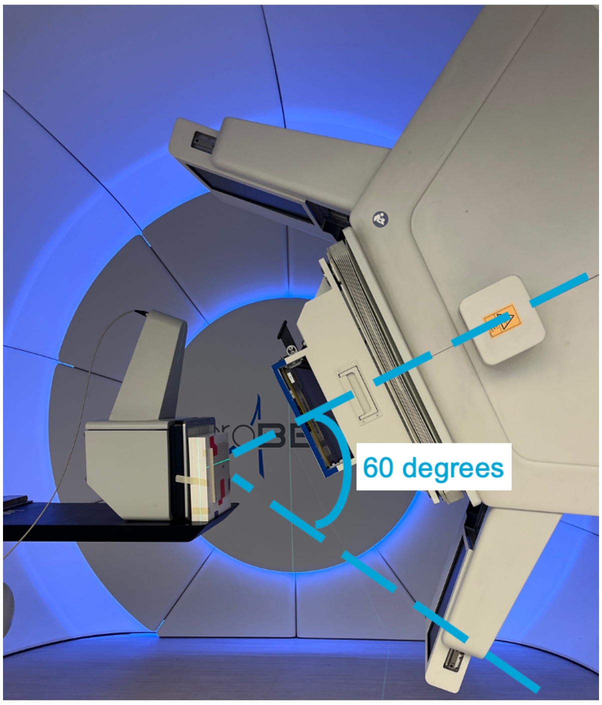

Figure 5.12: Experimental setup for the experiments performed in the clinical treatment room at Hollandptc. In blue, the used beam angles. The gantry is positioned at 60 degrees. The experiments are also performed when the gantry is positioned under 120 degrees.

The phantom is placed on the treatment table. Behind the phantom, the detector is placed at varying depths to measure the dose at different levels in the phantom. First, the detector was placed after one layer of RW3, to measure the dose at the beginning of the CTV. Secondly, the detector was placed after three slabs of RW3 to measure the dose at the center of the CTV. Thirdly, the detector was placed after five slabs of RW3 to measure the dose at the distal border of the CTV. And lastly, the detector was placed after six slabs of RW3, to measure the dose in the OAR. An overview of the detector depths is depicted in Figure 5.13.

The order of the experiments was as follows: the detector was positioned at one of the specified depths. Then, all treatment plans are applied for one angle. Hereafter, the gantry is rotated to the other angle, where all strategies are applied again. During this process, the experimental setup remains untouched to keep possible alignment errors constant at each depth. After all planning strategies are applied at both angles, the experimental setup is adjusted to the next specified depth.

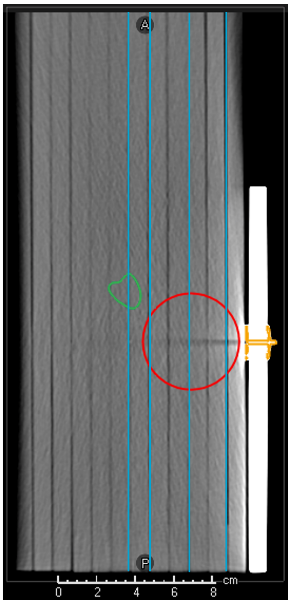

Figure 5.13: This Figure represents a cross-section of the phantom, in which the blue horizontal lines indicate the depths at which the detector was placed.

For all experiments, the iris aperture of the Lynx detector was consistently set to 50 and the exposure time was fixed at 2500 (more information on the Lynx detector settings is provided in Chapter 4. However, in the case of strategy 3 at 50 mm depth, the detector signal of the beam irradiating the phantom at an angle of 60 degrees became saturated. This saturation likely occurred due to the high number of motor units (MU) allocated to this particular angle within this strategy. The MU count for this specific combination of strategy, angle, and depth was the highest when compared to all other strategies and angles. As a response to this issue, the experiment was repeated with adjusted iris settings. It was found that when the iris setting was lowered to 49, the signal no longer became saturated. This adjustment in iris settings was solely made for this specific strategy, depth, and angle.

5.4.1. Checkup plan

In addition to the previously mentioned treatment plans, a checkup plan was created. This plan was made according to two objectives. First, it must determine the orientation of the measured data. Secondly, it gives an insight into the linearity of the used detector.

The plan is designed on a 30 x 30 cm RW3 phantom. In the phantom, 4 cuboids 3x3x5 cm are delineated. Each cuboid is optimized with different optimization goals: a uniform dose objective with 1, 0.75, 0.5, or 0.25 Gy. The measurements were performed by using the same Lynx detector as in all other experiments. Here, the iris was set to 0 to avoid saturation. An image of the checkup plan is provided in Figure 5.14.

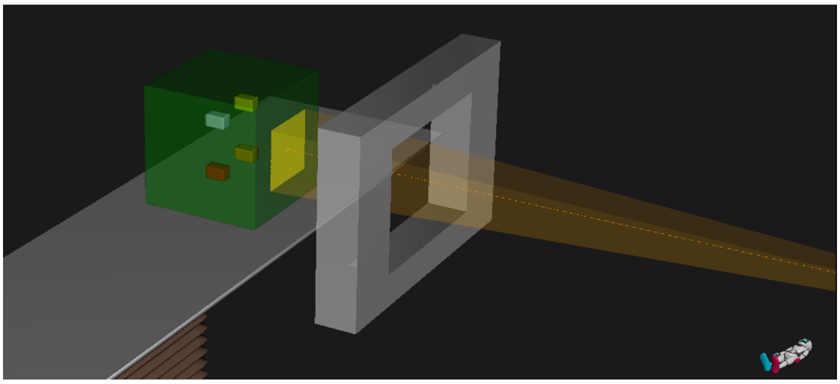

Figure 5.14: The experimental setup for the checkup plan. The green box represents the 30x30 RW3 phantom. In the phantom, four structures were delineated, receiving a dose of 1, 0.75, 0.5, or 0.25 Gy. The table was rotated 90 degrees compared to the depicted value, to be able to place the Lynx detector on the table.

6

Results

This Chapter provides an overview of the results of the conducted experiments. The goal of performing the experiments is twofold. First, the agreement between the treatment planning system and experiments is compared. Secondly, it is investigated what the best strategy is to handle metal implants in proton therapy. This assessment is based on CTV coverage and OAR sparing and will be determined based on the outcomes of the experiments.

6.1. Data processing

6.1.1. Experimental data

All experiments in this chapter are performed with the Lynx detector (IBA dosimetry). More information on the detector is provided in Chapter 4. At four depths along the phantom, the six treatment planning strategies were tested. Each treatment plan consists of two beams. Consequently, after the experiments, the data for each beam was combined independently for each strategy and depth. This resulted in a total of 24 2D dose planes, with dimensions 600x600 (x,y) (resolution = 0.5 mm). The orientation of the acquired data was compared with the checkup plan and adjusted to ensure that the correct orientation was employed; see Figure 6.1a. The output signal of the detector is presented as signal intensity values [a.u].

6.1.2. Raystation data

To perform the intended data analysis, it was necessary to extract the data from the treatment planning system. Raystation has a built-in tool to extract line profiles out of the system. However, extracting 2D dose planes is not supported. Therefore, an in-house developed Python script was used (the RayExpoort script developed by Matthijs Jansen). This extracts the dose per voxel from Raystation. The acquired data's alignment was compared with the checkup plan and adjusted to ensure the usage of the correct orientation, see Figure 6.1b. This resulted in a 174x298x144 (x-y-z) 3D volume for every strategy, containing all voxels inside the dose grid. Since the experimental data only contains 2D dose planes at four depths, the depths corresponding to the experimental depths were extracted from the 3D volume. This resulted in four 2D dose planes with dimensions 174x298 (x,y). The treatment plans in Raystation are calculated on a dose grid of 1 mm. Therefore, the resolution of the extracted Raystation data is 1 mm per voxel. The output data is presented in dose [Gy].

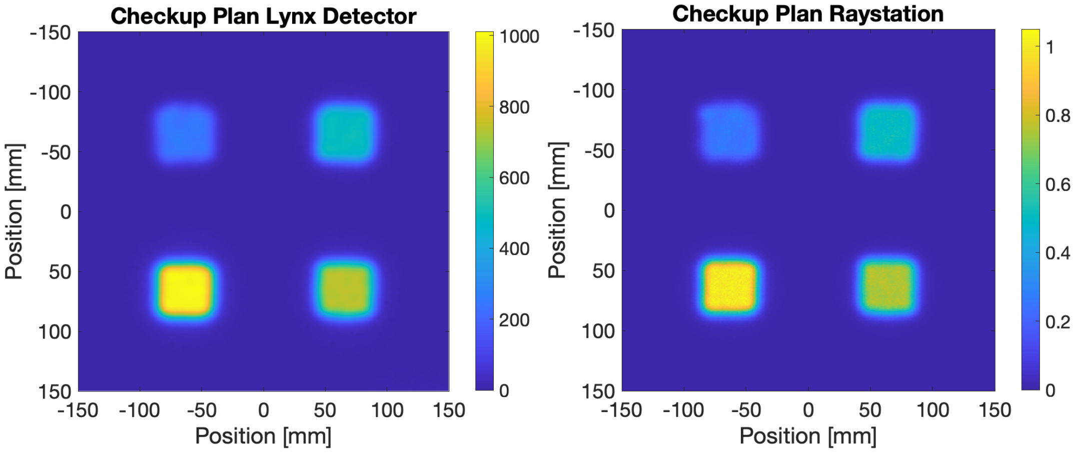

(a)

(b)

Figure 6.1: Orientation checkup plans of the experimental (figure 6.1a) and Raystation data (figure 6.1b)

6.1.3. Data comparison

Two important aspects need to be considered when comparing the experimental data with the Raystation data: the different resolutions and outcome metrics. An important note to make here is that the resolution of the Lynx detector is twice as high as the resolution of the Raystation data. However, this was inevitable, as the resolution is determined by the 0.1 cm dose grid that was applied, which is the minimum dose grid that Raystation supports. Additionally, the output of the detector is presented in signal intensity values [a.u.] and the output of the Raystation data in dose [Gy]. In this thesis, the detector data was not calibrated, so therefore, it was not possible to convert the intensity values to dose values. This must be carefully taken into account when interpreting the data.

In addition to these aspects, caution is required when interpreting the data for strategy 3, at a depth of 50 mm. As was mentioned in Section 5.4, for this setup, the beam angle at 60 mm was set to an iris of 49. The measurement at 120 degrees was measured with an iris setting of 50. This could have influenced the measured signal for this specific experiment.

6.1.4. Center of radiation field

The location of the center of the radiation field serves as an essential tool for data analysis. This is because this is used to determine the geometrical boundaries of the CTV when evaluating the CTV coverage. During treatment planning, the isocenter was set to be located in the center of the spherical CTV. This is considered to be the center of the radiation field. This point is projected onto every depth. From the Raystation data, the location of the field's center at the different depths can, therefore be precisely determined.

The experiments are performed according to the experimental setup as described in Section 5.4. During the preparation of the experimental setup, the isocenter was placed at the center of the phantom, which was subsequently placed at the center of the detector. The alignment was performed by using the in-room laser system. Nevertheless, alignment inaccuracies may have occurred during the setup of the measurement system. This also impacted the placement of the detector with respect to the phantom. To incorporate the last mentioned inaccuracy, the coordinates of the center of the field were also computationally determined for the experimental data. This was done by determining the centroid at each dose plane. Further explanation is presented in Appendix F.

6.2. Effect of clip on irradiation field

In this section, an overview of the initial findings is presented to indicate how Raystation incorporates the dose perturbation caused by the clip into the treatment plan and if this effect is measured in the experiments.

6.2.1. Projection of clip on 2D dose planes

The 2D planes corresponding to strategy 1 are depicted in Figure 6.3. It provides an overview of the experimental and Raystation data at all four depths. The projection of the clip on the dose field is visible in the 2D dose graphs as a dose reduction. The clip is projected twice, once for each beam, and shifts along with the beamline across the CTV. A graphical representation is provided in Figure 6.2.

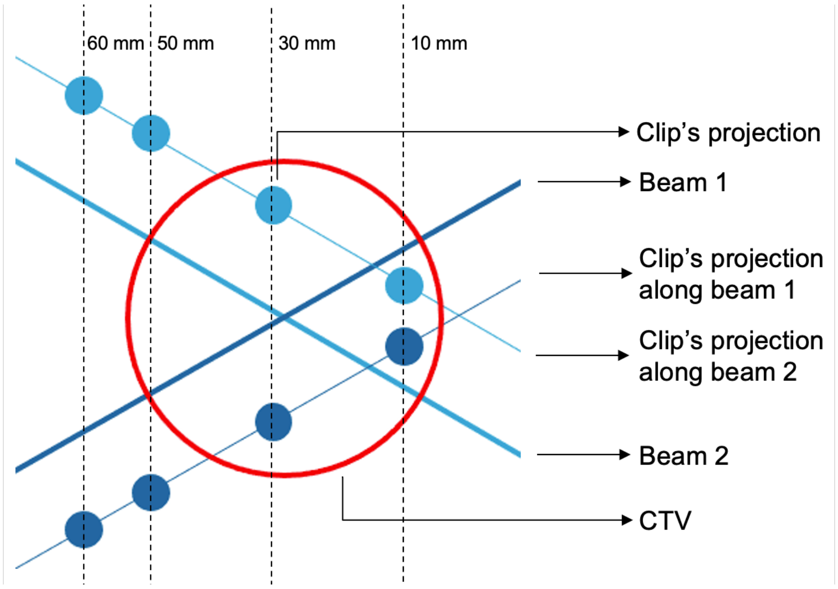

Figure 6.2: A graphical representation of the projection of the clip on the radiation field.

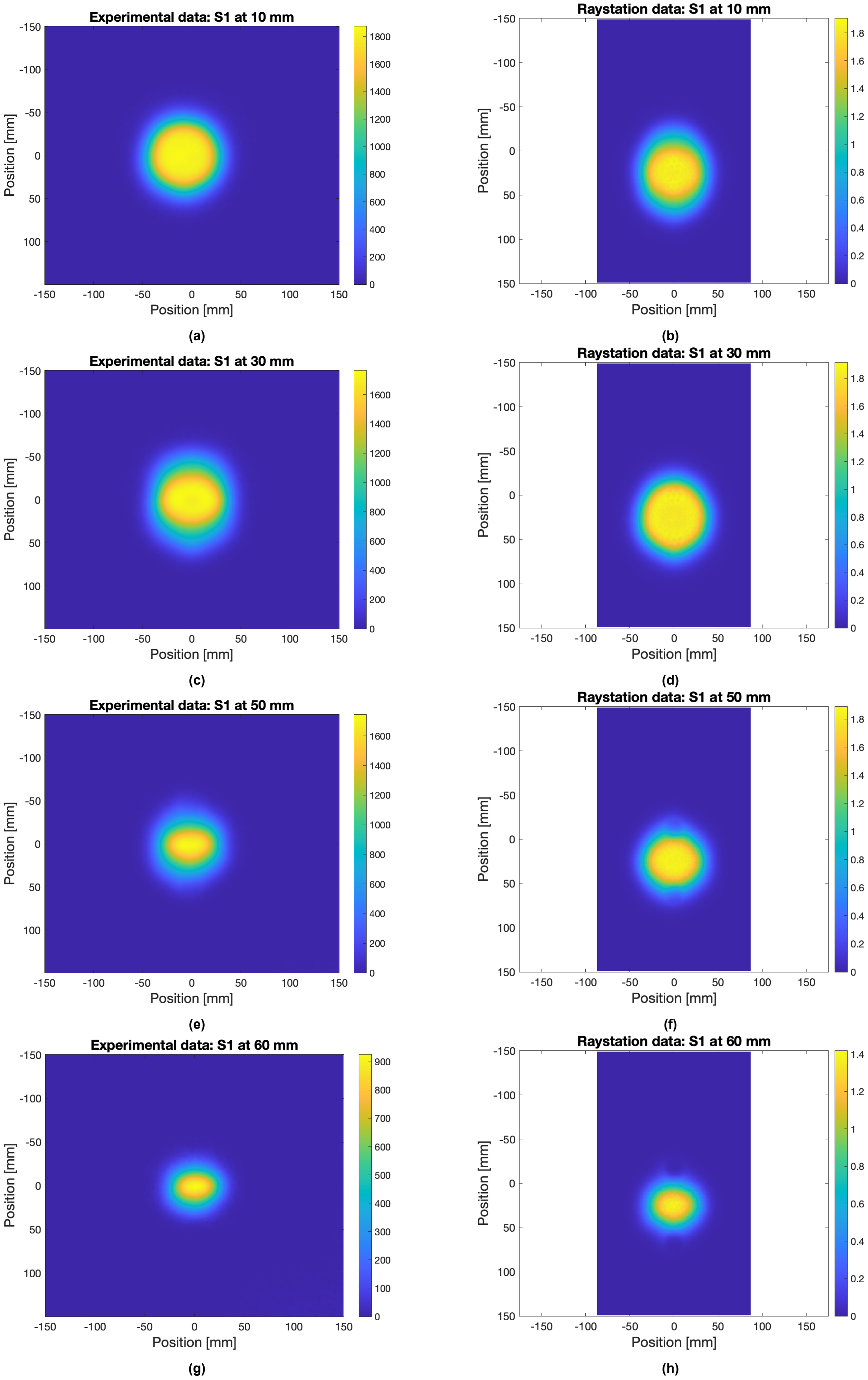
Experimental data: S1 at 10 mm

(a)

Raystation data: S1 at 10 mm

(b)

Experimental data: S1 at 30 mm

(c)

Raystation data: S1 at 30 mm

(d)

Experimental data: S1 at 50 mm

(e)

Raystation data: S1 at 50 mm

(f)

Experimental data: S1 at 60 mm

(g)

Raystation data: S1 at 60 mm

(h)

Figure 6.3: An overview of the 2D graphs, measured at the four depths along the phantom. In the left column, the graphs correspond to the experimental data, and in the right column, to the Raystation data.

6.2.2. Line profiles through centroid

To gain a better understanding of the perturbation caused by the clip, line profiles were extracted from the 2D graphs. The line profiles are drawn through the center of each 2D graph along the x- and y-axis. An overview of all line profiles is presented on page 48. Note that the line profile for strategy 3 at 50 mm depth should be interpreted with caution since the iris setting of one of the beam angles was adjusted for this specific measurement. In Appendix G, an overview of the normalized line profiles is provided.

Overall signal reduction

The line profiles from the Raystation data align with the intended outcomes. The profiles achieve the prescribed dose of 1.8 Gy per fraction inside the CTV volume and show sharp lateral penumbras. Furthermore, it is observed that the dose levels remain constant along the different depths in the CTV.

Several dissimilarities are observed when comparing the experimental and Raystation data. What appears evident from the experimental data is that the total signal is reduced at greater depths. The signal reduction at 60 mm depth is expected: at 60 mm, the detector was placed distally from the CTV. Therefore, it is desired to measure a low signal. However, at a depth of 10, 30, and 50 mm, instead of measuring a constant, high signal value, a signal reduction is observed, which decreases at greater depths. This signal reduction is present for all strategies, while it is measured the most for strategies 3, 5, and 6. Figure 6.4 displays the line profiles of strategy 5. Based on these experiments, there is an indication that an insufficient amount of dose is delivered halfway through the CTV and at the distal end of the CTV.

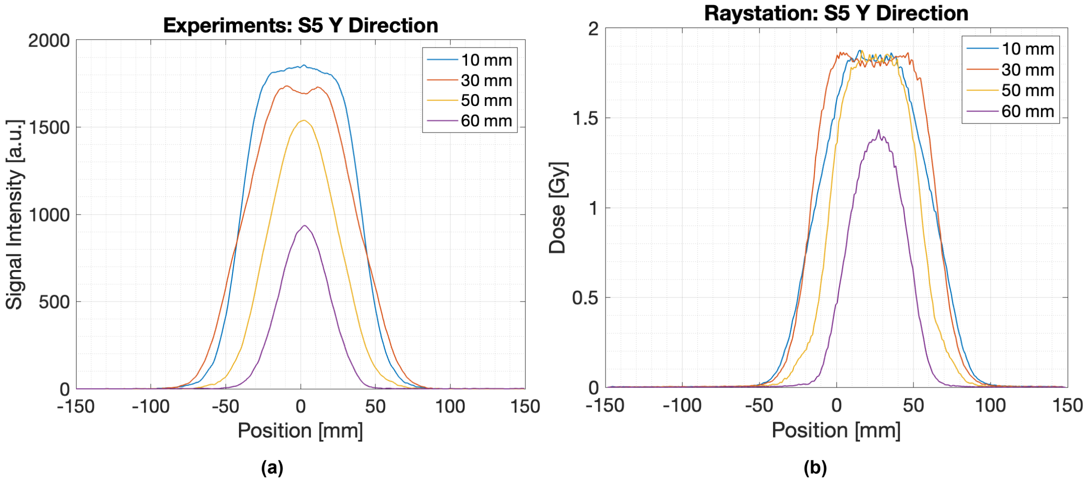

(a) (b)

Figure 6.4: The line profiles corresponding to strategy 5 along the Y-direction combined for each measured depth. Figure 6.4a represents the experimental data and figure 6.4b the Raystation data. Note that the experimental data is presented in signal intensity values and the Raystation data in dose.

Dose reduction halfway through the CTV

Another aspect that stands out from investigating the line profiles extracted from the experimental data is observed in the line profiles at 30 mm depth (i.e., halfway through the CTV). The profiles show an apparent signal reduction at the center of the CTV, both along the x- and y-direction. An overview of the line profiles along the y-direction at 30 mm depth is depicted in Figure 6.5. This effect is less pronounced at 10 mm and absent at 50 mm and 60 mm depth. Based on the visual assessment of the line profiles, this signal reduction is less evident in the Raystation data. This could be the result of the reduced resolution in the Raystation data or Monte Carlo noise.

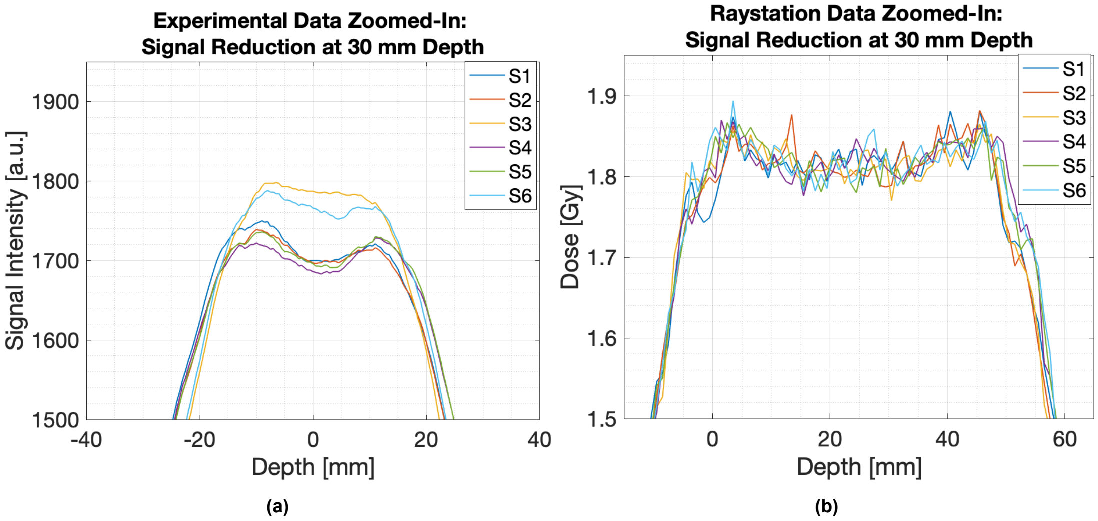

Figure 6.5: Combined line profiles at 30 mm depth for each strategy. Figure 6.5a represents the Experimental data, figure 6.5b the Raystation data. Note that the experimental data is presented in signal intensity values and the Raystation data in dose.

It was questioned whether the detected signal reduction affects the dose homogeneity of the CTV. This will be further analyzed in Section 6.3. Furthermore, an evaluation of the dose received by the OAR for the different strategies is presented in Section 6.4.

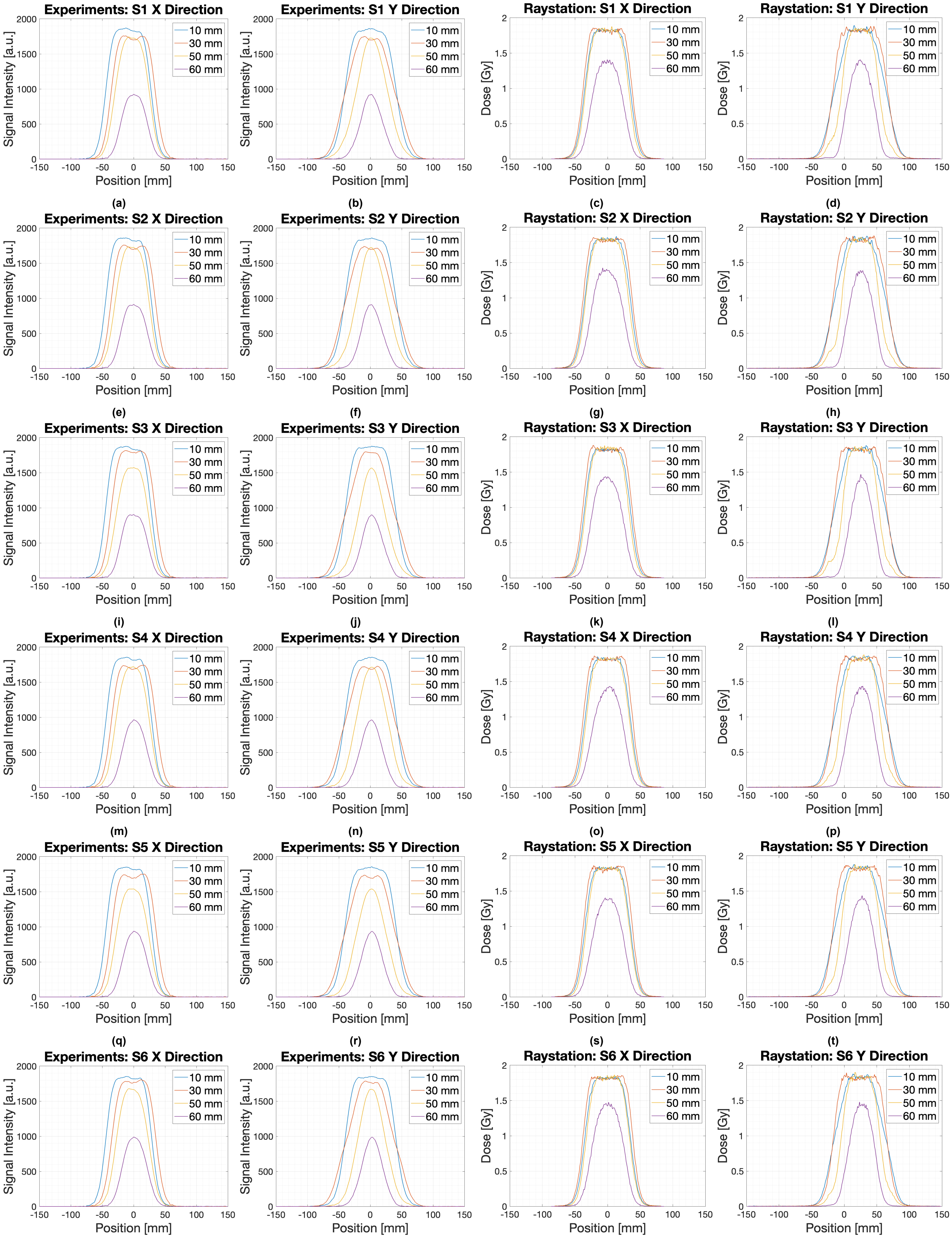

Experiments: S1 X Direction (a)

Experiments: S1 Y Direction (b)

Raystation: S1 X Direction (c)

Raystation: S1 Y Direction (d)

Experiments: S2 X Direction (e)

Experiments: S2 Y Direction (f)

Raystation: S2 X Direction (g)

Raystation: S2 Y Direction (h)

Experiments: S3 X Direction (i)

Experiments: S3 Y Direction (j)

Raystation: S3 X Direction (k)

Raystation: S3 Y Direction (l)

Experiments: S4 X Direction (m)

Experiments: S4 Y Direction (n)

Raystation: S4 X Direction (o)

Raystation: S4 Y Direction (p)

Experiments: S5 X Direction (q)

Experiments: S5 Y Direction (r)

Raystation: S5 X Direction (s)

Raystation: S5 Y Direction (t)

Experiments: S6 X Direction (u)

Experiments: S6 Y Direction (v)

Raystation: S6 X Direction (w)

Raystation: S6 Y Direction (x)

6.3. CTV coverage

The main objective of this thesis is to create treatment planning strategies with adequate CTV coverage. Therefore, in this section, it was assessed whether CTV coverage was achieved and which strategy scored best. When creating the treatment plans in Raystation, all plans acquired sufficient target coverage in the nominal plan and the robustly evaluated voxelwise minimum and maximum plan. Target coverage was achieved if 98% of the CTV volume received 95% of the prescribed dose (47.88 Gy). The results are presented in Table 6.1. In this section, the target coverage based on the experimental data is evaluated.

Table 6.1: Overview of the clinical goals for the CTV obtained from Raystation. The goal was to achieve a coverage level of 47.88 Gy in 98% of the CTV volume.

	Nominal plan [%]	Voxel-wise minimum [%]	Voxel-wise maximum [%]
Strategy 1	100	98.57	100
Strategy 2	100	98.27	100
Strategy 3	100	98.32	100
Strategy 4	100	98.76	100
Strategy 5	100	98.40	100
Strategy 6	100	98.60	100

6.3.1. CTV contouring

For an assessment of the dose delivered to the CTV, the measured signal inside the CTV area was compared. The dose was measured at three depths along the CTV: 10 mm, 30 mm, and 50 mm. The CTV area was determined by calculating the circular CTV with the radius corresponding to the considered depth, situated around the center point of each 2D plane (information on the determination of the center point is provided in Appendix F). The CTV contours projected onto the experimental data for strategy 1 are illustrated in Figure 6.7.

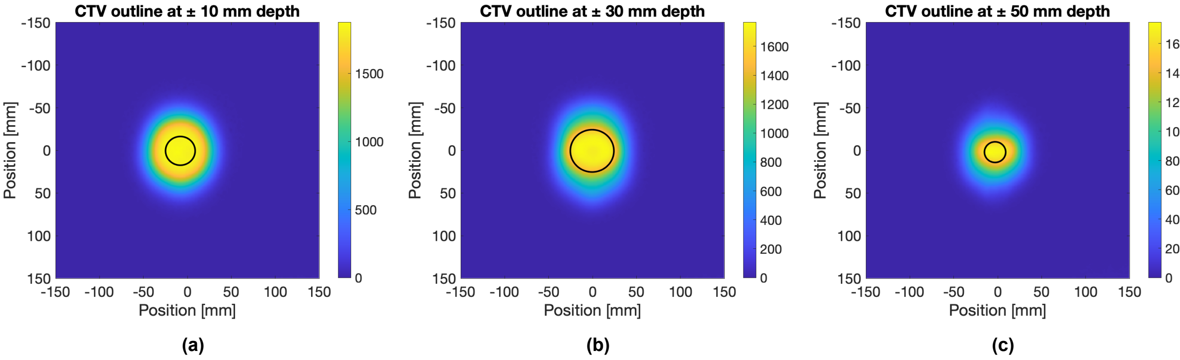

(a) (b) (c)

Figure 6.7: CTV contours projected onto the experimental data for strategy 1.

6.3.2. Assessment of CTV coverage

There are several ways to assess CTV coverage in radiation therapy. Tools that are often used include defining the percentage dose coverage level, the conformity index, and the homogeneity index [79], [77].

The first tool is often used to determine if a significant portion of the target volume has received a dose that meets a predefined threshold. A way to implement this is by determining if at least x% of the target volume receives x% of the prescribed dose. In this thesis, this tool was implemented in the treatment planning system to determine if the treatment plans achieved sufficient target coverage.

The specific settings that were employed were: 98% of the volume receives 95% of the prescribed dose.

The second tool includes determining the dose conformity. This defines to which extent the prescribed dose aligns with the CTV volume, e.g., how much of the volume receives the intended dose level. To quantitatively define the dose conformity of a treatment plan, the dose conformity index can be calculated:

$$\mathrm{CI} = \mathrm{VRI}/\mathrm{TV}, \tag{6.1}$$

with *CI* the conformity index, *VRI* the coverage of the volume by the prescribed dose and *TV* the target volume [77].

The last tool, the homogeneity index (HI), serves as a measure for assessing the uniformity of the dose within a defined volume. It is often used to define the ratio between the minimum and maximum dose inside a volume. It is described by the formula

$$\mathrm{HI} = \mathrm{D(x)}/\mathrm{D(100\text{-}x)}, \tag{6.2}$$

where *D* is the dose at a certain *x* percentage of a volume [77].

It was investigated which of the parameters mentioned above was the most eligible to apply to the experimental data in this thesis. The first two analysis methods are considered reliable in investigating the clinical target coverage goals. However, they rely on the usage of the prescribed dose to determine the coverage level. Since the experimental data is defined as signal intensity values and not in dose, comparing the results to a dose threshold was not possible. Therefore, these first two tools are not applicable to the data used in this thesis. The homogeneity index focuses on assessing dose field inhomogeneities, which had been identified in the prior experiments in Chapter 4. This tool aligns with the desired objectives, which include determining the effect of the clip on the radiation field and was therefore adopted to evaluate the dose in the CTV areas.

6.3.3. Homogeneity Index

The Homogeneity Index is described by formula 6.2. Since the measurement data is provided in signal intensity units, this serves as the input for the formula. The index is calculated by dividing *I(95)* by *I(5)*: *I(95)* is taken as the minimum intensity value in 95% of the volume and represents the minimum value in the CTV area. This measure is divided by *I(5)*, which is the minimum intensity value in 5% of the CTV area and represents the maximum value in the CTV area. This results in an index between 0 and 1, with 1 being the optimal outcome. For the Raystation data, the same method was applied, but with dose instead of signal intensity values. The HI is calculated for all strategies along the depths that measured an area inside the CTV (at 10, 30, and 50 mm). Note that the calculation for strategy 3 at 50 mm depth should be interpreted with caution since the iris setting of one of the beam angles was adjusted for this specific measurement. In Figure 6.8, the Homogeneity index values are displayed.

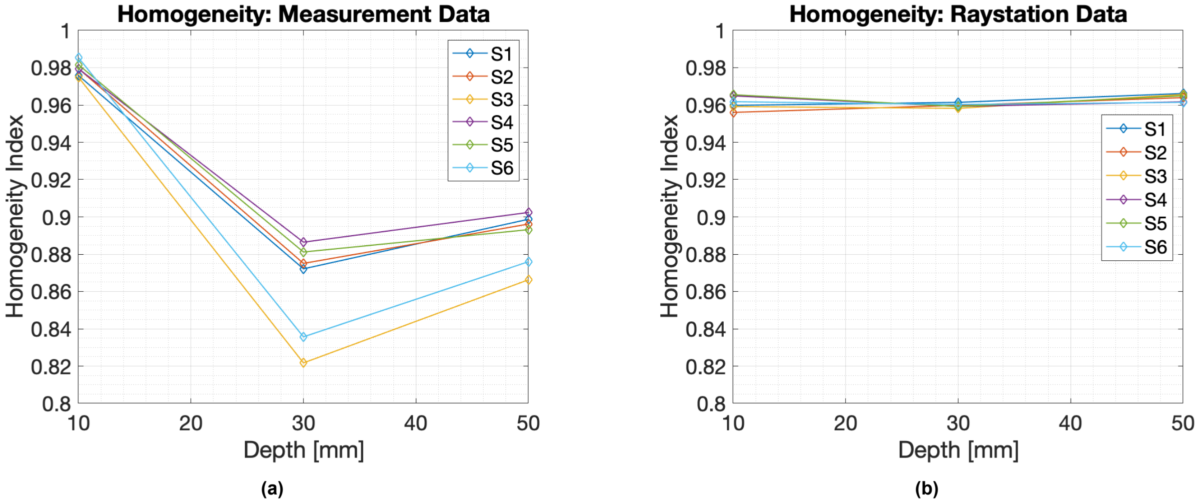

Figure 6.8: Calculated homogeneity indexes for the measurement data, figure 6.8a and Raystation data, figure 6.8b, at the measured depths along the CTV.

As was explained in Section 6.3.1, the determination of the CTV area relies on determining the central point of the radiation field; more information can be found in Appendix F. Using this method introduces uncertainty in determining the exact location of the CTV in the datasets. Moreover, given the detector's resolution of 0.5 mm, it is incapable of distinguishing details below this level. Therefore, an uncertainty margin of 0.5 mm was taken into account when determining the homogeneity index. This was done by shifting the center's location along the x- and y direction by 0.5 mm and recalculating the HI's for those scenarios.

In the bar charts in Figure 6.9, the homogeneity values per depth along the CTV are displayed separately. In the graphs, error bars are included, which indicate the effect of a 0.5 mm center shift error error.

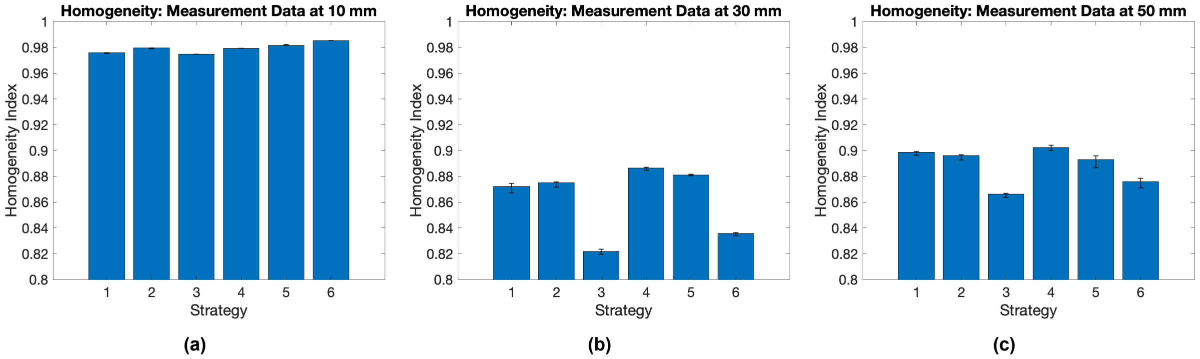

Figure 6.9: Calculated homogeneity indexes per depth, including an error bar representing the minimum and maximum calculated error for a 0.5 mm shift of the center of the field.

The uncertainty by a 0.5 mm shift was less than 1%. It was evaluated if the homogeneity indexes, including the error margins, differed per strategy. This was evaluated up to two decimal places. No statistical tests were performed since the data consists of one sample per measurement.

For the experiments performed at 10 mm depth, the overall mean HI scored the best: mean HI = 0.98. No difference was found between strategies 1, 2, 4, and 5 (HI = 0.98 ± 0.01). Only strategy 3 (HI = 0.97 ± 0.01) scored lower, and strategy 6 (HI = 0.99 ± 0.01) higher.

Regarding the experiments performed at 30 mm depth, the average calculated HI gained the lowest score: mean HI = 0.86. Strategy 3 (HI = 0.82 ± 0.01), followed by strategy 6 (HI = 0.84 ± 0.01), acquired the lowest indexes. The results of strategy 1 (HI = 0.87 ± 0.01) overlapped with strategy 2 but were lower than strategy 4 and 5. Strategies 2, 4, and 5 overlapped with each other (HI = 0.88 ± 0.01).

Compared to the measurements at 30 mm depth, the average calculated HI was higher at 50 mm depth: mean HI = 0.89. Here, strategies 3 and 6 scored the lowest index (HI = 0.87 ± 0.01). Strategies 1, 2, 4, and 5 achieved similar results (HI = 0.90 ± 0.01).

6.4. OAR sparing

In addition to the CTV coverage, the treatment plans were optimized to spare the OAR. To evaluate the OAR sparing, the experimental data of the different strategies was compared. The OAR is located at the distal end of the CTV. In one of the measurement setups, the Lynx detector was placed after 60 mm of RW3 plates, effectively measuring the signal throughout the OAR. Therefore, in this section, only the measurements performed at 60 mm depth are incorporated.

6.4.1. Dose in OAR

Absolute measured intensity

First, the signal in the OAR was compared in two points: point 1, the proximal end with respect to the beamline, and point 2, the distal end with respect to the beamline, see Figure 6.10a. In Figure 6.10b, one of the line profiles along the Y direction through the OAR is presented. The blue asterisk represents P1, and the red asterisk is P2. The exact locations of these points were determined based on the known geometry of the OAR.

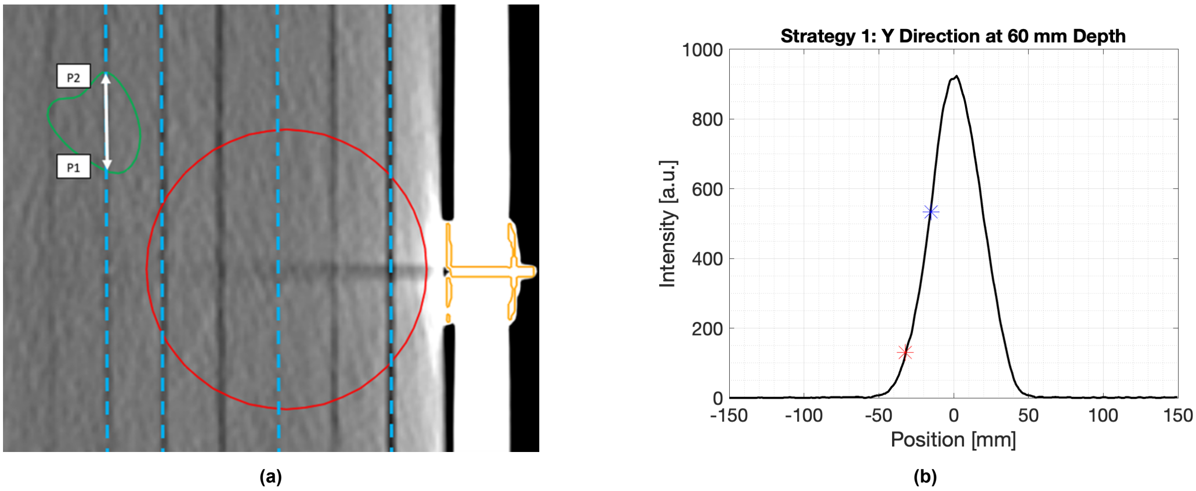

Figure 6.10: (a): A cross-section of the CT scan. The blue dashed lines represent the depths at which the detector was placed. The signal in the OAR is measured along the white arrow between P1, the most proximal point in the OAR, and P2, the most distal point in the OAR with respect to the beamline. (b): The line profile along the Y direction, measured at 60 mm depth for strategy 1. The blue asterisk represents P1 and the red asterisk P2.

The absolute measured signal is displayed in the bar chart in Figure 6.11. The error bars indicate the effect of a 0.5 mm center shift. Regarding the intensity measured at P1, at the proximal end of the OAR with respect to the beamline, the lowest signal was measured for strategy 3 (signal = 446), indicating the most favorable outcome. The highest signal was detected in strategy 4 (measured intensity = 566) with only a slight overlap in error margins compared to the signal in strategy 1. The error bars for strategies 2, 5, and 6 displayed overlap, and a minor degree of mutual overlap was observed between strategies 1 and 2 for their respective error bars.

When evaluating the signal measured at P2, the most distal end with respect to the beamline, the lowest signal was again detected for strategy 3 (signal = 70), although it slightly overlapped with strategy 2. The highest measured signal was detected in strategies 1 and 4 (130 and 131, respectively).

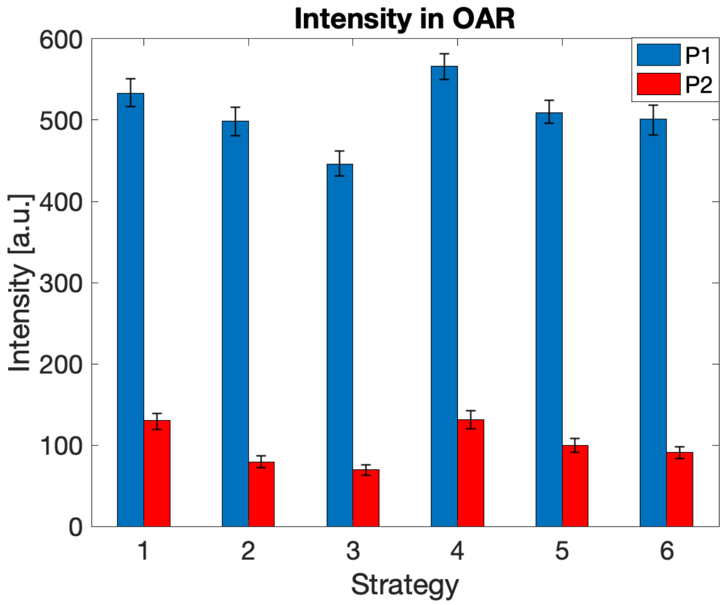

Figure 6.11: The bars represent the measured signal inside the OAR at two points. The error bars include the minimum and maximum calculated error for a 0.5 mm shift of the center of the field.

In order to obtain an indication of the total measured signal in the OAR, all data measured in the OAR along the line profile was summed. The calculation was performed along the cross-section of the y-profiles that measured the signal in the OAR (between the blue and red asterisk in Figure 6.10b). The results are presented in Table 6.2 and align with the previously presented findings.

Table 6.2: The total measured signal, measured along the line profile through the OAR, is depicted for each strategy.

	Strategy 1	Strategy 2	Strategy 3	Strategy 4	Strategy 5	Strategy 6
Total measured signal in OAR	$103(4)\times10^2$	$85(4)\times10^2$	$75(4)\times10^2$	$110(4)\times10^2$	$94(4)\times10^2$	$90(4)\times10^2$

6.4.2. OAR dose constraints

As was presented in Chapter 5.2.4, each treatment planning strategy was optimized with a different dose objective for the OAR. Table 6.3 presents an overview of the dose statistics regarding the OAR for each treatment planning strategy and the corresponding maximum and minimum dose according to Raystation. The maximum dose is represented as D1, which is calculated as the minimum dose in 1% of the OAR volume. The minimum dose is represented as D95, which is calculated as the minimum dose in 95% of the volume.

Table 6.3: Dose statistics for the OAR.

	Dose objective OAR [Gy]	Maximum Dose (D1) [Gy]	Minimum Dose (D95) [Gy]
Strategy 1	33.29	31.89	1.44
Strategy 2	31.85	30.87	1.19
Strategy 3	27.43	26.70	1.04
Strategy 4	33.26	31.68	1.46
Strategy 5	31.97	30.63	1.30
Strategy 6	33.00	31.13	1.30

Note that the dose objectives applied for the OAR in Raystation differ per strategy. Some strategies allowed for a lower dose objective than others. This should be taken into consideration when determining the OAR sparing. When comparing the results from Table 6.2 with the dose objectives presented in Table 6.3, it is observed that a lower dose objective also corresponds to a lower overall measured signal and vice versa.

6.4.3. Depth dose distribution

The advantage of employing proton therapy in contrast to photon therapy lies in the presence of sharp distal penumbras within proton therapy [80]. Therefore, an attempt has been made to obtain an indication of the distal dose fall-off of applied treatment plans. In Figure 6.12, the signal intensity at the center of the radiation field for each strategy and depth is depicted. This figure illustrates how the dose decreases beyond the target area. The signal fall-off was calculated by $\Delta y/\Delta x$, with Δy determined by taking the signal at 50 mm depth minus the signal at 60 mm depth and Δx being 10 mm. A higher value indicates a sharper fall-off. The results are depicted in Table 6.4.

It must be noted, however, that not only the steepness of the distal fall-off plays a role, but also the relatively measured intensity at 60 mm depth, where the OAR is located. Additional details on the lateral penumbra, e.g., the signal fall-off at the lateral sides of the field, are provided in Appendix H.

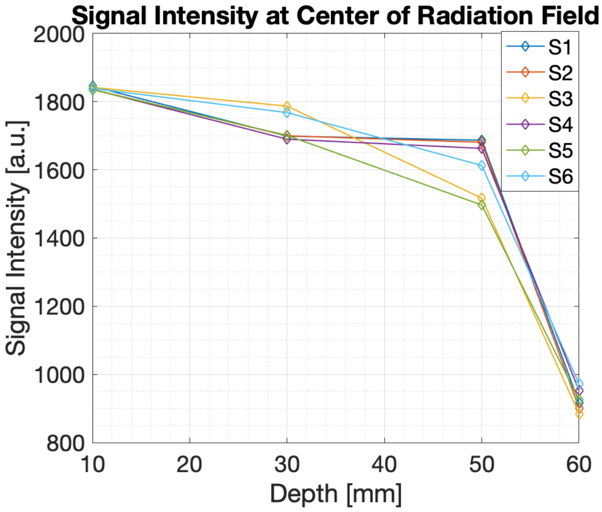

Figure 6.12: Signal intensity, measured at the center of the radiation field at every depth, for each strategy.

Table 6.4: This table presents the signal fall-off from 50 mm to 60 mm depth.

	Strategy 1	Strategy 2	Strategy 3	Strategy 4	Strategy 5	Strategy 6
Signal fall-off from 50 mm to 60 mm depth	77	78	63	71	57	64

7

Discussion and Conclusion

7.1. Interpretations and implications

This thesis aimed to create treatment planning strategies for proton therapy, that incorporate the presence of a titanium cranial fixation system. The most important interpretations and implications of the applied methodology and results are presented in this section.

7.1.1. Methodology

Designing the phantom and imaging

In this thesis, a basic phantom design composed of brain and bone equivalent materials was created, upon which the clip could be attached. The phantom served its intended purposes well: it was small and lightweight, and it was possible to easily transport and use it in the CT scanner, the R&D facility, and the clinical gantry. Additionally, it was easy to detach, which made it possible to position the detectors at different positions along the phantom.

The phantom was imaged by using CT since this is the main imaging modality used in proton therapy [50]. CT scans are highly susceptible to imaging artifacts in the presence of metal implants [14], [15], [16], [17]. Therefore, methods to address the negative consequences of these artifacts were investigated. The conducted literature review showed that the usage of an artifact reduction algorithm or density overrides to the materials affected by the artifacts, are adequate methods to eliminate artifacts. These methods were therefore adopted in this thesis. The importance of choosing the correct CT imaging protocol to accurately visualize the clip was also demonstrated. Based on the methodology employed in this thesis, a 1 mm CT acquisition protocol is recommended, because the quality of the image degrades quickly for 2 and 3 mm scanning protocols, which makes measuring the diameter of the clip more difficult and inaccurate.

Dose perturbation caused by the clip

This thesis presents an experimental method to investigate the dose perturbations caused by the cranial fixation clip. Several detection methods were investigated: the Lynx detector (IBA dosimetry), the OCTAVIUS detector (PTW dosimetry), and radiochromic films (EBT3). The Lynx detector was an effective tool to detect signal perturbations caused by the small titanium implant. It allows the identification of a signal distortion up to 0.5 mm, is easy to use, and provides direct, on-site digitization of the data.

The experiments showed that the presence of the clip in the radiation field created by a 150 MeV mono-energetic proton beam produces a measurable signal perturbation. This was presented as a signal reduction in the center of the radiation field and was measured in all experiments, with all proposed detection methods. The sharp edges of the clip created a local signal elevation, probably caused by multiple coulomb scattering. The presence of the clip affected the uniformity of the field by a reduction of 1 to 2% for most experimental setups. Only when the clip and detector were placed at the most distal end of the SOBP, a larger reduction in uniformity was detected. This indicates that the measured signal perturbation differs when varying the measurement position along the plateau of the SOBP.

The results of the Lynx detector were in line with the findings of the radiochromic film experiments. The radiochromic films have a very fine resolution and are often used for dosimetry. However, the usage of radiochromic films is accompanied by an increased workload and induces several uncertainties, as presented in Section 4.1.3. Therefore, the Lynx detector was chosen to be used over the films. Additionally, based on the presented findings, it is not recommended to use the OCTAVIUS detector to capture the effect of a small metal implant, such as the Flapfix system. This was mainly due to the detector's low resolution (5 mm), which created information loss compared to the Lynx detector.

Treatment planning strategies

This thesis presents a total of seven different treatment planning strategies specifically designed for the presence of titanium cranial fixation clips. The strategies were developed based on the findings of a systematic literature search (Appendix A) and their implementation relied on base experiments that explored the clip's effect on the radiation field. Six of the strategies were employed in the treatment planning system Raystation. Only the strategy, including an avoidance margin around the implant, did not meet the required clinical goals and was therefore excluded prior to commencing the experiments.

The strategies were designed according to four main concepts: implementing a density override on the clip, employing either an SFO or MFO technique, implementing beam-specific margins or not, and adding an avoidance margin on the implant. The treatment plans were robustly optimized for a ±3mm / ±3% uncertainty and met the clinical goals regarding CTV coverage (at least 98% of the target volume receives 95% of the maximum dose (47.88 Gy)) in the voxelwise minimum scenarios. Additionally, it was feasible to experimentally evaluate these strategies.

Treatment planning in Raystation

The treatment plans were made in the treatment planning system Raystation. A basic set of anatomical structures was created, including a spherical target volume and the addition of a small organ at risk. In addition to this, the components of the phantom, including the clip, were delineated. Delineating a metal implant is accompanied by several difficulties. This thesis provides a detailed explanation of the employed delineation process, which includes a combination of the proper level-window settings on the CT scan and using prior knowledge of the shape and size of the clip. The treatment plans were designed with two proton beams, separated by 60 degrees, and adding a range shifter was deemed necessary. A Monte Carlo dose calculation algorithm was employed based on the advantages presented in the literature review.

Experimental design

The experiments were performed in a clinical treatment room at HollandPTC. The detector was placed at varying depths through the phantom; after 10 mm, 30 mm, and 50 mm of RW3 plates, effectively measuring at the beginning, middle, and end of the CTV. Additionally, the detector was positioned after 60 mm of RW3 to measure the dose halfway through the OAR.

7.1.2. Experimental results

Effect of clip on radiation field

At first, an investigation was conducted to understand how Raystation integrated the clip into the treatment plans. From the 2D dose graphs extracted out of the TPS, it was observed that the clip was projected onto the radiation field as a dose reduction. The clip was projected twice, once for each beam, and shifted along with the beamline across the CTV.

Hereafter, the measured signal in the CTV was further evaluated by extracting line profiles through the center of the radiation field. When the line profiles were compared with each other, it was observed that the total signal was reduced at greater depths. This was in direct contrast to the data of the TPS, which presented a high, uniform signal at all depths. This contrast was measured for every strategy, although it was more pronounced for some strategies than others. This could indicate a disagreement between the dose calculated in the TPS and the delivered dose. However, there are possible other causes that contribute to this measured disagreement. One of these causes could be inaccuracies that occurred during the measurements, leading to range errors. Further elaboration on measurement uncertainties can be found in Section 7.2.2. Additionally, there could be a discrepancy in how Raystation calculates the range in the RW3 plates compared to the actual range. Additional research, in which a detection method capable of detecting dose, is needed to identify this disagreement further. The main focus must be to determine if the signal reduction exceeds clinical dose limits. Recommendations on possible detection methods will be discussed in Section 7.3.

In addition, further analysis of the experimental data highlighted a measured signal reduction at the center of the field when measurements were performed halfway through the CTV. This signal reduction was less pronounced at the beginning of the CTV. At the end of the CTV, at 50 mm depth, an overall signal reduction was measured, with more noticeable differences in some strategies compared to others. However, the specific reduction at the center of the field, as was present at 30 mm depth, was less evident. This might indicate either an absence of reduction at the center of the field or the presence of the clip could have affected the entire height of the peak. When compared to the TPS data, this observation was less apparent. The possible effects of this signal reduction on the homogeneity of the CTV were investigated subsequently.

CTV coverage

All treatment planning strategies were robustly optimized to acquire adequate CTV coverage. This was achieved if 98% of the CTV volume received 95% of the prescribed dose (47.88 Gy). The homogeneity index was used to evaluate the CTV coverage of the experimental data. Regardless of the applied strategies, the homogeneity calculated from the experimental data was worse than the homogeneity calculated from the TPS data. Interestingly, the HI was observed to differ significantly per measured depth. The average calculated HI was best at 10 mm (mean HI = 0.98), and decreased when measured at 30 mm (mean HI = 0.86), and 50 mm depth (mean HI = 0.89). When comparing the different strategies, it was found that the strategies employing MFO techniques produced a more inhomogeneous signal in the CTV than those employing SFO methods. Based on the presented results, the addition of beam-specific margins around the CTV did not evidently alter the measured homogeneity. The same applies to the addition of a density override to the clip.

Together, these results provide important insights into the overall field inhomogeneities caused by the clip. There is a strong indication that the field homogeneity inside the target volume gets perturbed by the clip, and it was questioned whether this exceeds clinically acceptable limits. To gain a complete understanding of whether these inhomogeneities exceed clinical limits, additional studies that focus on measuring the absolute dose inside the CTV will be needed. Recommendations for future studies are further discussed in Section 7.3.

OAR sparing

In addition to CTV coverage, it was investigated to what extent the different treatment planning strategies could spare the OAR. Overall, in the strategies that employed an MFO technique (strategies 3 and 6), the lowest amount of signal was measured inside the OAR, indicating that these methods were best at sparing the OAR. In addition to that, strategy 2, which is created based on an SFO technique and the usage of a density override on the clip, scored similar results to strategy 6. In strategies 1 and 4, which employed an SFO technique and the use of beam-specific margins, the highest signal levels were detected. These results imply that an SFO method, in combination with the usage of beam-specific margins, results in a diminished capability to spare critical organs.

Treatment planning strategies

One of the goals of this thesis was to determine which treatment planning strategy is best to use in the presence of the cranial fixation clip. Based on the results presented, strategies 2 and 5 showed the most favorable outcomes when considering the clinical goals regarding CTV coverage and OAR sparing. However, to provide a conclusive decision on the strategy to use, it is necessary to perform additional research, which focuses on measuring the dose inside the CTV and OAR when applying the different strategies.

7.2. Limitations

7.2.1. Lynx detector

The experiments presented in this thesis were conducted using the Lynx detector, and as was mentioned previously, this detector cannot currently provide output in terms of dose in Gray. This results in two main limitations for this thesis.

First, since the signal was not measured in dose, the presented results must be interpreted with caution. The results show that the presence of the clip in the radiation field affects the field homogeneity when considering the signal provided by the Lynx detector. However, there remains the need to investigate how this affects the absolute measured dose inside the CTV.

Secondly, this limitation affected the ability to compare the experimental results with the Raystation data. It was not possible to apply a gamma analysis [81]. This analysis method compares the dose measured in experiments or during quality assurance with the dose from a treatment planning system [82]. This method is a well-established protocol for dose verification in photon radiation therapy quality assurance [83], [84]. Additionally, it is increasingly applied in proton therapy [85], [86]. It determines the dose difference based on a predefined dose difference level and a distance to agreement criteria, which results in an index that can be used to assess the outcomes. Based on this index, it is determined if the measured dose resembles the intended dose from the treatment planning system or not. However, it was not possible to apply this tool for data analysis. This limits the capability of comparing the measured results with the data from the TPS. Nevertheless, a relative comparison between the experimental data and Raystation data was applied. This outlined the presence of several types of dissimilarities. Additional research is needed to better understand the agreement between the TPS and outcomes of a Lynx detector. One approach to achieve this is through the process of calibrating the Lynx detector. Another approach is to investigate the usage of other detection methods further. This will be further elaborated on in Section 7.3.

7.2.2. Measurement uncertainties

During the measurement process, measurement uncertainties and inaccuracies might have occurred. In the experiments performed in the treatment room using the clinical gantry, presented in Chapter 5, the phantom was positioned using the in-room laser system. The lasers were used to align the isocenter of the treatment plans on the phantom. However, the laser system has a limited accuracy of ± 2 mm. This introduces a systematic error in all the data along all axes (e.g., the horizontal, vertical, and depth axes). In addition to this, to measure at different depths, RW3 plates were removed from the phantom. When switching to a different depth, the distance between the phantom and detector was kept constant. This was achieved through the utilization of a ruler and the laser system. This also introduces a systematic error. This error only concerns the comparison between measurement depths since the phantom remained untouched between the change in treatment planning strategy and beam angle. Lastly, to compare the experimental data with the Raystation data, it was necessary to extract 2D dose planes from the 3D volume. This also introduces a possible range uncertainty.

7.2.3. Delineation of the ROIs

The part of the phantom representing the brain is solely comprised of RW3 plates. This means that it does not include any other materials, representing for example different types of tissues or air cavities. Therefore, it was required to manually delineate the CTV and OAR structures and decide on their size and shape. It was chosen to contour a perfectly round-shaped sphere to represent the CTV volume. The size of the CTV was supported by literature, and the choice of the spherical shape was selected because of the necessity to ascertain the precise geometry for data analysis. An irregularly shaped CTV would have made it difficult to determine the sectional geometrical boundaries of the CTV during data analysis. However, it is likely that the choice of the CTV's shape affects the experimental outcomes when considering the underlying working principles of the employed optimization techniques.

SFO relies on delivering the dose to the target volume by optimizing each field separately. This means that during the optimization process, the optimization of one field is not dependent on the optimization of other fields. Therefore, this method is relatively robust against setup errors. MFO, on the other hand, optimizes all fields together, which makes it more efficient in sparing organs at risk. However, this does make it more susceptible to setup errors.

When reflecting on the performed experiments, it is hypothesized that a more irregularly shaped CTV would have introduced less favorable outcomes for the employed SFO methods. Additionally, setup errors are nearly absent in the experiments since the phantom includes few tissue heterogeneities and was statically positioned. The only source of uncertainty could have been introduced by aligning the clip to the beam's center. A clinical scenario where setup uncertainties are an important source of treatment inaccuracies probably impacts the outcomes of the strategies where MFO techniques are applied.

Additionally, it was found in the experiments that the dose distribution in the CTV was relatively inhomogeneous. It was questioned whether selecting a different CTV shape, for example a cuboid, would have made the comparison between the different depths along the CTV better interpretable. Subsequently, this could have better enhanced the comparability between the different strategies and the measurements versus the TPS. Nevertheless, a cuboid-shaped CTV is less clinically relevant and more difficult to optimize with some of the presented optimization techniques. Further work could elaborate on the considerations involved in selecting the OAR and CTV.

Furthermore, the delineation of the clip posed a challenging aspect. Imaging high-density materials already introduces difficulties with CT imaging of the clip. Additionally, significant variations in the representation of the clip were observed when applying different level window settings, and the presence of the small structures in the clip further complicated the visualization and delineation of the clip. Attempts were made to delineate the clip precisely by using the knowledge of the shape and size of the clip, but inaccuracies are present, particularly at the edges of the clip and in capturing the specific shape of the clip. It is advisable to take careful consideration in the delineation of metal implants in future studies. The methods presented in Appendix E.1 can be consulted for assistance.

7.2.4. Methodology of assessing the dose objectives in the OAR

The methodology to determine the dose objectives inside the OAR is evaluated in Section 5.2.4. The purpose of adopting this approach was to mirror a clinically realistic assessment strategy. However, alternative approaches could have led to different trade-offs and consequently different dose objectives for the OAR. Additionally, in a clinical scenario, there are often more OARs present, increasing the clinical goals that must be met. It is important to keep this in mind for potential follow-up studies and take careful consideration in determining the dose objectives for the OAR.

7.2.5. Overlapping ROIs

In Section 5.2.2, the process of delineating the regions of interest on the CT scan was enlightened. At the end of this project, after the treatment plans were made and the experiments were conducted, a delineation inaccuracy was detected. This inaccuracy included the delineation of the RW3 plates and clip: it was found that the bottom disk of the clip overlapped with the RW3 ROI. Since a density override of RW3 was added to the RW3 ROI, this resulted in an override of RW3 to a part of the bottom disk of the clip. This is an inaccuracy that likely had an impact on the results and was, therefore further investigated.

To assess the impact, two scenarios were recalculated in Raystation. First, a scenario in which the ROI of the clip was subtracted from the ROI of the RW3 plates, see Figure 7.1b. This will be referred to as scenario A. Secondly, a scenario in which the ROI of the RW3 plates was subtracted from the ROI of the clip was investigated, see Figure 7.1c. This will be referred to as scenario B.

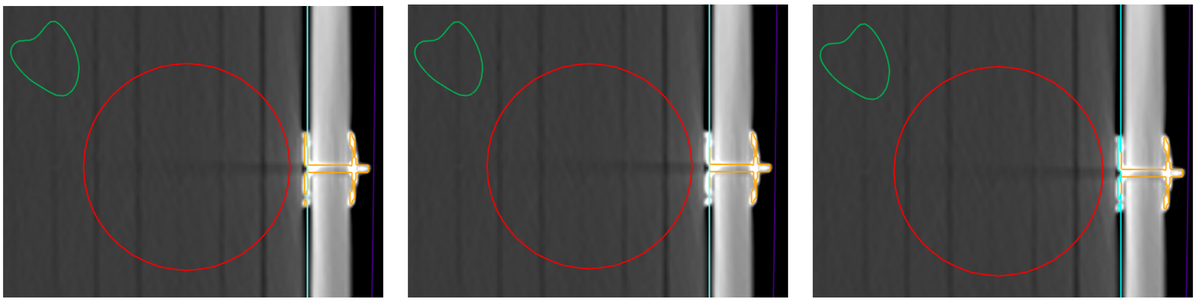

(a) (b) (c)

Figure 7.1: Figure 7.1a visualizes the delineation applied in the experiments. As is visible, the RW3 ROI overlaps with the clip. Figure 7.1b displays scenario A. Figure 7.1c displays scenario B.

All treatment plans were recalculated for these scenarios. The dose differences were evaluated to gain a better comprehension of the consequences. In Figure 7.2a, the dose distribution for treatment planning strategy 1 is displayed. Figure 7.2b visualizes the dose difference between the treatment plan for strategy 1, compared to the same treatment plan, recalculated scenario A. Figure 7.2c displays the dose difference between the treatment plan for strategy 1, compared to the same treatment plan, recalculated on scenario B.

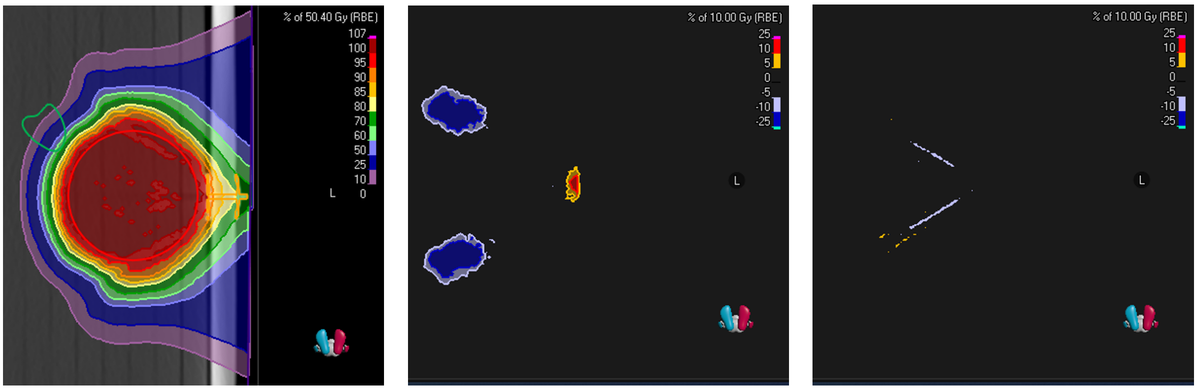

(a) (b) (c)

Figure 7.2: Figure 7.2a visualizes the calculated dose for strategy 1, as was applied in the experiments. Figure 7.2b displays the dose difference between the dose for strategy 1 and the dose calculated for scenario A. Figure 7.2c displays the dose difference between the dose in strategy 1 and the dose calculated for scenario B.

Figure 7.2 illustrates that the inaccuracy particularly affects the dose measured at the areas distal to the CTV. Therefore, this inaccuracy probably has influenced the way in which the OAR dose objectives were determined. In addition to this, the line profiles at the depths on which the measurements were performed were evaluated in Raystation for the different scenarios. The results are presented in Figure 7.3. Only small differences are visible, which are a bit more pronounced at 50 and 60 mm depth.

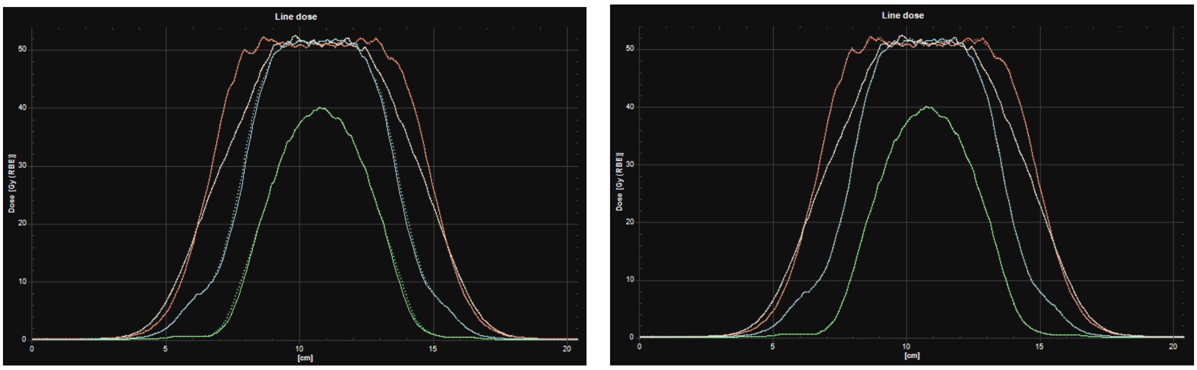

(a)

(b)

Figure 7.3: The solid line presents the calculated dose for strategy 1, as was applied in the experiments. In Figure 7.3a, the comparison between the dose for strategy 1 and scenario A is visualized, where the latter is displayed by the dotted line. In Figure 7.3b, the dose for scenario B is displayed by the dotted line. The white line profiles are measured after 10 mm of RW3, the orange line profiles at 30 mm of RW3, the blue profiles at 50 mm of RW3, and the green profiles at 60 mm of RW3.

Furthermore, the minimum dose inside the CTV and maximum dose inside the OAR were evaluated and are listed in Table 7.1. The consequences for the dose inside the CTV and OAR are limited. A greater impact is measured on the plans with a density override (strategies 1, 2, and 3) compared to the plans without a density override (strategies 4, 5, and 6). Overall, it can be deduced that the magnitude of impact resulting from this delineation inaccuracy was relatively small.

Table 7.1: This table summarizes the maximum dose in the OAR and minimum dose in the CTV when considering the original plan applied in the experiments in this thesis, scenario A and scenario B.

	D1 OAR Original Plan	D1 OAR Scenario A	D1 OAR Scenario B	D98 CTV Original Plan	D98 CTV Scenario A	D98 CTV Scenario B
Strategy 1	31.89	31.96	31.95	49.91	49.90	49.88
Strategy 2	30.87	31.01	30.84	49.81	49.79	49.79
Strategy 3	26.70	26.76	26.69	49.75	49.73	49.73
Strategy 4	31.68	31.68	31.61	49.86	49.86	49.86
Strategy 5	30.63	30.63	30.49	49.83	49.83	49.84
Strategy 6	31.13	31.13	31.08	49.71	49.71	49.72

7.3. Recommendations for future work

This research provides guidelines for an experimental method to investigate the effect of a cranial fixation clip on the radiation field. One of the key aspects for further research is assessing whether the measured field inhomogeneities affect clinical dose limits. As was mentioned in Section 7.2, one of the main limitations of this study is that the currently used detection method did not provide outcomes in terms of dose in Gray. Therefore, further work should elaborate on using detection methods for absolute dosimetry.

The Lynx detector, used in the measurements involving the different treatment planning strategies, served as an adequate detection method: it has high resolution and provides easy and quick on-site analysis. Therefore, it is recommended to reuse this detector in future experiments and focus on its calibration so that it can be applied to absolute dosimetry. Consultation of the article written by Russo et al. is recommended, which characterized the detector and investigated the linearity of the detector [59].

In addition to this, other type of detection methods could be further investigated. The literature review found that ionization chamber detectors are commonly used in experiments like the ones presented in this thesis or for quality assurance purposes. The OCTAVIUS detector, used in the experiments performed in the experimental bunker, presented in Chapter 4, is also an ionization chamber detector with ±5 mm resolution. However, the low resolution resulted in information loss, which is why it is not recommended. One could consider the usage of ionization chamber detectors offering enhanced resolution.

Furthermore, a detection method that was largely applied in the articles incorporated in the literature review is radiochromic films. Calibrated films can be used in absolute dosimetry. However, this method presents several challenges and uncertainties, as was discussed in Section 4.1.3. This research can be expanded by incorporating the use of radiochromic films, but it is crucial to carefully account for the related uncertainties in the process.

As another recommendation, the presented experimental methods can serve as the basis for future research to investigate other types of implants. If research is conducted on implants at other locations in the body, one can reassess strategy 7, which included setting an avoidance region around the implant. According to this thesis, this strategy is not an effective treatment planning strategy for the current scenario. However, it should be reconsidered when evaluating implants in different body parts. Furthermore, a follow-up study could focus on establishing how the presented strategies can be applied to clinical patient data.

7.4. Conclusion

To our knowledge, no research has been published on the effects of the Flapfix cranial fixation system on proton therapy. By performing measurements on a mono-energetic beamline, it has been shown that the effect of the clip in the radiation field is measurable and affects the field uniformity. This thesis presented six treatment planning strategies that incorporate the presence of a titanium clip. These strategies were successfully implemented into the treatment planning system Raystation and were evaluated by performing experiments. Based on the results of the conducted experiments, there is a strong indication that the field homogeneity inside the target volume gets perturbed by the clip. This indicates a high need to investigate the clinical implications of this further. In particular, absolute dose measurements must be added to the presented results.

References

[1] *NKR Cijfers*, [Online; accessed 5. Jul. 2023], Jul. 2023. [Online]. Available: `https://iknl.nl/nkr-cijfers`.

[2] *Brain Tumor Types*, [Online; accessed 26. Oct. 2023], Nov. 2021. [Online]. Available: `https://www.hopkinsmedicine.org/health/conditions-and-diseases/brain-tumor/brain-tumor-types`.

[3] M. M. Vargo, "Brain Tumors and Metastases," *Phys. Med. Rehabil. Clin. N. Am.*, vol. 28, no. 1, pp. 115–141, Feb. 2017, ISSN: 1047-9651. DOI: `10.1016/j.pmr.2016.08.005`.

[4] *Brain Tumor Types, Glioblastoma, Meningioma & More*, [Online; accessed 26. Oct. 2023], Jan. 2020. [Online]. Available: `https://miamineurosciencecenter.com/en/conditions/brain-tumors/types`.

[5] R. Grant, T. Dowswell, E. Tomlinson, *et al.*, "Interventions to reduce the time to diagnosis of brain tumours," *Cochrane Database of Systematic Reviews*, vol. 2020, no. 9, 2020. DOI: `10.1002/14651858.CD013564.pub2`.

[6] M. Lambrecht, D. B. P. Eekers, C. Alapetite, *et al.*, "Radiation dose constraints for organs at risk in neuro-oncology; the European Particle Therapy Network consensus," *Radiother. Oncol.*, vol. 128, no. 1, pp. 26–36, Jul. 2018, ISSN: 1879-0887. DOI: `10.1016/j.radonc.2018.05.001`. eprint: `29779919`.

[7] *Advances in Brain and Spinal Cord Tumor Research*, [Online; accessed 26. Oct. 2023], Oct. 2023. [Online]. Available: `https://www.cancer.gov/types/brain/research`.

[8] *Brain Tumor Surgery*, [Online; accessed 26. Oct. 2023], Apr. 2022. [Online]. Available: `https://www.hopkinsmedicine.org/health/conditions-and-diseases/brain-tumor/brain-tumor-surgery`.

[9] M. Piccirilli, G. Spena, E. Marchese, M. P. Tropeano, and A. Santoro, "A new device for bone cranial flap fixation: Technical note and surgical remarks. A multicentric experience," *Surgical Neurology International*, vol. 12, 2021. DOI: `10.25259/SNI_819_2020`.

[10] W. B. et al., "Titanium miniplates or stainless steel wire for cranial fixation: a prospective randomized comparison," *J. Neurosurg.*, vol. 96, 2002. DOI: `10.3171/jns.2002.96.2.0244`.

[11] *Brain Tumors: Radiation Therapy - Health Encyclopedia - University of Rochester Medical Center*, [Online; accessed 26. Oct. 2023], Oct. 2023. [Online]. Available: `https://www.urmc.rochester.edu/encyclopedia/content.aspx?contentid=17829-4&contenttypeid=34`.

[12] C. Scaringi, L. Agolli, and G. Minniti, "Technical Advances in Radiation Therapy for Brain Tumors," *Anticancer Res.*, vol. 38, no. 11, pp. 6041–6045, Nov. 2018, ISSN: 0250-7005. DOI: `10.21873/anticanres.12954`.

[13] J. Vogel, R. Carmona, C. G. Ainsley, and R. A. Lustig, "The Promise of Proton Therapy for Central Nervous System Malignancies," *Neurosurgery*, vol. 84, no. 5, p. 1000, Nov. 2018, ISSN: 0148-396X. DOI: `10.1093/neuros/nyy454`.

[14] R. Righetto, L. P. Clemens, S. Lorentini, *et al.*, "Accurate proton treatment planning for pencil beam crossing titanium fixation implants," *Phys. Med.*, vol. 70, pp. 28–38, Feb. 2020, ISSN: 1724-191X. DOI: `10.1016/j.ejmp.2020.01.003`. eprint: `31954210`.

[15] Depauw, *Practical Radiation Oncology*, Feb. 2023, ISSN: 1879-8500. DOI: `10.1016/j.prro.2023.01.009`.

[16] R. Poel, F. Belosi, F. Albertini, *et al.*, "Assessing the advantages of CFR-PEEK over titanium spinal stabilization implants in proton therapy-a phantom study," *Phys. Med. Biol.*, vol. 65, no. 24, p. 245031. Dec. 2020, ISSN: 1361-6560. DOI: `10.1088/1361-6560/ab8ba0`. eprint: `32315991`.

[17] D. J. Indelicato, R. L. Rotondo, D. Begosh-Mayne, *et al.*, “A Prospective Outcomes Study of Proton Therapy for Chordomas and Chondrosarcomas of the Spine,” *International Journal of Radiation Oncology∗Biology∗Physics*, vol. 95, no. 1, pp. 297–303, May 2016, ISSN: 0360-3016. DOI: `10.1016/j.ijrobp.2016.01.057`.

[18] A. Pehlivanl and M. H. Blkdemir, “Investigation of the effects of biomaterials on proton Bragg peak and secondary neutron production by the Monte Carlo method in the slab head phantom,” *Appl. Radiat. Isot.*, vol. 180, p. 110 060, Feb. 2022, ISSN: 0969-8043. DOI: `10.1016/j.apradiso.2021.110060`.

[19] *ProBeam | Varian*, [Online; accessed 22. Nov. 2023], Nov. 2023. [Online]. Available: `https://www.varian.com/products/proton-therapy/treatment-delivery/probeam`.

[20] W. D. Newhauser and R. Zhang, “The physics of proton therapy,” *Phys. Med. Biol.*, vol. 60, no. 8, R155, Mar. 2015, ISSN: 0031-9155. DOI: `10.1088/0031-9155/60/8/R155`.

[21] D. R. Grimes, D. R. Warren, and M. Partridge, “An approximate analytical solution of the Bethe equation for charged particles in the radiotherapeutic energy range,” *Sci. Rep.*, vol. 7, no. 9781, pp. 1–12, Aug. 2017, ISSN: 2045-2322. DOI: `10.1038/s41598-017-10554-0`.

[22] A. Beddok, A. Vela, V. Calugaru, *et al.*, “Proton therapy for head and neck squamous cell carcinomas: A review of the physical and clinical challenges,” *Radiother. Oncol.*, vol. 147:30-39. Jun. 2020, ISSN: 1879-0887. DOI: `10.1016/j.radonc.2020.03.006`. eprint: `32224315`.

[23] R. W. Mutter and N. B. Remmes, “Initial clinical experience of postmastectomy intensity modulated proton therapy in patients with breast expanders with metallic ports,” *Practical Radiation Oncology*, vol. 7, no. 4, e243–e252, Jul. 2017, [Online; accessed 20. Apr. 2023], ISSN: 1879-8500. DOI: `10.1016/j.prro.2016.12.002`.

[24] F. Fellin, M. Artoni, R. Righetto, *et al.*, “An avoidance method to minimize dose perturbation effects in proton pencil beam scanning treatment of patients with small high-Z implants,” *Phys. Med. Biol.*, vol. 65, no. 14, 14NT01, Jul. 2020, ISSN: 0031-9155. DOI: `10.1088/1361-6560/ab9775`.

[25] A. Fredriksson, A. Forsgren, and B. Hårdemark, “Minimax optimization for handling range and setup uncertainties in proton therapy,” *Med. Phys.*, vol. 38, no. 3, pp. 1672–1684, Mar. 2011, ISSN: 0094-2405. DOI: `10.1118/1.3556559`. eprint: `21520880`.

[26] C. M. DeCesaris, S. Mossahebi, J. Jatczak, *et al.*, “Outcomes of and treatment planning considerations for a hybrid technique delivering proton pencil-beam scanning radiation to women with metal-containing tissue expanders undergoing post-mastectomy radiation,” *Radiother. Oncol.*, vol. 164, pp. 289–298, Nov. 2021, ISSN: 0167-8140. DOI: `10.1016/j.radonc.2021.07.012`.

[27] Y. Kang, J. Shen, M. Bues, Y. Hu, W. Liu, and X. Ding, “Technical Note: Clinical modeling and validation of breast tissue expander metallic ports in a commercial treatment planning system for proton therapy,” *Med. Phys.*, vol. 48, no. 11, pp. 7512–7525, Nov. 2021, ISSN: 2473-4209. DOI: `10.1002/mp.15225`. eprint: `34519357`.

[28] M. Kirk, G. Freedman, T. Ostrander, and L. Dong, “Field-Specific Intensity-modulated Proton Therapy Optimization Technique for Breast Cancer Patients with Tissue Expanders Containing Metal Ports,” *Cureus*, vol. 9, no. 9, e1698. Sep. 2017, ISSN: 2168-8184. DOI: `10.7759/cureus.1698`. eprint: `29159005`.

[29] L. Zhao, V. P. Moskvin, C.-W. Cheng, and I. J. Das, “Dose perturbation caused by metallic port in breast tissue expander in proton beam therapy,” *Biomed. Phys. Eng. Express*, vol. 6, no. 6, p. . Nov. 2020, ISSN: 2057-1976. DOI: `10.1088/2057-1976/abc899`. eprint: `34035189`.

[30] M. Zhu, K. Langen, E. M. Nichols, *et al.*, “Intensity Modulated Proton Therapy Treatment Planning for Postmastectomy Patients with Metallic Port Tissue Expanders,” *Adv. Radiat. Oncol.*, vol. 7, no. 1, p. 100825. Oct. 2021, ISSN: 2452-1094. DOI: `10.1016/j.adro.2021.100825`. eprint: `34805622`.

[31] K. Kisielewicz, E. Gra, T. Skra, *et al.*, “Safe Proton Radiotherapy for Patients with Metallic Spine Stabilization System,” *Acta Phys. Pol. A*, vol. 142, no. 3, pp. 351–355, Sep. 2022, ISSN: 0587-4246. DOI: `10.12693/APhysPolA.142.351`.

[32] Y.-H. Hu, W. C. T. H. Seum, A. Hunzeker, O. Muller, R. L. Foote, and D. W. Mundy, “The effect of common dental fixtures on treatment planning and delivery for head and neck intensity modulated proton therapy,” *J. Appl. Clin. Med. Phys.*, vol. 24, no. 7, e13973. Jul. 2023, ISSN: 1526-9914. DOI: `10.1002/acm2.13973`. eprint: `36972299`.

[33] C. Shi, H. Lin, S. Huang, *et al.*, “Comprehensive Evaluation of Carbon-Fiber-Reinforced Polyetheretherketone (CFR-PEEK) Spinal Hardware for Proton and Photon Planning,” *Technol. Cancer Res. Treat.*, vol. 21, p. 15330338221091700. Jan. 2022, ISSN: 1533-0338. DOI: `10.1177/15330338221091700`. eprint: `35410544`.

[34] S. Rana, C. Cheng, Y. Zheng, *et al.*, “Dosimetric study of uniform scanning proton therapy planning for prostate cancer patients with a metal hip prosthesis, and comparison with volumetric-modulated arc therapy,” *J. Appl. Clin. Med. Phys.*, vol. 15, no. 3, p. 4611. May 2014, ISSN: 1526-9914. DOI: `10.1120/jacmp.v15i3.4611`. eprint: `24892333`.

[35] E. J. Tryggestad, W. Liu, M. D. Pepin, C. L. Hallemeier, and T. T. Sio, “Managing treatment-related uncertainties in proton beam radiotherapy for gastrointestinal cancers,” *Journal of Gastrointestinal Oncology*, vol. 11, no. 1, p. 212, Feb. 2020. DOI: `10.21037/jgo.2019.11.07`.

[36] Z. Yang, Y. Chang, K. K. Brock, *et al.*, “Effect of setup and inter-fraction anatomical changes on the accumulated dose in CT-guided breath-hold intensity modulated proton therapy of liver malignancies,” *Radiother. Oncol.*, vol. 134:101-109. May 2019, ISSN: 1879-0887. DOI: `10.1016/j.radonc.2019.01.028`. eprint: `31005203`.

[37] Y. Jia, L. Zhao, C.-W. Cheng, M. W. McDonald, and I. J. Das, “Dose perturbation effect of metallic spinal implants in proton beam therapy,” *J. Appl. Clin. Med. Phys.*, vol. 16, no. 5, p. 333, Sep. 2015. DOI: `10.1120/jacmp.v16i5.5566`.

[38] P. Farace, R. Righetto, and M. Cianchetti, “Single-energy intensity modulated proton therapy,” *Phys. Med. Biol.*, vol. 60, no. 19, pp. 357–367, Oct. 2015, ISSN: 1361-6560. DOI: `10.1088/0031-9155/60/19/N357`. eprint: `26352616`.

[39] D. Pflugfelder, J. J. Wilkens, and U. Oelfke, “Worst case optimization: a method to account for uncertainties in the optimization of intensity modulated proton therapy,” *Phys. Med. Biol.*, vol. 53, no. 6, pp. 1689–1700, Mar. 2008, ISSN: 0031-9155. DOI: `10.1088/0031-9155/53/6/013`. eprint: `18367797`.

[40] J. Unkelbach, T. Bortfeld, B. C. Martin, and M. Soukup, “Reducing the sensitivity of IMPT treatment plans to setup errors and range uncertainties via probabilistic treatment planning,” *Med. Phys.*, vol. 36, no. 1, pp. 149–163, Jan. 2009, ISSN: 0094-2405. DOI: `10.1118/1.3021139`. eprint: `19235384`.

[41] E. W. Korevaar, S. J. M. Habraken, D. Scandurra, *et al.*, “Practical robustness evaluation in radiotherapy – A photon and proton-proof alternative to PTV-based plan evaluation,” *Radiother. Oncol.*, vol. 141, pp. 267–274, Dec. 2019, ISSN: 0167-8140. DOI: `10.1016/j.radonc.2019.08.005`.

[42] A.-M. Oros-Peusquens, R. Louo, Z. Abbas, V. Gras, M. Zimmermann, and N. J. Shah, “A Single-Scan, Rapid Whole-Brain Protocol for Quantitative Water Content Mapping With Neurobiological Implications,” *Front. Neurol.*, vol. 10, p. 471 036, Dec. 2019, ISSN: 1664-2295. DOI: `10.3389/fneur.2019.01333`.

[43] *IBA Dosimetry: Solid Phantoms*, [Online; accessed 10. Oct. 2023], Oct. 2023. [Online]. Available: `https://www.iba-dosimetry.com/product/solid-phantoms`.

[44] *RW3 Slab Phantom | PTW*, [Online; accessed 10. Oct. 2023], Oct. 2023. [Online]. Available: `https://www.ptwdosimetry.com/en/products/rw3-slab-phantom`.

[45] A. Loureno, A. Subiel, N. Lee, *et al.*, “Absolute dosimetry for FLASH proton pencil beam scanning radiotherapy,” *Sci. Rep.*, vol. 13, no. 2054, pp. 1–11, Feb. 2023, ISSN: 2045-2322. DOI: `10.1038/s41598-023-28192-0`.

[46] C. Peucelle, C. Nauraye, A. Patriarca, *et al.*, “Proton minibeam radiation therapy: Experimental dosimetry evaluation,” *Med. Phys.*, vol. 42, no. 12, pp. 7108–7113, Dec. 2015, ISSN: 2473-4209. DOI: `10.1118/1.4935868`. eprint: `26632064`.

[47] *Density » IT’IS Foundation*, [Online; accessed 11. Oct. 2023], Oct. 2023. [Online]. Available: `https://itis.swiss/virtual-population/tissue-properties/database/density`.

[48] *Safety Footwear With Accurate Fit Protection*, [Online; accessed 2. Nov. 2023], Jul. 2023. [Online]. Available: `https://ohsonline.com/articles/2008/01/study-womens-skulls-thicker-mens-wider-might-affect-protection-design.aspx?m=1`.

[49] *Grade 4 Unalloyed Ti ("Pure") 75A (UNS 50700)*, [Online; accessed 11. Oct. 2023], Jul. 2013. [Online]. Available: `https://www.azom.com/article.aspx?ArticleID=9414`.

[50] *Imaging Considerations for Proton Therapy Treatment Planning*, [Online; accessed 11. Oct. 2023], Oct. 2021. [Online]. Available: `https://www.itnonline.com/article/imaging-considerations-proton-therapy-treatment-planning-0`.

[51] Y. Liu, Y. Lei, Y. Wang, *et al.*, "MRI-based Treatment Planning for Proton Radiotherapy: Dosimetric Validation of a Deep Learning-based Liver Synthetic CT Generation Method," *Phys. Med. Biol.*, vol. 64, no. 14, p. 145 015, Jul. 2019. DOI: `10.1088/1361-6560/ab25bc`.

[52] P. Monnin, N. Sfameni, A. Gianoli, and S. Ding, "Optimal slice thickness for object detection with longitudinal partial volume effects in computed tomography," *J. Appl. Clin. Med. Phys.*, vol. 18, no. 1, p. 251, Jan. 2017. DOI: `10.1002/acm2.12005`.

[53] *Artifacts and Partial-Volume Effects – UTCT – University of Texas*, [Online; accessed 1. Sep. 2023], Sep. 2023. [Online]. Available: `https://www.ctlab.geo.utexas.edu/about-ct/artifacts-and-partial-volume-effects`.

[54] *iMAR - Iterative Metal Artifact Reduction*, [Online; accessed 11. Oct. 2023], Oct. 2023. [Online]. Available: `https://www.siemens-healthineers.com/molecular-imaging/options-and-upgrades/software-applications/imar`.

[55] M. Rovituso, C. F. Groenendijk, E. van der Wal, *et al.*, "Characterisation of the HollandPTC R&D proton beamline for physics and radiobiology studies," *arXiv, In Prep. for Physica Medica*, Feb. 2023. DOI: `10.48550/arXiv.2302.09943`. eprint: `2302.09943`.

[56] K. M. Holm, U. Weber, Y. Simeonov, A. Krauss, O. Jkel, and S. Greilich, "2D range modulator for high-precision water calorimetry in scanned carbon-ion beams," *Phys. Med. Biol.*, vol. 65, no. 21, p. 215 003, Oct. 2020, ISSN: 0031-9155. DOI: `10.1088/1361-6560/aba6d5`.

[57] *IBA Dosimetry: Lynx PT - Daily machine parameter verification*, [Online; accessed 26. Oct. 2023], Oct. 2023. [Online]. Available: `https://www.iba-dosimetry.com/product/lynx-pt`.

[58] L. Placidi, M. Togno, D. C. Weber, A. J. Lomax, and J. Hrbacek, "Range resolution and reproducibility of a dedicated phantom for proton PBS daily quality assurance," *Z. Med. Phys.*, vol. 28, no. 4, pp. 310–317, Dec. 2018, ISSN: 0939-3889. DOI: `10.1016/j.zemedi.2018.02.001`.

[59] S. Russo, A. Mirandola, S. Molinelli, *et al.*, "Characterization of a commercial scintillation detector for 2-D dosimetry in scanned proton and carbon ion beams," *Phys. Med.*, vol. 34:48-54. Feb. 2017, ISSN: 1724-191X. DOI: `10.1016/j.ejmp.2017.01.011`. eprint: `28118950`.

[60] *OCTAVIUS Detector 1500XDR | PTW*, [Online; accessed 26. Oct. 2023], Oct. 2023. [Online]. Available: `https://www.ptwdosimetry.com/en/products/octavius-detector-1500xdr`.

[61] *Gafchromic™ Radiology, Radiotherapy and Security Radiographic Films, and FilmQA™ Pro Software*, [Online; accessed 26. Oct. 2023], Oct. 2023. [Online]. Available: `http://www.gafchromic.com`.

[62] N. Wen, S. Lu, J. Kim, *et al.*, "Precise film dosimetry for stereotactic radiosurgery and stereotactic body radiotherapy quality assurance using Gafchromic™ EBT3 films," *Radiat. Oncol.*, vol. 11, no. 1, pp. 1–11, Dec. 2016, ISSN: 1748-717X. DOI: `10.1186/s13014-016-0709-4`.

[63] P. Vaiano, M. Consales, P. Casolaro, *et al.*, "A novel method for EBT3 Gafchromic films readout at high dose levels," *Physica Med.*, vol. 61, pp. 77–84, May 2019, ISSN: 1120-1797. DOI: `10.1016/j.ejmp.2019.04.013`.

[64] T. Cheung, M. J. Butson, and P. K. N. Yu, "Post-irradiation colouration of Gafchromic EBT radiochromic film," *Phys. Med. Biol.*, vol. 50, no. 20, pp. 281–285, Oct. 2005, ISSN: 0031-9155. DOI: `10.1088/0031-9155/50/20/N04`. eprint: `16204869`.

[65] L. B. Valdetaro, E. M. Høye, P. S. Skyt, J. B. B. Petersen, P. Balling, and L. P. Muren, "Empirical quenching correction in radiochromic silicone-based three-dimensional dosimetry of spot-scanning proton therapy," *Physics and Imaging in Radiation Oncology*, vol. 18, pp. 11–18, Apr. 2021, ISSN: 2405-6316. DOI: `10.1016/j.phro.2021.03.006`.

[66] J. M. Verburg and J. Seco, “Dosimetric accuracy of proton therapy for chordoma patients with titanium implants,” *Med. Phys.*, vol. 40, no. 7, Jul. 2013. DOI: `10.1118/1.4810942`.

[67] H. Paganetti, “Range uncertainties in proton therapy and the role of Monte Carlo simulations,” *Phys. Med. Biol.*, vol. 57, no. 11, R99, Jun. 2012. DOI: `10.1088/0031-9155/57/11/R99`.

[68] J. Saini, E. Traneus, D. Maes, *et al.*, “Advanced Proton Beam Dosimetry Part I: review and performance evaluation of dose calculation algorithms,” *Translational Lung Cancer Research*, vol. 7, no. 2, p. 171, Apr. 2018. DOI: `10.21037/tlcr.2018.04.05`.

[69] F. De Martino, S. Clemente, C. Graeff, G. Palma, and L. Cella, “Dose Calculation Algorithms for External Radiation Therapy: An Overview for Practitioners,” *Appl. Sci.*, vol. 11, no. 15, p. 6806, Jul. 2021, ISSN: 2076-3417. DOI: `10.3390/app11156806`.

[70] A. Murphy, “Windowing (CT),” *Radiopaedia*, Mar. 2023. DOI: `10.53347/rID-52108`.

[71] J. Rojo-Santiago, S. J. M. Habraken, D. Lathouwers, A. Mndez Romero, Z. Perk, and M. S. Hoogeman, “Accurate assessment of a Dutch practical robustness evaluation protocol in clinical PT with pencil beam scanning for neurological tumors,” *Radiother. Oncol.*, vol. 163, pp. 121–127, Oct. 2021, ISSN: 0167-8140. DOI: `10.1016/j.radonc.2021.07.028`.

[72] H. L. van der Weide, M. C. A. Kramer, D. Scandurra, *et al.*, “Proton therapy for selected low grade glioma patients in the Netherlands,” *Radiother. Oncol.*, vol. 154, pp. 283–290, Jan. 2021, ISSN: 0167-8140. DOI: `10.1016/j.radonc.2020.11.004`.

[73] H. Lin, C. Shi, S. Huang, *et al.*, “Applications of various range shifters for proton pencil beam scanning radiotherapy,” *Radiat. Oncol.*, vol. 16, no. 1, pp. 1–10, Dec. 2021, ISSN: 1748-717X. DOI: `10.1186/s13014-021-01873-8`.

[74] J. Shen, W. Liu, A. Anand, *et al.*, “Impact of range shifter material on proton pencil beam spot,” *Med. Phys.*, vol. 42, no. 3, p. 1335, Mar. 2015. DOI: `10.1118/1.4908208`.

[75] A. Kern, C. Bumer, K. Krninger, J. Wulff, and B. Timmermann, “Impact of air gap, range shifter, and delivery technique on skin dose in proton therapy,” *Med. Phys.*, vol. 48, no. 2, pp. 831–840, Feb. 2021, ISSN: 0094-2405. DOI: `10.1002/mp.14626`.

[76] S. Rana and J. Bennouna, “Impact of Air Gap on Intensity-Modulated Proton Therapy Breast Plans,” *Journal of Medical Imaging and Radiation Sciences*, vol. 50, no. 4, pp. 499–505, Dec. 2019, ISSN: 1939-8654. DOI: `10.1016/j.jmir.2019.09.007`.

[77] J. Rojo-Santiago, E. Korevaar, Z. Perk, S. Both, S. J. M. Habraken, and M. S. Hoogeman, “PTV-based VMAT vs. robust IMPT for head-and-neck cancer: A probabilistic uncertainty analysis of clinical plan evaluation with the Dutch model-based selection,” *Radiother. Oncol.*, vol. 186, Sep. 2023, ISSN: 0167-8140. DOI: `10.1016/j.radonc.2023.109729`.

[78] D. Maes, J. Saini, J. Zeng, R. Rengan, T. Wong, and S. R. Bowen, “Advanced proton beam dosimetry part II: Monte Carlo vs. pencil beam-based planning for lung cancer,” *Translational Lung Cancer Research*, vol. 7, no. 2, p. 114, Apr. 2018. DOI: `10.21037/tlcr.2018.04.04`.

[79] D. Petrova, S. Smickovska, and E. Lazarevska, “Conformity Index and Homogeneity Index of the Postoperative Whole Breast Radiotherapy,” *Open Access Macedonian Journal of Medical Sciences*, vol. 5, no. 6, p. 736, Oct. 2017. DOI: `10.3889/oamjms.2017.161`.

[80] M. F. Chan, C.-C. Chen, C. Shi, *et al.*, “Patient-Specific QA of Spot-Scanning Proton Beams using Radiochromic Film,” *International journal of medical physics, clinical engineering and radiation oncology*, vol. 6, no. 2, p. 111, May 2017. DOI: `10.4236/ijmpcero.2017.62011`.

[81] D. A. Low, W. B. Harms, S. Mutic, and J. A. Purdy, “A technique for the quantitative evaluation of dose distributions,” *Med. Phys.*, vol. 25, no. 5, pp. 656–661, May 1998, ISSN: 0094-2405. DOI: `10.1118/1.598248`. eprint: `9608475`.

[82] H. Li, L. Dong, L. Zhang, J. N. Yang, M. T. Gillin, and X. R. Zhu, “Toward a better understanding of the gamma index: Investigation of parameters with a surface-based distance method,” *Med. Phys.*, vol. 38, no. 12, p. 6730, Dec. 2011. DOI: `10.1118/1.3659707`.

[83] J. Winiecki, T. Morga, K. Majewska, and B. Drzewiecka, “The gamma evaluation method as a routine QA procedure of IMRT,” *Reports of Practical Oncology & Radiotherapy*, vol. 14, no. 5, pp. 162–168, Sep. 2009, ISSN: 1507-1367. DOI: `10.1016/S1507-1367(10)60031-4`.

[84] M. Stock, B. Kroupa, and D. Georg, “Interpretation and evaluation of the gamma index and the gamma index angle for the verification of IMRT hybrid plans,” *Phys. Med. Biol.*, vol. 50, no. 3, pp. 399–411, Feb. 2005, ISSN: 0031-9155. DOI: `10.1088/0031-9155/50/3/001`. eprint: `15773719`.

[85] X. R. Zhu, F. Poenisch, X. Song, *et al.*, “Patient-specific quality assurance for prostate cancer patients receiving spot scanning proton therapy using single-field uniform dose,” *Int. J. Radiat. Oncol. Biol. Phys.*, vol. 81, no. 2, pp. 552–559, Oct. 2011, ISSN: 1879-355X. DOI: `10.1016/j.ijrobp.2010.11.071`. eprint: `21300457`.

[86] A. J. Lomax, T. Bhringer, A. Bolsi, *et al.*, “Treatment planning and verification of proton therapy using spot scanning: initial experiences,” *Med. Phys.*, vol. 31, no. 11, pp. 3150–3157, Nov. 2004, ISSN: 0094-2405. DOI: `10.1118/1.1779371`. eprint: `15587667`.

A

Literature Review

The Influence of Metal Implants on Proton Therapy: Addressing Uncertainties through Treatment Planning Strategies

Iris Kuitems
MSc Biomedical Engineering, Track Medical Physics
Delft University of Technology
HollandPTC

***Abstract*—The objective of this literature research is to investigate what treatment planning strategies are used for proton therapy in the presence of metal implants. In the first part, literature was evaluated in a non-systematic manner, to obtain an overview of the fundamental aspects of proton therapy. The impact of proton therapy on metal implants was examined and related uncertainties were identified.**

Hereafter, in part 2, a systematic literature search was conducted to explore the current knowledge of resolving potential challenges of proton therapy in combination with metal implants. Search queries were created to find relevant articles in databases Pubmed and Scopus. 22 articles were considered eligible and were evaluated. These articles covered a wide range of strategies, with the most significant ones including: (1) The utilization of techniques aimed at mitigating CT-related issues such as artifact reduction algorithms or density overrides. (2) The implementation of a Monte Carlo dose calculation algorithm. (3) Locally accounting for the presence of implants by using avoidance margins or beam-specific margins. (4) The adoption of appropriate optimization methods, including Single Field Optimization (SFO), Multiple Field Optimization (MFO), and robust optimization techniques.

***Index Terms*—Proton therapy, treatment planning, metal implants**

1. INTRODUCTION

1.1 Proton Therapy

Proton therapy has raised increasing interest in the field of cancer treatment in the past few decades. It is a type of external radiation therapy, in which a proton beam is aimed at the patient, causing cell death and shrinkage of the tumor [1]. Prior to starting the treatment, a treatment plan is created to determine the dose distribution in the tissue. This entails the delineation of the tumor, giving rise to the clinical target volume (CTV). The primary objective is to ensure a sufficiently high dosage is provided to the CTV, thereby effectively targeting the tumor [2]. Additionally, the treatment plan takes into account neighboring tissues and organs at risk (OARs), where the aim is to minimize the radiation dose delivered to these structures. These precautions are highly important as they mitigate potential side effects and minimize damage to healthy tissue [3].

Proton therapy offers several advantages when compared to conventional photon-based radiotherapy. In the latter approach, all cells along the trajectory of the photons are subjected to radiation, inevitably impacting neighboring tissues and OARs all the way through the patient. In contrast, protons have a limited range and deposit their energy predominantly in the last part of their path, resulting in the absence of an exit dose. This phenomenon is depicted in Figure 1. As illustrated, the proton beam creates a very high amount of energy, deposited in a very localized region known as the Bragg peak, which exhibits a characteristic, sharp dose gradient [4]. Consequently, the dose deposition can be steered precisely, thereby facilitating the prescribed delivery of radiation to the tumor, while sparing the OARs.

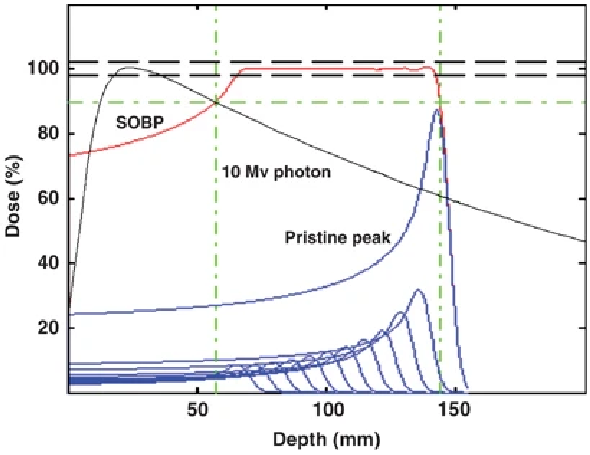

Fig. 1: In this graph, the dose distribution of photons (depicted in black) and protons (depicted in blue) is presented. The y-axis represents the dose distribution and the x-axis is the depth in tissue. The dose delivery curve of photons exhibits a broad distribution, with a peak located at approximately ±30 mm depth in tissue. In contrast, protons display a more narrow dose delivery curve, characterized by a peak situated deeper in the tissue at approximately ±150 mm depth [1].

Proton therapy is already frequently applied for treating cancer and has demonstrated efficacy, particularly in the treatment of non-metastatic cancers and tumors situated close to critical organs such as the brain and spinal cord. Additionally, it is especially beneficial for treating pediatric patients, because it

Fig. 2: In this figure, the Synthes Flapfix system is visible (DePuySynthes). These clips are used for fixation after craniotomy. Here, the skull is fixated with 3 different titanium clips [9].

reduces the risk of detrimental effects on healthy, growing tissue. The application of proton therapy involves various cancer types, including cancer of the eye, head and neck, breast, lung, liver, prostate, and sarcomas within the central nervous system, pelvic region or brain [4].

Nevertheless, while proton therapy seems to be more advantageous in comparison with photon therapy, it also presents a significant challenge. This arises from the steep dose gradient at the far end of the Bragg peak. Small inaccuracies in the determination of the proton range, can significantly affect treatment delivery. This uncertainty is the primary aspect that prevents proton therapy from optimal sparing the OARs [5].

1.2 Implants

This literature research is written as a preparation for a Master Thesis that investigates the effect of proton therapy on cranial fixation clips. Patients with brain tumors often undergo surgery, which involves the creation of a small aperture in the skull, known as a craniotomy, to access the brain tissue [6]. Following this procedure, the skull needs to be repositioned and reattached again, by using a fixation device composed of metal [7], [8]. Figure 2 showcases the Synthes Flapfix fixation system, an example of clips used for post-craniotomy fixation.

The effects of metal implants on proton therapy have been an object of research in the past two decades. Recent findings suggest that the presence of titanium implants within the body can give rise to artifacts or distortions, resulting in inaccuracies in the treatment plan [10], [11]. The artifacts appear mainly in the vicinity of the implants, causing inaccuracies in determining their size and geometry. Consequently, these discrepancies introduce clinical uncertainties and errors in the delineation of the CTV and OARs [10], [12]. This results in either an underdosage of the CTV and possible treatment failure, or an overdosage of the OAR, leading to unnecessary side effects.

This indicates a need to understand the effects of metal implants on proton therapy. To assess the present status of proton therapy when used in combination with metal implants, this literature research encompasses not only cranial fixation clips but also other types of metal implants.

1.3 Structure of this literature research

In the first part of this research, relevant articles were collected in a non-systematic manner, to obtain a broad understanding of the subject. The characteristics of proton therapy were explored, while also taking into account the potential impact of metal implants on treatment planning and delivery. The findings from this investigation are presented in Part 1.

In the second part of this research, a systematic literature search was conducted. To ensure a thorough examination of the existing literature, search queries were developed, inclusion and exclusion criteria were defined, and thereafter articles were screened for relevance. The outcomes of this systematic search are outlined in Part 2.

Combining the non-systematic and systematic approach delivers a well-rounded literature research that includes both the broader context of proton therapy as well as the details relevant to the treatment planning strategies. This research will therefore serve as a basis to guide the thesis.

PART 1

2. BACKGROUND INFORMATION

This section presents an overview of the fundamental aspects of proton therapy. This includes an exploration of the underlying physics principles, treatment delivery procedures, dose calculation methods, treatment planning strategies, uncertainties associated with proton therapy, and combining of proton therapy with implants.

2.1 Proton physics

To comprehend the basis of proton therapy in cancer treatment, it is important to delve into the underlying physics principles. One crucial aspect to analyze is the interaction of charged particles with materials, particularly their stopping power (SP). The following equation can describe this:

$$\frac{S}{\rho} = \frac{-dE}{\rho dx}[13] \tag{1}$$

Here, S represents the stopping power (SP) of a particle in a medium, ρ the density of the medium it travels through, dE the energy loss and dx the travel distance.

Equation 1 demonstrates that the SP is characterized by the energy loss, dE, per unit of length, dx. As mentioned in the introduction, the trajectory of a proton is indicated by the Bragg peak. This describes the depth within the tissue where protons deposit their maximum amount of energy. When a mono-energetic proton beam is used, this peak is referred to as the pristine Bragg Peak, visible in Figure 1. However, when irradiating a larger volume, such as a tumor, a more widespread Bragg Peak is desired, covering the entire tumor. This is achieved by modulating the energies, creating a Spread Out Bragg Peak (SOBP), see Figure 1. This indicates that the depth of the Bragg peak is dependent on the energy of the proton beam [14].

Furthermore, the penetration depth of the beam is also influenced by the density, ρ, of the material it travels through. This can be observed in Figure 3, where the left part represents the propagation of a proton beam through water, the middle part through titanium (lower density), and the right part through steel (higher density). Evidently from the image, protons deposit their energy earlier in the medium, when passing through higher-density media.

Another important aspect to consider is the interaction mechanisms between protons and the atoms of the medium. The stopping power of a proton in a medium is influenced by different interaction mechanisms, but the most important interaction mechanism is Coulomb scattering. This is the deflection that occurs when protons interact with the electric fields of other charged particles that are encountered when traversing a medium. It occurs due to the repulsive or attractive forces between the charges involved [13].

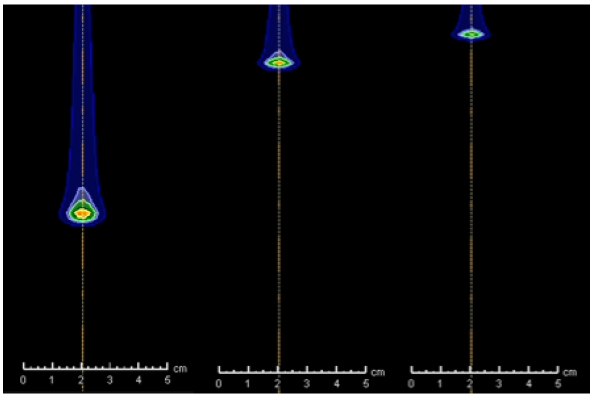

Fig. 3: The propagation of a mono-energetic proton beam in three different media: on the left water, in the middle titanium, and on the right steel. The energy remains the same across all three scenarios. Source: HollandPTC

2.2 Proton therapy treatment workflow

This section presents a concise overview of the proton therapy workflow. The process begins with the patient's diagnosis, after which the appropriate treatment is determined. Possible treatment options include surgery, radiation therapy, chemotherapy, immunotherapy, targeted therapy, or a combination thereof [15]. In the Netherlands, in cases where radiotherapy is considered suitable, an evaluation is conducted to verify whether photon therapy or proton therapy is the optimal option. In HollandPTC, the center where this research is conducted, a treatment plan for both modalities will be created and compared to determine the most suitable approach. Once a decision is made, the treatment plan is further optimized and adjusted, after which the treatment delivery can start.

In the following sections, the most important stages in this workflow are explained, commencing with the treatment delivery. Here, the main focus lies on the treatment planning stage, because this is the primary emphasis of the thesis. This encompasses aspects such as target delineation, dose calculation methodologies, and plan optimization techniques. Additionally, key aspects of metal implants in proton therapy are enlightened.

2.3 Treatment delivery

There are two primary modalities that are used for the delivery of proton therapy: passively scattered (PSPT) proton therapy or pencil beam scanning (PBS) proton therapy. The distinctions between these two techniques are explained in a study by Beddok et al. [16]:

- Passively scattering: "Accurately modulating the energy of the initially narrow mono-energetic beam with a range modulation wheel and scattering it laterally to cover the tumor volume."
- Pencil beam scanning: "Scanning narrow (pencil) beams magnetically by energy layers."
  PBS can be used with single or multiple fields, which will also be referred to as single field uniform dose

(SFUD) and intensity modulated proton therapy (IMPT) respectively.

Both techniques are employed in clinical practice. However, PBS has some advantages over PSPT. PBS uses a scanning technique, in which the location, intensity, and energy of multiple proton spots can be adjusted separately. This enables high precision in dose distribution and creates adequate target coverage. This is not possible with PSPT, in which a range-modulating device is required to shape the proton beam [17]. This research focuses therefore only on PBS proton therapy.

2.4 Treatment planning: delineation

As described in the introduction, prior to the treatment, a treatment plan is made. Among other imaging modalities, this is mostly done by making a Computed Tomography (CT) scan of the patient [18]. This scan is used for the delineation of the tumor and critical organs. Some concepts are introduced to improve treatment outcomes and ensure complete tumor coverage by incorporating uncertainties [19]:

- Gross Tumor Volume (GTV): This is the visible tumor mass, also called the macroscopic tumor volume.
- Clinical Target Volume (CTV): This includes also the invisible microscopic enlargements of the tumor in the neighboring tissues.
- Internal Target Volume (ITV): This includes the uncertainties created by the motion of the body during treatment.
- Planning Target Volume (PTV): This is the volume that is used for treatment planning, and takes several types of uncertainties into account.

2.5 Treatment planning: dose calculation

An important aspect of the treatment planning process is dose calculation. This happens after the delineation process and is performed to determine the distribution of radiation within the patient's body. The precision of a dose calculation algorithm depends on several factors [20]:

- The data that is used to perform the calculation and the capability of the system to comprehend this data.
- The assumptions that the algorithm makes regarding physical mechanisms in the body.
- The tissue heterogeneities in the area where the dose is calculated.

Several dose calculation methods exist, with analytical pencil beam algorithms and Monte Carlo (MC) algorithms being the most prevalent [21].

Analytical pencil beam algorithms

Analytical pencil beam algorithms can be used to calculate the dose distribution in PBS proton therapy. Here, the proton beam that is targeting one spot is divided into smaller beamlets, called pencil beams.

This algorithm uses models to calculate the dose deposition along the path of each of these pencil beams [20]. The patient's body is simplified in these models: it involves setting up an arrangement of uniform slabs that extend sideways, at each depth of the beamlet. The material composition of each slab is defined according to the material composition at the central axis of the beam. Pencil beam algorithms encounter difficulties when addressing different tissue densities; if the calculation of each beam is limited to the material at the central axis of the beam path, variations in tissue densities in the surrounding area will not be accurately accounted for.

Additionally, pencil beam algorithms typically are insufficient in modeling the secondary electron distribution created by the protons traversing a heterogeneous medium [20], [21].

This results in inaccuracies regarding dose calculations. Several approaches have been made to address this issue. However, they have not been optimally successful as they lead to increased computational time and persistent incorrect consideration of small heterogeneities [21].

Monte Carlo algorithms

MC algorithms have been demonstrated to provide enhanced precision when compared to pencil beam algorithms. An MC algorithm is based on a stochastic representation of the interactions between protons, secondary particles, and tissue. It tracks particles that traverse different types of tissues and it models each interaction based on probability distributions. The particles are tracked until they reach a certain energy threshold: at that point, it is assumed that the dose is deposited [20], [22].

One advantage of MC algorithms is that they also include the generation of secondary particles as a result of the interactions [22]. Next to that, MC algorithms can account for tissue inhomogeneities and are therefore better capable of handling complicated geometries. As a result, they exhibit better accuracy when metal implants are present, because of the improved precision in addressing the sharp density interfaces around the implants [23]. This makes MC algorithms a suitable technique for treating patients with metal implants [24]. Nevertheless, these advantages go at the expense of significantly increased computational demands [21].

Due to the established benefits, MC algorithms have already been adopted by large commercial treatment planning systems. Consequently, it is already often used in clinical treatment planning systems [24].

2.6 Uncertainties

There are several types of uncertainties that can create difficulties in correctly planning and delivering the dose. To provide a clear overview of the most important types of uncertainties, a subdivision has been established: technical, biological, delineation, and anatomical uncertainties.

Technical uncertainties

- Setup uncertainties: In proton therapy, the total dose is administered in several fractions, spread out over several

days to weeks. The treatment plan is based on the initial patient's position. The efficacy of the treatment relies on the accurate replication of the patient's position, throughout all the fractions. Thus, ensuring accurate treatment delivery relies on proper patient positioning. Consequently, this creates the potential for errors and uncertainties. These uncertainties can arise from either displacement of the patient or the treatment delivery system [25].
- Range uncertainties: This type of uncertainty includes the potential alterations in the penetration depth of protons in tissue. Tryggestad et al. [25] presented two main causes of range uncertainties in proton treatment. Firstly, treatment planning is performed on CT scans. These scans are based on Hounsfield Units (HU), which are subsequently based on the linear attenuation coefficient of different materials. However, the relationship between HU and proton relative stopping power is non-linear, which results in potential errors in the range verification. Moreover, the range of protons differs in different types of materials, as was explained in Figure 3. This causes difficulties in predicting the range of the protons.
- Dose calculation algorithms: As was described in section 2.5, dose calculation algorithms introduce uncertainties in the dose delivery as well.

Biological uncertainties

- Relative Biological Effectiveness (RBE): The dose deposition in tissue varies for different types of radiation. The RBE is introduced to compare the effect of these different types of radiation, in terms of damage to the irradiated tissue. It is incorporated into the treatment plan to control tissue damage. Treatment plans are created with an assumed RBE for protons, namely 1.1. However, the RBE is dependent on several factors, which makes this assumption a source of uncertainties [16].

Delineation uncertainties

- Contouring uncertainties: Treatment planning is based on the precise delineation of the tumor and anatomical structures, as described in section 2.4. The accuracy of the delineation is, among other factors, dependent upon the accuracy of the imaging modality. Microscopic structures are not visible on currently used imaging modalities, which results in potential errors in contouring [26].
- Inter-observer variability: The delineation is performed by medical specialists. Variations among different observers in their interpretation of anatomical structures and the delineation process can introduce systematic inaccuracies in treatment delivery [27].

Anatomical uncertainties

- Intra-fractional anatomical differences: As was previously mentioned, proton therapy is delivered in multiple fractions, spread out over several weeks. Often, anatomical changes arise due to for example shrinkage of the tumor or weight loss. The dose distributions will alter which can lead to under- or overdosing in certain areas [28].
- Tumor movement: During the treatment delivery, movement of the tumor can occur due to for example breathing, heartbeat, or gastrointestinal motions. The dynamic motion of the tumor necessitates adjusted treatment planning techniques to prevent dosimetric inaccuracies [25].

Uncertainties due to the presence of metal implants

- Imaging artifacts: Metal implants can create artifacts in CT images. This results in a possible misinterpretation in assigning the accurate HU in those pixels. This makes accurate delineation of implants a difficult task. Consequently, these uncertainties create errors in the treatment plan [29].
- Dose calculation: Treatment planning systems use conversion tables to convert the HU's from the CT image to the mass density of the materials. These tables are generally made based on tissue-equivalent materials. The presence of high-density materials used in implants creates difficulties because there are uncertainties in assigning the correct material of the implant in the calculation [29], [30].

2.7 Correcting for uncertainties

The uncertainties described in the previous section can lead to discrepancies between the dose delivered to the patient, compared to the dose calculated during treatment planning. Accordingly, the accurate management of these uncertainties is important to ensure optimal coverage of the CTV and minimize irradiation of the OARs. Therefore, it is crucial to use methods for addressing and correcting these uncertainties.

Adding geometrical margins

In section 2.4, the concept of adding margins around the target volume (CTV), e.g. creating a PTV, was introduced. For photon therapy, this is supposed to be an acceptable method to correct setup and anatomical uncertainties. To support this, studies have proved that slight displacements of the target only have a small effect on the photon dose distribution. Therefore adding margins to the CTV, creating a PTV, is considered sufficient in most cases [31], [32].

However, the uncertainties present in proton therapy differ from the ones that occur in photon therapy, therefore making this approach unsuitable [33], [34]. This is mostly caused by the alteration in proton dose distribution that occurs when the tissue along the beam path is changed. This is especially a problem with heterogeneous tissues, air cavities, or implants [31].

Field optimization

Another approach to reducing uncertainties is by optimization methods. In general, there are two ways to optimize PBS proton therapy: single-field optimization (SFO) and multi-field optimization (MFO). Beddok et al. explained these concepts as follows [16]:

- SFO: “Each beam is optimized independently to achieve a uniform dose to the target while minimizing the dose outside the tumor.”
- MFO: “The optimization process simultaneously optimizes the intensities of the spots from all of the beams, thereby irradiating the tumor heterogeneously with each beam but providing a uniform dose to it.” This is mostly used in intensity-modulated proton therapy (IMPT).

When using MFO, all the spots are optimized simultaneously, leading to an inhomogeneous dose distribution with large dose gradients, both within and outside the irradiation field margins. By combining the individual fields, uniform coverage of the target area is then achieved. This concept is accompanied by a significant downside; the large dose gradients increase its susceptibility to uncertainties [35], [36].

SFO is better at addressing uncertainties. This is because it optimizes the single fields separately, making the dose gradients generally lower. However, because of the reduced amount of modulations that can be created by SFO, it is less capable of sparing critical organs than MFO [35], [36]. This creates the necessity to investigate other optimization methods that are robust against uncertainties.

Robust optimization

Relatively novel methods that are used for optimizing the treatment plan are robust optimization techniques. Here, the optimization is directly performed on the CTV, without the usage of a PTV. It incorporates setup and range errors during the spot weight optimization itself. This results in less dosage to neighboring organs at risk. One approach to applying robust optimization is Minimax optimization. This method operates by finding the optimal treatment plan by minimizing the worst-case scenario plan. It thereby aims to be robust against large uncertainties [37].

2.9 Implants

As was previously mentioned, this research will focus on proton therapy in combination with metal implants. To gain a deeper comprehension, this section will elaborate on some general characteristics of metals used for medical implants.

The atomic number (Z) of metal implants is an important property in radiation therapy. It presents the number of protons in the atomic nuclei. When protons traverse tissues with higher atomic numbers, more interactions take place, which results in more scattering, when compared to tissues with lower atomic numbers. Therefore, high-Z materials generally lead to larger uncertainties than low-Z materials and have a large impact on the robustness of the treatment plan [38].

Table I gives an overview of the atomic numbers of some of the materials used in medical implants that are discussed in the reviewed literature [39]. As is depicted in the table, the atomic numbers of the different materials differ a lot. It is important to consider this when evaluating the effect of proton therapy on metal implants.

TABLE I: Several atomic numbers of metals that are used for medical implants.

Material	Atomic number (Z)
Titanium	22
Stainless steel	24
Copper	29
Tantalum	73
Lead	82

In addition to the presented metal implants, several studies have also investigated the effect of using Carbon Fiber Reinforced Polyetheretherketone (CFR-PEEK) implants, which are low-density materials that can be applied in medical implants. Poel et al. [38] compared the usage of titanium and CFR-PEEK implants for proton therapy. It was found that apart from less occurrence of artifacts, utilizing CFR-PEEK in proton therapy does not significantly influence the dose distribution in a treatment plan, when compared to the situation without artificial materials.

2.11 Research objective

Patients with metal implants in their bodies, present a challenge in the treatment planning process of proton therapy. The presence of these metal implants can cause significant dosimetric uncertainties and affect the accuracy of the dose distribution. The focus of this research lies in the usage of metal cranial fixation clips, which was elaborated on in section 1.2.

The objective of the rest of this literature research is to explore the different treatment planning strategies for patients undergoing proton therapy with metal implants. It aims to analyze the currently known strategie and to assess to what extent it is possible to correct for negative effects caused by these implants. The aim is to come to an answer for the following research question: “What planning strategies are used for proton therapy in the presence of metal implants?”

PART 2

In the second part of this research, a systematic literature search was conducted. Section 3 ‘Methods’ describes the approach of finding the relevant literature. Section 4 ‘Results’ presents the observed findings from the analyzed literature. Subsequently, a short discussion and conclusion will follow in Section 5 ‘Discussion and Conclusion’.

3. METHODS

3.1 Selection of Articles

Data for this review were gathered via the electronic databases Pubmed and Scopus. The focus is to find an overview of the literature, reporting on proton therapy planning strategies in combination with metal implants. A search query was built, in which a combination of Medical Subject Headings (Mesh) terms and keywords were used:

Search query Pubmed: `("Proton Therapy"[Mesh] OR "proton therap*"[tw] OR "proton beam therap*"[tw] OR "proton beam radiation therap*"[tw] OR "proton radiation therapy*"[tw] OR "proton beam"[tw] OR "particle therapy*"[tw]) AND ("Titanium"[Mesh] OR titanium[tw] OR "Metals"[Mesh] OR metal*[tiab]) AND ("Prostheses and Implants"[Mesh] OR "implant*")`

Search query Scopus: `("proton therap*" OR "proton radiotherap*" OR \proton radiation therapy*" OR (proton AND (therap* OR radiotherap* OR \radiation therapy*")) OR "proton beam" OR "particle therap*") AND (titanium OR metal*) AND (implant*)`

In the query, particle therapy was used, which includes protons, neutrons, and other heavy ions. This review only focuses on protons, but the term must be included to avoid missing essential articles.

Additionally, regarding the materials of the implants, only “titanium” and “metals” were added to the search query. This is because the focus of this review lies on the titanium cranial fixation clips. By adding “metals” to the query, other relevant articles reporting about non-titanium metal implants were examined as well.

Terms related to robust optimization methods were not included, because the addition of the term “robust optimization” reduced the number of articles significantly. An explanation for this could be that robust optimization for proton therapy is relatively new [40], which explains why little research has been done on this concept.

Based on exclusion criteria presented in Table II, articles were included or excluded in this review. First, all the articles were scanned, only on title and abstract. Hereafter, the articles were read entirely.

TABLE II: Exclusion criteria categorized by accessibility, title and abstract, and full article

	Criteria	Explanation
Accessibility	Language	Not English
	Accessibility	No access by TU Delft
Title and abstract	Reported content	Not about proton therapy
		Not about biomaterials
		Systematic reviews
Full article	Reported outcomes	CT artifact reduction algorithms
		Fiducial markers
		Material size too small (nanoparticles)
		No treatment planning strategies

4. RESULTS

This section presents an overview of the results of the literature search. First, the outcomes of the applied search methods are presented. Subsequently, there will be emphasis on the metal implants that are studied and their most important characteristics. Furthermore, the effects of the interaction between the proton beam and the metal implants, are outlined. Lastly, the different strategies to manage metal implants are presented. The strategies are categorized into themes: avoidance, treatment delivery, treatment planning, field optimization, and CT imaging.

In the included articles, a range of different research approaches and methodologies were utilized. Consequently, a large diversity in outcome measures was observed. For instance, some studies utilized gamma analysis, while others solely compared doses in percentages. Therefore, it was chosen not to review different strategies based on one outcome measure quantitatively, but to qualitatively analyze the included articles.

4.1 Search results

The search was conducted in April 2023. In the flowchart in Figure 4, an overview of the inclusion process is presented. 311 articles were extracted from the databases. First, duplicates were removed, which led to a reduction of 62 articles. Only English-written articles and articles accessible by TU Delft were evaluated. This led to the exclusion of another 14 articles.

Screening on title and abstract resulted in the exclusion of 161 articles. Both human and phantom studies were considered eligible for this review. Articles were excluded if they did not report about proton therapy or metal implants at all. The publication date was not considered an exclusion criterion due to the relatively recent emergence of proton therapy as a treatment modality, particularly in combination with metal implants. While the first article extracted from the database was published in 1975, approximately 90% of the articles were

Fig. 4: Flowchart with an overview of included articles.

published in the past two decades. There was no exclusion made based on atomic number (Z).

Lastly, references of the included articles were screened to determine eligibility. This resulted in another addition of 4 articles.

A total of 22 articles were considered eligible for this study. An overview of the included articles is presented in Table III.

4.3 Type of implants and materials

The included articles reported on different types of metal implants composed of different materials. Most articles defined the exact composition of the metal implant they investigated. On the other hand, some articles only referred to the used materials as either high-Z or low-Z materials.

Table III provides an overview of the type of implants and their materials. The different types of implants and their purpose are shortly discussed:

- Breast tissue expanders:
  Tissue expanders are implemented to provide a reconstruction of the breast after mastectomy. It is similar to a balloon that is gradually filled over several weeks, stretching the skin and muscle tissue. The expanders consist of a silicone balloon, filled with a saline solution. A metal port is also included through which the saline can be injected. This metal port can cause dose perturbations during irradiation with proton therapy [41], [42], [43], [44], [45], [46].
- Surgical stabilizing system:
  Patients treated for chordoma or chondrosarcoma (tumors in the spine) often undergo surgery prior to external radiation therapy. During a surgical procedure, the spine is fixated using surgical fixation screws, to prevent instability. Most articles reported on stabilization devices composed of titanium [10], [37], [47], [48], [49], [50], [51], [52], [53]. Two articles compared stabilization devices composed of titanium or CFR-PEEK [38], [51].
- Dental implants:
  Dental implants are commonly used to replace teeth or parts of broken teeth and are often made of metals. The presence of these implants can cause difficulties for external radiation therapy when cancer is located in the head and neck area [49], [54], [55].
- Hip prosthesis:
  Hip joint replacement is frequently applied in elderly patients. Hip prostheses are large metallic implants and their presence can influence proton therapy used to treat tumors located in the pelvic region: the prostate, uterus, and ovaries [56].
- Other implants:
  Fellin et al. [30] reported on small high-Z implants in general for their ex vivo experiments and they tested their methods on a patient with a platinum embolization coil. Additionally, Farace et al. [57] conducted ex vivo experiments on a simple phantom containing titanium inserts and Newhauser et al. [58] conducted experiments on spheres composed of stainless steel.

4.4 Effects of metal implants on proton therapy

The articles included in this review reported on several perturbations caused by the interaction of the proton beam with metal implants. This section elaborates on the most important effects.

CT Artifacts

The occurrence of artifacts created by metal implants and its accompanying uncertainties have been discussed in Section: 2.6 ‘Uncertainties’. The main causes of CT artifacts by metal implants are:

- Partial volume effect: An imaging system’s accuracy depends on its resolution. The resolution is a measure of the smallest features that can be distinguished on an image. When the size of a structure being imaged, is smaller than the size of one pixel, the system cannot distinguish the different structures anymore. This can lead to a misestimate of the exact size and contour of the implant [10] [43], [45], [56].
- Beam hardening: The X-rays produced by the CT-imaging system contain a range of energies. When the X-ray beam enters the body, the X-rays are attenuated in the tissues it traverses through. This attenuation gives rise to the beam hardening effect: low-energy X-rays are absorbed to a greater extent than high-energy X-rays. This effect is enhanced in the presence of metal implants

TABLE III: An overview of the articles included in this review and their main characteristics: the authors, year of publishing, article name, type of implant discussed in the article, and its composition.

Author	**Year**	**Article**	Type of implant	Material
DeCesaris et al.	2021	Outcomes of and treatment planning considerations for a hybrid technique delivering proton pencil-beam scanning radiation to women with metal-containing tissue expanders undergoing post-mastectomy radiation	Breast tissue expander	High Z materials
Dietlicher et al.	2014	The effect of surgical titanium rods on proton therapy delivered for cervical bone tumors: experimental validation using an anthropomorphic phantom	Surgical stabilizing implants in the spine	Titanium
Farace et al.	2015	Single-energy intensity modulated proton therapy	Inserts	Titanium
Fellin et al.	2020	An avoidance method to minimize dose perturbation effects in proton pencil beam scanning treatment of patients with small high-Z implants	Small high-Z implants	Copper, Tantalum, Lead and Platinum
Fredriksson et al.	2011	Minimax optimization for handling range and setup uncertainties in proton therapy	Surgical stabilizing implants in the spine	Titanium
Hu et al.	2023	The effect of common dental fixtures on treatment planning and delivery for head and neck intensity modulated proton therapy	Dental implants	Amalgam and porcelain-fused-to-metal crown
Kang et al.	2021	Technical Note: Clinical modeling and validation of breast tissue expander metal ports in a commercial treatment planning system for proton therapy	Breast tissue expander	Samarium cobalt, titanium and stainless steel
Kisielewicz et al.	2022	Safe Proton Radiotherapy for Patients with metal Spine Stabilization System	Surgical stabilizing implants in the spine	Titanium
Kirk et al.	2017	Field-Specific Intensity-modulated Proton Therapy Optimization Technique for Breast Cancer Patients with Tissue Expanders Containing Metal Ports	Breast tissue expander	Non-specified
Mutter et al.	2017	Initial clinical experience of postmastectomy intensity modulated proton therapy in patients with breast expanders with metal ports	Breast tissue expander	High density material. Titanium casting
Newhauser et al.	2013	Benchmark measurements and simulations of dose perturbations due to metal spheres in proton beams	Mettalic spheres	Stainless steel
Oancea et al.	2017	Effect of titanium dental implants on proton therapy delivered for head tumors: Experimental validation using an anthropomorphic head phantom	Dental implants	Titanium
Paganetti et al.	2007	Comparison of pencil-beam and Monte Carlo calculated dose distributions for proton therapy of skull-base and para-spinal tumors	Spinal and dental implants	Titanium
Pflugfelder et al.	2008	Worst case optimization: a method to account for uncertainties in the optimization of intensity modulated proton therapy	Surgical stabilizing implants in the spine	Non-specified
Poel et al.	2020	Assessing the advantages of CFR-PEEK over titanium spinal stabilization implants in proton therapy—a phantom study	Spinal implant	Titanium and CFR-PEEK
Rana et al.	2014	Dosimetric study of uniform scanning proton therapy planning for prostate cancer patients with a metal hip prosthesis, and comparison with volumetric-modulated arc therapy	Hip prosthesis	Metal (High Z materials)
Righetto et al.	2020	Accurate proton treatment planning for pencil beam crossing titanium fixation implants	Surgical stabilizing implants in the spine	Titanium
Shi et al.	2022	Comprehensive Evaluation of Carbon-Fiber-Reinforced Polyetheretherketone (CFR-PEEK) Spinal Hardware for Proton and Photon Planning	Spinal implant	Titanium and CFR-PEEK
Tourovsky et al.	2005	Monte Carlo dose calculations for spot scanned proton therapy	Surgical stabilizing implants in the spine	Titanium
Unkelbach et al.	2008	Reducing the sensitivity of IMPT treatment plans to setup errors and range uncertainties via probabilistic treatment planning	Surgical stabilizing implants in the spine	Non-specified
Zhao et al.	2020	Dose perturbation caused by metal port in breast tissue expander in proton beam therapy	Breast tissue expander	Stainless steel
Zhu et al.	2021	Intensity Modulated Proton Therapy Treatment Planning for Postmastectomy Patients with metal Port Tissue Expanders	Breast tissue expander	Steel

and causes uncertainties because low-energy X-rays are crucial for visualizing soft tissues [48].

- Intensity saturation: When imaging high-density materials, such as metal implants, the Hounsfield Units (HU's) can exceed the maximum HU scale of the CT imaging system, causing intensity saturation. This is the phenomenon when the CT imaging system is not able to accurately measure and represent high attenuation values, resulting in saturation of the pixel intensities [10], [30], [38], [54].

Dose shadows

When a proton beam passes through a high-density material, it experiences scattering and nuclear interactions that cause it to lose energy and change direction. As a result, less dose is deposited in the tissue beyond the implant resulting in a lower dose delivered to those regions [38], [43], [45], [48], [50], [51], [54]. This phenomenon is referred to as dose shadows. The main problem in proton therapy planning is that treatment planning systems do not accurately calculate these dose shadows, resulting in hot or cold spots (areas with a higher or lower dose than intended). The usage of Monte Carlo algorithms can reduce this problem. This will be discussed further in Section 4.5.3.

Dose enhancement

Zhao et al. [45] investigated dose perturbations for metal-tissue interfaces in proton therapy. They conducted experiments including the metal components of breast tissue expanders. Irradiation of the expanders resulted in a dose elevation of up to 15% at the metal-tissue interface and an additional increase at the lateral sides of the implant. Similar findings were presented by Dietlicher et al. [47] and Newhauser et al. [58]. These results indicate the need to further investigate the presence of dose elevations around metal implants when they lie in the irradiation field.

The primary cause of the dose enhancement is secondary electrons. These are created by interactions between the proton beam and the traversed tissues. The most critical interaction mechanism is Coulomb Scattering, as was discussed in Section: 2.1 'Proton physics'. This mechanism is enhanced by the presence of metal implants. While scattering itself is not primarily the issue, the challenge lies in accurately calculating and predicting its effects using dose calculation algorithms [45], [58]. This issue will be further addressed in Section 4.5.3. 'Dose calculation'.

The impact of the implants position

Oancea et al. [55] conducted research to investigate dose perturbations induced by titanium dental implants. In their experiments, titanium implants were placed at two locations: first, at the center of the Bragg peak, and second, at the beginning of the Bragg curve.

For their first setup, a more rapid dose fall-off was measured in the area distal to the implants, in comparison to the calculation of the treatment planning system (TPS). In the second setup, they also detected a noticeable difference, although the TPS's prediction was slightly more accurate. To quantify the difference between the measured and calculated dose, a gamma analysis (3 mm, 3%) was performed. The results showed 84.3% for the first setup and 86.4% for the second setup. These results indicate that the relative position of the implant with respect to the Bragg peak of the proton beam, can play a role in the accuracy of the TPS calculations.

In this research, film dosimetry measurements were used to measure the dose. This is assumed to be an adequate way to measure the dose distribution in proton therapy [59]. However, it does have limitations. Grilj et al. [60] conducted research on the Linear Energy Transfer (LET) dependent response in film dosimetry. It was reported that irradiating radiochromic films with protons can result in an under-response when compared to irradiation by photons. This is primarily caused by the amplification of the LET, especially around the Bragg Peak. The LET defines the amount of energy that is transferred from the ionizing radiation to the material it traverses. In the region around the Bragg Peak, the LET is high, because the ions decelerate rapidly. It was found that high LET radiation does not always create a response in the films, which results in an under-response.

To overcome this limitation, in the article of Oancea et al. [55], additional measurements were performed, using nuclear track detectors. They detected a high amount of both primary and secondary particles in the region behind the Bragg peak, containing high LET. They stated that this was caused by the presence of the implants and that this subsequently can result in a REB above accepted limits.

4.5 Strategies to manage metal implants

All the included articles reported ways to account for the uncertainties introduced by metal implants. The articles focused on strategies regarding CT imaging, density overrides, dose calculation algorithms, treatment planning techniques, field optimization, robust optimization, and treatment delivery techniques. The following sections will elaborate on these subjects.

4.5.1 CT imaging

This section encompasses multiple strategies, centered on CT imaging. It starts with a paragraph on metal-induced CT artifacts and the usage of CT artifact reduction algorithms to manage them. It should be noted that this review primarily focuses on strategies beyond CT artifact reduction algorithms. Therefore, articles solely dedicated to such algorithms were excluded, as indicated in Table II. However, since a significant proportion of the included articles used artifact reduction algorithms as an addition to another proposed strategy, a brief overview of their applications is provided. After that, an analysis of the correct CT acquisition protocol is presented, the difference between kilo-Voltage CT and Mega-Voltage CT systems is enlightened and lastly, the process of converting

CT-related Hounsfield Units (HU's) to relative stopping power (RSP) is addressed.

Metal induced CT artifacts

Eight of the included articles reported on using an artifact reduction algorithm to correct for CT artifacts [10], [30], [38], [45], [46], [47], [48], [51], [54].

In the study by Righetto et al. [10], the advantages of two artifact reduction algorithms were outlined for titanium fixation screws in both a phantom and clinical case: a standard and O-MAR (orthopedic metal artifact reduction) algorithm. The usage of an artifact reduction algorithm enabled an improved reconstruction of the implant's shape and dimensions. More reliable treatment plans were obtained when the O-MAR algorithm was applied. They stated that the perturbations caused by metal implants depend on implant material, orientation, and size, which should therefore be considered.

In complement to this, Poel et al. [38] investigated another method to manage metal-induced artifacts, by studying both titanium and CFR-PEEK implants. They corrected artifacts by first delineating the artifacts and then using density overrides. Their results showed that when using a non-corrected image, the presence of titanium implants showed a significant decrease in target coverage compared to an artifact-corrected CT image: a reduction from approximately 91% to 89% on the 95% coverage level was found. When using a CFR-PEEK implant, there was no reduction reported. This is due to a higher amount of distortions created by metal implants when compared to CFR-PEEK implants.

Although this method seemed efficient in eliminating artifacts, the presence of titanium implants still resulted in a significant worsening of the gamma analysis (3 mm, 3%) when comparing the TPS dose calculation with the dose measurements: a passing rate reduction from 83.2% (no implant present) to 81.3% (implant present) was calculated when using a clinical 3-field proton plan. Further detail about density overrides is provided in Section 4.5.3 'Density overrides'.

CT acquisition protocol

Fellin et al. [30] enlightened that the shape and size of an implant can greatly influence the accuracy of the TPS. Their goal was to find an adequate CT acquisition protocol, that could accurately determine the implant's size. Their experiments were conducted on small implants made of lead. Their approach was to compare a 12-bit versus a 16-bit protocol. The number of bits in an image represents the number of grey tones that one pixel can have: a 16-bit image can depict 2^{16} = 65.536 gray tones, whereas a 12-bit can depict only 2^{12} = 4.096 gray tones. They hypothesized that using an extended 16-bit acquisition protocol would result in removing data truncation, which occurs when using a 12-bit protocol. The data truncation especially affects the reconstruction of materials with high densities.

The results of the conducted experiments showed that the 16-bit protocol created a more accurate estimation of the dimensions of the metal implants: when measuring the volume of the implants, almost no errors were found in the smaller spheres (0.01-0.29 cm^3), and only a 5% error was found for the larger sphere (2.77 cm^3).

kVCT versus MVCT

Zhao et al. [45] investigated dose disruption caused by breast tissue expanders and compared the artifacts on kilo-Voltage (kV) and Mega-Voltage (MV) CT imaging. kVCT images are made by the usage of X-ray beams in the range of ± 80 – 140 kV, whereas MVCT images are made with higher energy X-ray beams, ± 4 MV – 25 MV. Lower energy ranges are generally better capable of imaging soft tissues and therefore used for diagnostic purposes. In contrast, higher energy ranges are more often used for treatment purposes. Additionally, MVCT shows advantages in the presence of metal implants. This arises from the capability of photons with higher energies to traverse metal implants and reach the detector, rather than being completely absorbed. Consequently, the occurrence of photon starvation and beam hardening is diminished when compared to kVCT imaging, leading to a reduction in metal artifacts [61], [62].

The results of the experiments conducted in the study by Zhao et al. [45] showed that the metal part of the implants caused large dose perturbations, primarily created by electron fluence: a 4 mm diameter metal port decreased the proton fluence by up to 79%. Additionally, a dose increase around the implant was detected. The TPS calculation algorithm could not accurately calculate this. When comparing kVCT and MVCT imaging, they reported that MVCT imaging created less image artifacts, making it possible to create more precise delineation.

Conversion of HU to RSP

As was mentioned in the previous sections, CT images are represented by HU's. To use CT scans for radiotherapy treatment planning, the HU's must be converted into suitable physical variables [63]. In photon therapy, this is done by using a HU to mass density table. Proton therapy differs from photon therapy in its approach to dose calculation. It uses the relative stopping power (RSP) to determine the loss of energy of protons traversing tissue, which subsequently is used to calculate the dose distribution. Thus, HU's need to be converted to RSP, which can be done by using an HU to RSP calibration curve [48].

The occurrence of metal-induced artifacts or intensity saturation leads to an incorrect representation of HU's, subsequently leading to a miscalculation of the corresponding RSP and thus a considerable reduction in the dose calculation accuracy [48], [54].

The included articles reported on strategies to incorporate this limitation into their workflow. Dietlicher et al. [47] corrected for metal implants by using a calibration curve in which the RSP corresponding to the highest HU value is modified to the RSP of the considered material. Several other articles used a similar approach [38], [48], [50], [57].

Overall, using an appropriate calibration curve for proton therapy dose calculation is crucial, especially in the presence of metal implants.

4.5.2 Density overrides

In the following section, the usage of density overrides is explained. Density overrides are often applied in proton therapy to correct for variations in tissue density, which are not correctly depicted on the CT scan. These variations can occur in regions with sharp density interfaces, for example in the presence of metals or air cavities. Density overrides can be applied manually or automatically. This is done by assigning the accurate HU value to the voxel with the incorrect HU value. An overview of the articles that implemented density overrides and their purpose of use is provided in Table IV.

Density overrides for artifact correction

Most of the articles report on using density overrides to correct for CT artifacts [41], [30], [38], [42], [44], [45], [46], [47], [48], [51], [56]. Hereby, voxels affected by (metal-induced) artifacts are delineated first. Thereafter, they are manually or automatically overwritten with either the HU values of the adjacent or neighboring tissue, which closely resembled the expected values, or with an average HU value, such as that of water [47]. Most of the articles used manual density override methods, and a few used an automated program in the TPS.

Material overrides

Moreover, it has been reported to apply density override for the material of the metal implant [41], [30], [37], [42], [43], [44], [45], [46], [48], [54].

Hu et al. [54] investigated the impact of dental implants on proton therapy. In their method, a metal artifact reduction algorithm was applied, using a form of an extended HU scale to account for the high-density implants. Although this technique helps mitigate the disadvantages of intensity saturation, it also reduces the accuracy of the overall HU values. Therefore, the implants were delineated and overwritten by replacing the HU values with representative stopping power values. This enabled the TPS to more accurately model the interaction between the proton beam and the implants and improved dose calculation.

Additionally, their research concentrated on investigating the dose-shadowing effects caused by metal implants. They made a comparison between treatment plans created without implant overrides and treatment plans where implant overrides were applied and included in the optimization process. Although they found severe cold spots distal to the metal implants for both cases, the cold spots were reduced when the materials were overridden. This was possible because overriding the implants with their correct RSP's made sure that the TPS could better account for the correct HU values.

Righetto et al. [10] stated that the override of implants is not suitable for every case. In their research, they investigated titanium fixation screws. When implants are small and have irregular surfaces, the delineation of the implant is difficult and is presumably not accurate. Additionally, the occurrence of the partial volume effect will cause either a too large or small delineation.

4.5.3 Dose calculation

Dose calculation is an important aspect of every treatment planning process, and therefore, many different dose calculation algorithms have been developed over the years. The two main algorithms reported by the articles included in this review are Pencil-Beam and Monte Carlo algorithms.

As was mentioned in section 2.5 ‘Treatment planning: dose calculation’, MC algorithms show considerable advantages in the presence of metal implants. The majority of the included articles reported on the use of MC algorithms as their preferred dose calculation algorithm [41], [10], [19], [30], [38], [42], [43], [45], [46], [47], [48], [49], [50], [51], [54], [58]. Only four articles reported on using Pencil-Beam dose calculation algorithms [10], [53], [55], [56]. Additionally, two articles did not mention the specific type of dose calculation algorithm that was used in the study [44], [57].

The primary advantage of MC algorithms is the ability to accurately predict dose perturbations in the presence of metal implants. Newhauser et al. [58] determined the precision of various Monte Carlo codes. Their methods showed that the algorithms were relatively good in defining multiple Coulomb scattering caused by metal implants. The mean discrepancies between calculated and measured doses were roughly up to 5%. Additionally, they stated that MC-algorithms are eligible to be used as a benchmark method to test other calculation algorithms.

Paganetti et al. [49] investigated MC- and pencil beam algorithms for tumors in the skull base and spine. Overall, for patients without metal implants, the two algorithms showed similar results regarding dose calculation for target volumes. When metal implants were present, they demonstrated that the MC algorithm showed great advantages when compared to the PB algorithm, especially in heterogeneous areas. The differences were the most substantial for the OARs, which is probably due to their more complex anatomical interfaces.

In the research by Tourovsky et al. [50], MC algorithms were used to verify the dose calculated by a pencil beam dose calculation algorithm. They evaluated this on a clinical case involving titanium spinal implants and also reported on the profit of using MC algorithms in the presence of metal implants. They showed that MC algorithms can be used as a

TABLE IV: Reported metal-induced artifact density overrides and material density overrides per article.

Article	Metal-induced artifact override	Material override
Dietlicher et al.	Override to a mean soft tissue HU value	X
Fellin et al.	Override to HU of water	Material override with mass density of corresponding material
Fredriksson et al.	X	Material override with HU of corresponding material
Hu et al.	X	Material override to HU values with RSP values measured for the corresponding material
Kang et al.	X	Material override to HU values with RSP values measured for the corresponding material
Kirk et al.	Override to HU of water	Material override with varying RSP's
Kisielewicz et al.	Override to HU of neighboring tissues	Material override for materials with HU larger than the highest point in calibration curve
Mutter et al.	Override to HU of neighboring tissues	Material override with RSP of corresponding material
Poel et al.	Override to HU of neighboring tissues	Material override with correct RSP for materials where voxels reach the maximum HU scale of the CT scan
Rana et al.	Override to a mean soft tissue HU value	X
Shi et al.	Override to HU of neighboring tissues	X
Zhao et al.	Override to HU of neighboring tissues	Material override with HU of corresponding material
Zhu et al.	Override to HU of neighboring tissues	Material override with HU of corresponding material

tool to check the accuracy of pencil beam algorithms, because they are better capable of handling highly heterogeneous media. Figure 5, highlights the gains made by using MC algorithms when looking at target coverage and cold spots.

4.5.4 Avoidance of implants

In Section 4.4, the effects of the proton beam on metal implants are described. As was explained, multiple effects can occur, which often have a negative impact on treatment planning and delivery. Therefore, it is generally not recommended to cross metal implants with the proton beam. As a result, avoidance of the implants is determined to be the most optimal strategy to manage metal implants by several articles [30], [44], [46], [51], [56].

Fellin et al. [30] investigated the ability to avoid metal implants. This was done by determining an avoidance region around the implant, through which the proton beam is not allowed to pass. This region was created by adding a margin, representing the minimal distance that the proton beam must be from the implant to prevent the implant from affecting the dose distribution. In their experiments, they tested different margins on both copper and tantalum implants, for different setups (target depths, air gaps, and phantom depth). They found that for most of the setups, a spacing of 0.9–1.3 cm between the proton beam and the implant was large enough to create a maximal discrepancy in dose distribution under 5–10%. Thereby, they indicated that an avoidance margin could serve as a way to minimize the negative effects that metal implants can cause.

Rana et al. [56] investigated patients with hip prostheses who are treated for prostate cancer. They aimed to adjust the number of proton beams and their directions, with the goal of avoiding entrance through the implant. Meanwhile, a sufficiently high dosage must be applied to the CTV, and a low dosage to the OARs. Their approach was implemented successfully and they showed that by irradiating the prostate with 3 beams (instead of 2 beams that are used normally), and by applying beam setup of both lateral and oblique beams, all dose constraints were satisfied.

Both methods mentioned above indicate that avoiding metal implants can serve as an adequate strategy for applying proton therapy. However, there are often situations where avoiding irradiation through metal implants is not possible due to constraints in the treatment plan, such as limitations in beam direction or dose constraints for OARs. Therefore, the following sections report an overview of articles exploring strategies to address the challenges that occur when the proton beam traverses metal implants.

4.5.5 Beam specific adjustments

Some of the included articles reported on methods to account for metal implants by implementing beam-specific modifications.

Kang et al. [43] investigated proton therapy for patients with breast tissue expanders and they compared different plans with varying beam arrangements: a single-field and a multi-field plan. The single field plan involved delineating the metal component, adding a 1 cm lateral margin around it and including dose shadow components. An anterior-posterior (AP) or left anterior oblique (LAO) beam was used. The multi-field plans involved a 1 cm margin all around the implant. Here a plan was generated with 3 uniform distributed beams: an AP, an LAO and an RAO beam. These beams were optimized using SFO.

Their results showed that dose shadow areas created significant heterogeneities for a single field plan. Here the TPS miscalculated the dose by around 25%. Whereas for the multi-field plan, fewer heterogeneities were created, which resulted in a miscalculation of only 6%. Additionally, MC dose

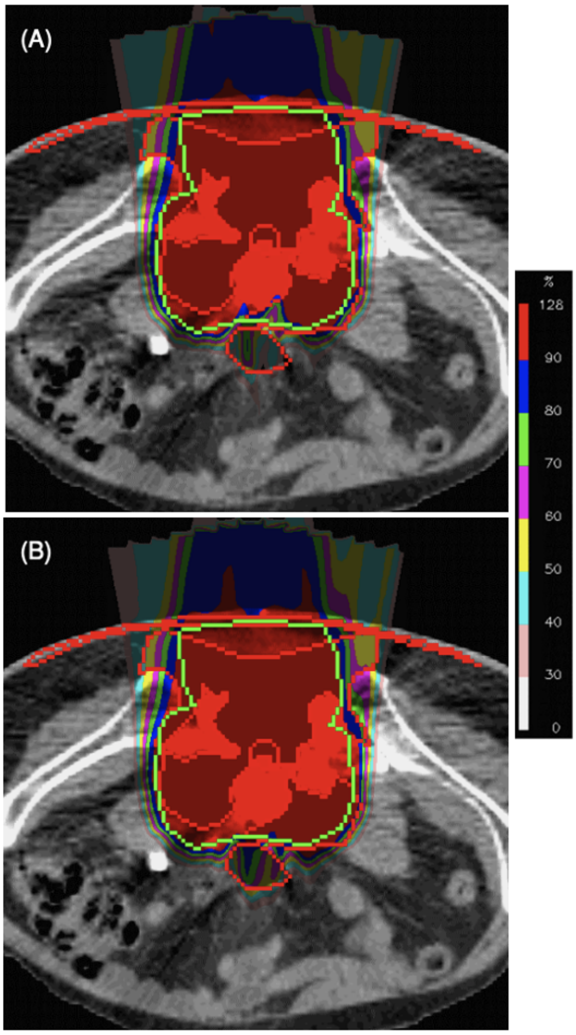

Fig. 5: This figure presents the dose distribution calculated by an analytical (A) and MC algorithm (B) for a patient with titanium spinal implants. For the distal end of the target, cold spots are visible in image A. The MC algorithm calculation shows a significant reduction of these spots, as depicted in image B [50]

calculation provided better agreement between the measured and calculated dose than the TPS algorithm.

Overall, they concluded that one should use multiple beams from different directions when treating patients with breast tissue expanders.

Righetto et al. [10] investigated the effect of titanium screws on proton therapy and applied their strategy to two patient cases. In their study, a method that reduces the need to use a range shifter was proposed. A range shifter is generally applied to modify the range of the proton beam. The range can be shifted to the desired depth. This is a useful tool and is often applied to irradiate superficial areas. However, it also introduces uncertainties such as setup errors, possible artifacts, and most importantly an increased lateral penumbra [64].

In their study they used a so-called ‘beam-splitting’ technique. Here, a plan was created in which a beam was separated into two components. One component was implemented to encompass the range of energy values that are able to provide irradiation at more superficial depths. This was done by using a range shifter. The other component includes all the other energy values, so no range shifter was utilized. They compared this with another plan containing a single beam with the addition of a range shifter. The beam-splitting setup proved to be effective in meeting the clinical objectives. These results indicate that by using this technique, the usage of a range shifter is not necessary, and thereby some of the above-mentioned uncertainties can be reduced.

4.5.6 Target delineation

Adding margins: PTV

As was mentioned in Section 2.4 ‘Treatment planning: delineation’, a method that is often used to account for uncertainties in the treatment plan is adding margins around the CTV, leading to a PTV. Several articles reported on ways to incorporate a modified PTV concept into their treatment planning process [19], [30], [37], [38], [47], [48], [50], [56], [57].

Nevertheless, as was mentioned in Section 2.7 ‘Correcting for uncertainties - Adding geometrical margins’, the PTV method is highly susceptible to uncertainties in proton therapy. This is mainly a problem when there are large heterogeneities present in the beam path, which is the case for metal implants [37]. This can be resolved by enlarging the PTV margins to a greater extent, but that introduces higher dosages to neighboring tissues [47]. It is possible to account for range and setup uncertainties via other methods, such as using robust optimization techniques. Therefore, the usage of PTV margins is not further investigated in this review. The usage of robust optimization is further elaborated on in section 4.8.5.

Field specific targets

Kirk et al. [44] proposed a strategy to account for metal parts in breast tissue expanders. They aimed to find a strategy that can be applied for patients from which the exact composition of the expander is not known. Their strategy was based on defining field-specific targets, thereby aiming to avoid the metal part of the expander. In step 1 of their approach, the implant was delineated and subtracted from the CTV. Secondly, the beam setup was determined, resulting in two beams: one anterior and one lateral to the target volume. Thereafter, the beam-specific targets were determined. Hereby, the volume delineated in step 1 was adjusted: the area behind the target was removed, see figure 6. This was done to reduce the effect of spot tails of the beams partially passing through the expander. Additionally, the lateral parts of the expander are adjusted to minimize the dose to critical organs. Moreover, the overlap region of the

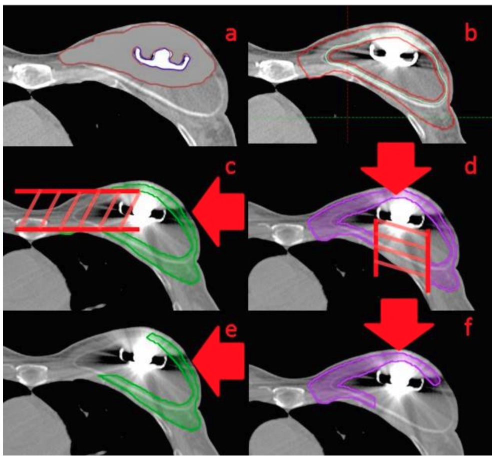

Fig. 6: This figure represents the strategy proposed by Kirk et al. [44]. In image C (lateral beam) and D (anterior beam), the part that is removed distally to the expander is displayed in red.

two beams is delineated. The part distal to this region is again removed from the target. Once the beam setup and targets were defined, MFO was applied to optimize the plan and the plan's robustness was analyzed. By applying this method, target coverage was achieved while the required robustness against the shift in stopping power was obtained.

4.5.7 Field optimization

In Section 2.7 'Correcting for uncertainties', different field optimization techniques were presented: SFO and MFO. As was mentioned, both approaches can be applied as a good method to correct uncertainties in treatment planning. An SFO method is characterized by creating a homogeneous plan that is robust against uncertainties. The MFO method is characterized by optimizing every beam independently, which makes it possible to irradiate heterogeneous areas more conformally. Therefore, the latter approach is more favorable to use in the presence of metal implants.

Fellin et al. [30] conducted experiments on metal implants to investigate an avoidance technique to manage the implants. The results of these experiments are presented in Section 4.5.1: Avoidance. After conducting their ex vivo experiments, they tested their strategy on a patient case. Here, an MFO technique was used to implement the treatment plans with the addition of a 0.9 cm avoidance margin. Dose calculations were performed by an MC algorithm and the plans were analyzed using robust optimization (with a 3.5 mm included error). Their results showed that the addition of the avoidance margins created an adequate treatment plan, in which, by optimizing the proton beams, avoidance of the implant could be obtained. However, the article pointed out that this technique is only suitable for implants that do not lie in the CTV. Additionally, the robust analysis indicated that setup errors might greatly affect the target coverage. This is mainly because by avoiding the implant, it is assumed that the proton beam only crosses normal tissues. When a setup error occurs and the proton beam will still cross the implant, underdosage to the tumor can occur. Additional care should be provided to avoid this complication.

For the application of proton therapy to patients with breast tissue expanders containing metal ports, DeCesaris et al. [42] developed a combined SFO-MFO approach, see Figure 7. Their strategy involved an SFO method in the area superior and inferior to the expander. Additionally, an MFO method was applied in the areas adjacent to the metal part of the expander. Also, a margin of 0.5 cm was added around the metal part of the expander, in which no spots were placed. They implemented their approach on several clinical treatment plans and obtained successful results, with all cases containing a median target coverage of 95% up to 100%. Additionally, the criteria regarding OAR sparing were largely fulfilled.

Zhu et al. [46] investigated a similar approach as DeCesaris et al. [42]. Their investigation also focussed on breast tissue expanders using a combined SFO-MFO approach. In addition, they delineated an avoidance area by projecting the metal part of the tissue expander distally and expanding

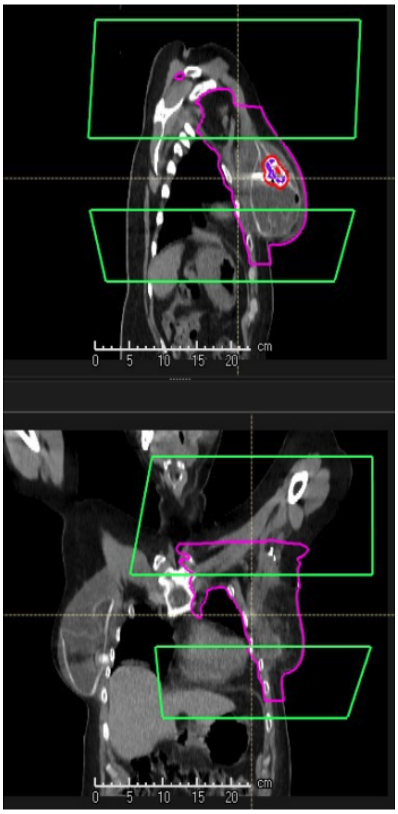

Fig. 7: The treatment plan for the combined SFO-MFO technique. In pink, the CTV is depicted. The green parts represent the areas treated with an SFO method, whereas the remaining areas of the CTV were treated with an MFO method [42].

that with a 5 mm margin. This was done for every beam independently and then summed up, creating one avoidance area for the combined beams. This approach resulted in successful treatment outcomes regarding CTV coverage.

Poel et al. [38] conducted a study in which they aimed to assess the difference in dosimetric impact between titanium and CFR-PEEK spinal stabilization implants. In their planning strategy, they compared a single-field SFO approach with a multi-field MFO approach. Their results were analyzed for planning accuracy and robustness. Gamma analysis was applied to evaluate the differences between the calculated and measured doses.

Their results showed favorable results for the MFO plan compared to the SFO plan, due to the aforementioned advantages of the MFO approach. Notable in the SFO approach was a decrease in dose distal to the implant, in the line of the proton beam. Meanwhile, an increase in the dose was measured on the lateral sides. These patterns can significantly impact treatment quality when not properly accounted for. Regarding the robust analysis, SFO created a more robust treatment plan, which arises from the fact that in MFO more modulations take place, resulting in a decrease in robustness. Overall, these results show that MFO can be better used in the presence of titanium spinal stabilization implants. Additionally, regarding the comparison between the titanium and CFR-PEEK implants, the latter showed advantages regarding CT-image artifacts, dosimetry accuracy, and plan robustness.

4.5.8 Robust Optimization

To date, several studies have investigated different Robust Optimization methods and there is still a lot of research conducted to expand and improve this technique. For this review, three articles have been included that focus on developing Robust Optimization methods and incorporating clinical cases with metal implants in their validation [37], [52], [53].

The main goal of implementing Robust Optimization is to account for range and setup uncertainties. Incorporating both types of uncertainties in the optimization process includes accounting for dose gradients in directions both parallel and perpendicular to the beam [52]. The range and setup uncertainty settings differ per clinical case (e.g. tumor location, size, and presence of metal implants) and preference of the medical institute. All articles included in this review that reported on using Robust Optimization to optimize their treatment plan are listed in Table V. Their approaches and settings were based on previous experiments or existing literature.

The focus of the method proposed by Unkelbach et al. [52] lies in a probabilistic methodology. Hereby, the dose distribution relies on the selection of arbitrary variables, that serve to represent the uncertainties that need to be incorporated. They included a three-dimensional setup error, representing the displacement of the patient relative to the isocenter, and a range error that was defined as the possible errors for every single beam. Thus, the uncertainties are represented by probability distributions. During the optimization of the treatment plan, different scenarios (one scenario encompasses one range and one setup parameter) were calculated and the weight per scenario was chosen based on the likelihood that a scenario takes place. As a result of this, the dose can be divided along the beams according to their objectives, creating a more robust treatment plan when compared with conventional methods (e.g. adding margins around the CTV). The protocol was validated on a clinical case including a surgical fixation implant in the spine.

TABLE V: An overview of the included articles that made use of Robust Optimization. The target area is depicted in combination with the applied setup and range uncertainty.

Article	**Target area**	**Setup uncertainty [mm]**	**Range uncertainty [%]**
DeCesaris et al.	Breast	5	3.5
Farace et al.	Spine	-	3.5
Fellin et al.	Head and neck area	2	3.5
Hu et al.	Head and neck area	3	3
Kirk et al.	Breast	3	3.5
Kisielewicz et al.	Skull base	3	3
Mutter et al.	Breast	5	3
Poel et al.	Spine	3.3	3
Shi et al.	Spine	3	3.5
Zhu et al.	Breast	5	3.5

Another method for implementing Robust Optimization includes a so-called ‘worst case scenario’ approach. This technique investigates worst-case (regarding range and setup uncertainties) situations during the optimization process [53]. A variance of the worst-case scenario approach was proposed by Fredriksson et al. [37]. Here, the plan is optimized by reducing the penalties associated with the most unfavorable or extreme scenario. The main advantage of this technique is that it incorporates only physically feasible scenarios. This is achieved by using non-linear optimization strategies. To illustrate: the voxels irradiated by the proton beam differ per scenario. Subsequently, their worst-case doses also differ per scenario. Thus, calculating the worst-case dose per voxel is not representative of real clinical situations. The proposed method incorporates these aspects and creates only realistic scenarios.

Overall, using Robust Optimization techniques shows promising results, especially when metal implants are located in the beam trajectory.

4.5.9 Treatment delivery

As mentioned in Part 1 of this review, there are two main ways to deliver proton therapy to patients: passive scattering and pencil beam scanning. In this review, articles that reported only on passive scattering techniques were excluded due to the reasons mentioned in Section 2.3. Two articles applied a strategy to handle metal implants based on different treatment delivery methods.

In the study by Dietlicher et al. [47], the effect of proton therapy on titanium implants was investigated by implementing three different treatment plans: two plans followed an SFUD approach, and one plan employed an IMPT approach. The main difference between these approaches is that the SFUD plans create a uniform dose throughout the CTV and an IMPT plan consists of non-uniform dose distributions within all the individual treatment fields. The IMPT plan and one of the SFUD plans included the usage of an artifact correction method (density overrides of artifacts), the second SFUD plan did not correct for any artifacts.

Overall, their experiments showed good similarity between calculated and measured dose distributions in the artifact-corrected plans: 97% of the evaluated points met the required gamma criterion (3 mm, 3%). For the SFUD plan without artifact correction, there were distinctions between the measured and calculated doses, and the gamma criterion was not met by 18% of the measured points. This was mostly in the points in proximity to the metal implants and led to a larger under-dosage for those areas.

Therefore they concluded that the addition of an artifact correction method is highly recommended in the presence of metal implants. However, there was a negligible difference between the SFUD and IMPT plans when they both included artifact correction.

Another article that explored the potential of IMPT was written by Farace et al. [57]. As was discussed extensively in Part 1 'Background information', proton therapy is more susceptible to uncertainties than photon therapy. These uncertainties affect the ability to precisely shape the dose gradients in proton therapy.

The dose gradient is the shift in radiation dose between two regions. In clinical practice, this is often used to determine the rate of dose change between the CTV and OARs. Dose gradients are related to the penumbra of the beam, which is the shift from high dose to low dose regions, and are measured relative to the central axis of the proton beam, see Figure 8. To minimize the dose to OARs, a sharp lateral penumbra, which results in a steeper dose gradient, is desired [65].

In the article from Farace et al. [57], a method utilizing solely the lateral penumbras of the proton beam to create steep dose gradients was proposed. This was achieved by implementing a single energy IMPT (SE-IMPT) method. In SE-IMPT the dose gradient primarily arises from the lateral penumbra, similar as is the case for photon irradiation beams. The energy that was used was 226 MeV (the system's maximum attainable energy level).

Experiments were performed on titanium implants in a phantom and clinical case. First, they investigated the lateral penumbras created by high-energy beams. Thereafter, an SE-IMPT plan was compared with an MFO-IMPT and an SFO-IMPT plan. The SE-IMPT plan showed similar results to the MFO-IMPT plan regarding the dose objectives. Thereby, endorsing the fact that SE-IMPT is able to produce sharp lateral penumbras and therefore create adequate treatment plans. Additionally, the SE-IMPT plan showed better results when compared to the SFO-IMPT plan.

This article indicates that SE-IMPT can be used as a sufficient technique to create adequate treatment plans in the presence of metal implants.

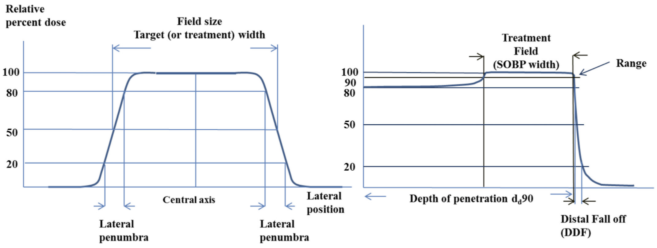

Fig. 8: Properties of the proton beam and factors related to the dose distribution [65].

5. DISCUSSION AND CONCLUSION

Reflection on findings

This literature review is conducted to gain a better understanding on the effects of metal implants on proton therapy. Part 1 of the review includes an overview of the general characteristics of proton therapy. In Part 2 it was aimed to evaluate various strategies employed in current literature to manage metal implants in proton therapy.

Overall it can be stated that metal implants can significantly impact the accuracy and effectiveness of proton therapy treatment planning and delivery. Therefore, there is a high need to find strategies to incorporate the accompanying uncertainties and correct them.

The proton therapy workflow is initiated by making a CT scan on which the treatment planning will be performed. Several strategies focused on aspects related to CT imaging. It was reported by Righetto et al. and Poel et al. that correcting for artifacts, either by using metal artifact reduction algorithms or by applying density overrides to the voxels affected by the artifacts, is crucial in providing accurate treatment planning [10], [38]. Additionally, the partial volume effect and intensity saturation should be considered when determining the CT acquisition protocol [30]. Moreover, it was found by Zhao et al. that MVCT protocols are preferred over kVCT protocols for cases involving metal implants [45]. Lastly, one of the issues that emerges from the presented findings is the importance of the correct conversion of HU's to RSP, since this is a significant source of uncertainty [47], [48].

In addition to the usage for artifact correction, density overrides are also applied to metal implants. Dietlicher et al. researched that this can ensure a more accurate dose calculation and therefore, more accurate treatment planning [47].

Another finding that stands out from the reported results is the advantage of using MC dose calculation algorithms compared to Pencil-Beam dose calculation algorithms when metal implants are present [49], [50], [58].

Moreover, the results of this study suggest that in principle, avoiding metal implants is the best way to minimize treatment inaccuracies. This can be done by adding avoidance margins around the implant or increasing the number of proton beams if irradiation from different directions is possible [30], [56].

In situations where it is not possible to avoid the implants, making beam-specific adjustments can offer a potential solution. Careful adjustment of beam angles and orientations becomes crucial in such cases. Additionally, it was observed in the literature that incorporating more beams proves to be a more effective approach when accommodating metal implants [10], [43].

The application of PTV margins has been consistently found to be sub-optimal for proton therapy in general. In contrast, Kirk et al. reported that the delineation of field-specific targets shows promise in achieving better outcomes, particularly in heterogeneous areas where different tissue densities are present. By defining targets specific to each treatment field, it becomes possible to account for variations in material composition and optimize the dose distribution accordingly. This approach offers potential improvements in managing the presence of metal implants, mitigating the impact of heterogeneity on proton therapy outcomes [44].

During the optimization of treatment plans for proton therapy, various methods can be employed to improve treatment delivery in the presence of metal implants. Notably, the inclusion of an avoidance margin [30] or the utilization of a hybrid SFO-MFO approach [42], [46] have demonstrated their effectiveness in achieving accurate treatment outcomes. Furthermore, in the vicinity of metal implants, MFO has been found to offer advantages over SFO [38].

Another optimization method that has shown promising results is Robust Optimization. This method involves optimization directly on the CTV without the use of a PTV and incorporates the estimation of secondary particle occurrences. By optimizing worst-case scenarios, Robust Optimization consistently demonstrates favorable overall results [19], [37], [53].

Limitations

A limitation of this study is that it did not compare articles based on a single primary outcome. Some articles reported their outcomes based on a comparison between measured and calculated doses, while others focused on CTV coverage or OAR sparing. This raises concerns about the comparability of the outcomes. Nevertheless, the decision was made not to compare the studies based on a single outcome, but instead conduct a qualitative analysis. This approach was chosen to avoid excluding important articles that might have been overlooked if a single primary outcome was selected.

Additionally, this review included various types of implants composed of different materials, which raises further doubts about the comparability of treatment planning techniques. Overall, precise knowledge of the composition of the implant is essential to determine the most appropriate treatment planning strategy [41], [66]. Unfortunately, in clinical practice, obtaining information about patient implants is sometimes challenging as it may not always be readily available.

In this review, when assessing the success of proton therapy, it is argued that incorrect treatment planning and delivery are the primary causes of failures. However, it is worth considering that it may not be the effect of protons on the implants and the accompanying uncertainties that lead to failure, but rather the influence of the implants on the tumors, potentially making the tumors more aggressive [38], [47]. Additionally, it is argued that the presence of implants makes a priory surgery more difficult, which subsequently also has an influence on treatment outcomes [38], [47].

In conclusion, it can be stated that the presence of implants is an indicator of treatment failure, however, it is essential to further investigate whether this is due to inaccurate treatment planning techniques or whether other aspects are the cause of this.

Future research

Each article in the study reported on different measurement methods employed to conduct their experiments, e.g. using film dosimetry or ionization chambers. It is evident that different measurement methods possess varying levels of accuracy and excel in assessing different aspects. Consequently, it is of interest to determine the optimal measurement methods to employ in the specific context of investigating proton therapy in the presence of metal implants.

Moreover, some articles in this review compared metal with non-metal implants. The utilization of non-metal implants has demonstrated numerous advantages. For instance, the application of CFR-PEEK implants offers benefits such as reduced artifacts in CT imaging and minimized range shifts in proton therapy. These findings prompt whether it would be more advantageous to utilize non-metal implants exclusively. Further research is required to investigate the applicability of non-metal materials for implants [38], [51], [67].

Despite the above-mentioned challenges, this study demonstrates the potential of mitigating the impact of metal implants on proton therapy. The implementation of these strategies has the ability to enhance treatment accuracy and improve outcomes for patients with metal implants.

REFERENCES

[1] W. P. Levin, H. Kooy, J. S. Loeffler, and T. F. DeLaney, "Proton beam therapy," *Br. J. Cancer*, vol. 93, pp. 849–854, Oct. 2005.

[2] C. Allen, S. Her, and D. A. Jaffray, "Radiotherapy for cancer: Present and future," *Adv Drug Deliv Rev*, vol. 109, pp. 1–2, 2017.

[3] G. Noel and D. Antoni, "Organs at risk radiation dose constraints," *Cancer Radiother*, vol. 26, no. 1-2, pp. 59–75, 2022.

[4] H. Liu and J. Y. Chang, "Proton therapy in clinical practice," *Chinese Journal of Cancer*, vol. 30, no. 5, p. 315, May 2011.

[5] A. Knopf and A. Lomax, "In vivo proton range verification: a review," *Phys. Med. Biol.*, vol. 58, no. 15, p. R131, Jul. 2013.

[6] "Brain Tumors: Radiation Therapy," Nov. 2021, [Online; accessed 3. Apr. 2023]. [Online]. Available: https://www.hopkinsmedicine.org/health/conditions-and-diseases/brain-tumor/brain-tumors-radiation-therapy

[7] M. Piccirilli, G. Spena, E. Marchese, M. P. Tropeano, and A. Santoro, "A new device for bone cranial flap fixation: Technical note and surgical remarks. A multicentric experience," *Surgical Neurology International*, vol. 12, 2021.

[8] W. B. et al., "Titanium miniplates or stainless steel wire for cranial fixation: a prospective randomized comparison," *J. Neurosurg.*, vol. 96, 2002.

[9] "Titanium Cranial Flap Tube Clamps | DePuy Synthes," Aug. 2023, [Online; accessed 11. Aug. 2023]. [Online]. Available: https://www.jnjmedtech.com/en-US/product/titanium-cranial-flap-tube-clamps

[10] R. Righetto, L. P. Clemens, S. Lorentini, F. Fracchiolla, C. Algranati, F. Tommasino, F. Dionisi, M. Cianchetti, M. Schwarz, and P. Farace, "Accurate proton treatment planning for pencil beam crossing titanium fixation implants," *Phys. Med.*, vol. 70, pp. 28–38, Feb. 2020.

[11] D. et al., *Practical Radiation Oncology*, Feb. 2023.

[12] A. Pehlivanlı and M. H. Bölükdemir, "Investigation of the effects of biomaterials on proton Bragg peak and secondary neutron production by the Monte Carlo method in the slab head phantom," *Appl. Radiat. Isot.*, vol. 180, p. 110060, Feb. 2022.

[13] W. D. Newhauser and R. Zhang, "The physics of proton therapy," *Phys. Med. Biol.*, vol. 60, no. 8, p. R155, Mar. 2015.

[14] T. Terasawa, T. Dvorak, S. Ip, G. Raman, J. Lau, and T. A. Trikalinos, "Systematic Review: Charged-Particle Radiation Therapy for Cancer," *Ann. Intern. Med.*, Oct. 2009.

[15] "Types of Cancer Treatment," Aug. 2023, [Online; accessed 11. Aug. 2023]. [Online]. Available: https://www.cancer.gov/about-cancer/treatment/types

[16] A. Beddok and A. Vela, "Proton therapy for head and neck squamous cell carcinomas: A review of the physical and clinical challenges," *Radiother. Oncol.*, vol. 147, pp. 30–39, Jun. 2020, [Online; accessed 4. Apr. 2023].

[17] M. Chuong, S. N. Badiyan, M. Yam, Z. Li, K. Langen, W. Regine, C. Morris, I. James Snider, M. Mehta, S. Huh, M. Rutenberg, and R. C. Nichols, "Pencil beam scanning versus passively scattered proton therapy for unresectable pancreatic cancer," *Journal of Gastrointestinal Oncology*, vol. 9, no. 4, p. 687, Aug. 2018.

[18] G. C. Pereira, M. Traughber, and R. F. Muzic, Jr., "The Role of Imaging in Radiation Therapy Planning: Past, Present, and Future," *Biomed Res. Int.*, vol. 2014, 2014.

[19] J. Unkelbach and T. Bortfeld, "The role of computational methods for automating and improving clinical target volume definition," *Radiother. Oncol.*, vol. 153, pp. 15–25, Dec. 2020.

[20] J. Saini, E. Traneus, D. Maes, R. Regmi, S. R. Bowen, C. Bloch, and T. Wong, "Advanced Proton Beam Dosimetry Part I: review and performance evaluation of dose calculation algorithms," *Translational Lung Cancer Research*, vol. 7, no. 2, p. 171, Apr. 2018.

[21] F. De Martino, S. Clemente, C. Graeff, G. Palma, and L. Cella, "Dose Calculation Algorithms for External Radiation Therapy: An Overview for Practitioners," *Applied Sciences*, vol. 11, no. 15, p. 6806, Jul. 2021.

[22] K. Jabbari, "Review of Fast Monte Carlo Codes for Dose Calculation in Radiation Therapy Treatment Planning," *Journal of Medical Signals and Sensors*, vol. 1, no. 1, p. 73, Jan. 2011. [Online]. Available: https://www.ncbi.nlm.nih.gov/pmc/articles/PMC3317764

[23] A. Staab, H. P. Rutz, C. Ares, B. Timmermann, R. Schneider, A. Bolsi, F. Albertini, A. Lomax, G. Goitein, and E. Hug, "Spot-Scanning-Based Proton Therapy for Extracranial Chordoma," *International Journal of Radiation Oncology*Biology*Physics*, vol. 81, no. 4, pp. e489–e496, Nov. 2011.

[24] L. Lin, P. A. Taylor, J. Shen, J. Saini, M. Kang, I. I. Charles B. Simone, J. D. Bradley, Z. Li, and Y. Xiao, "NRG Oncology Survey of Monte Carlo Dose Calculation Use in US Proton Therapy Centers," *International Journal of Particle Therapy*, vol. 8, no. 2, p. 73, 2021.

[25] E. J. Tryggestad, W. Liu, M. D. Pepin, C. L. Hallemeier, and T. T. Sio, "Managing treatment-related uncertainties in proton beam radiotherapy for gastrointestinal cancers," *Journal of Gastrointestinal Oncology*, vol. 11, no. 1, p. 212, Feb. 2020.

[26] J. Unkelbach and H. Paganetti, "Robust Proton Treatment Planning: Physical and Biological Optimization," *Semin. Radiat. Oncol.*, vol. 28, no. 2, p. 88, Apr. 2018.

[27] B. Segedin and P. Petric, "Uncertainties in target volume delineation in radiotherapy – are they relevant and what can we do about them?" *Radiology and Oncology*, vol. 50, no. 3, p. 254, Sep. 2016.

[28] Z. Yang and Y. Chang, "Effect of setup and inter-fraction anatomical changes on the accumulated dose in CT-guided breath-hold intensity modulated proton therapy of liver malignancies," *Radiother. Oncol.*, vol. 134, pp. 101–109, May 2019.

[29] Y. Jia, L. Zhao, C.-W. Cheng, M. W. McDonald, and I. J. Das, "Dose perturbation effect of metallic spinal implants in proton beam therapy," *J. Appl. Clin. Med. Phys.*, vol. 16, no. 5, p. 333, Sep. 2015.

[30] F. Fellin, M. Artoni, R. Righetto, V. E. Bellinzona, L. Widesott, F. Dionisi, and P. Farace, "An avoidance method to minimize dose perturbation effects in proton pencil beam scanning treatment of patients with small high-Z implants," *Phys. Med. Biol.*, vol. 65, no. 14, p. 14NT01, Jul. 2020.

[31] P. C. Park, X. R. Zhu, A. K. Lee, N. Sahoo, A. D. Melancon, L. Zhang, and L. Dong, "A beam-specific planning target volume (PTV) design for proton therapy to account for setup and range uncertainties," *Int. J. Radiat. Oncol. Biol. Phys.*, vol. 82, no. 2, pp. 329–336, Feb. 2012.

[32] B. C. J. Cho, M. van Herk, B. J. Mijnheer, and H. Bartelink, "The effect of set-up uncertainties, contour changes, and tissue inhomogeneities on target dose-volume histograms," *Med. Phys.*, vol. 29, no. 10, pp. 2305–2318, Oct. 2002.

[33] M. Engelsman and H. M. Kooy, "Target volume dose considerations in proton beam treatment planning for lung tumors," *Med. Phys.*, vol. 32, no. 12, pp. 3549–3557, Dec. 2005.

[34] M. F. Moyers, D. W. Miller, D. A. Bush, and J. D. Slater, "Methodologies and tools for proton beam design for lung tumors," *Int. J. Radiat. Oncol. Biol. Phys.*, vol. 49, no. 5, pp. 1429–1438, Apr. 2001.

[35] E. M. Quan, W. Liu, R. Wu, Y. Li, S. J. Frank, X. Zhang, X. R. Zhu, and R. Mohan, "Preliminary evaluation of multifield and single-field optimization for the treatment planning of spot-scanning proton therapy of head and neck cancer," *Med. Phys.*, vol. 40, no. 8, Aug. 2013.

[36] M. Cubillos-Mesías, M. Baumann, E. G. C. Troost, F. Lohaus, S. Löck, C. Richter, and K. Stützer, "Impact of robust treatment planning on single- and multi-field optimized plans for proton beam therapy of unilateral head and neck target volumes," *Radiation Oncology (London, England)*, vol. 12, 2017.

[37] A. Fredriksson, A. Forsgren, and B. Hårdemark, "Minimax optimization for handling range and setup uncertainties in proton therapy," *Med. Phys.*, vol. 38, no. 3, pp. 1672–1684, Mar. 2011.

[38] R. Poel, F. Belosi, F. Albertini, M. Walser, A. Gisep, A. J. Lomax, and D. C. Weber, "Assessing the advantages of CFR-PEEK over titanium spinal stabilization implants in proton therapy-a phantom study," *Phys. Med. Biol.*, vol. 65, no. 24, p. 245031., Dec. 2020.

[39] "The Periodic Table Of Metals And Nonmetals - Science Trends," Mar. 2020, [Online; accessed 14. Aug. 2023]. [Online]. Available: https://sciencetrends.com/the-full-periodic-table-of-metals-and-nonmetals-and-their-location

[40] J. Unkelbach, T. C. Y. Chan, and T. Bortfeld, “Accounting for range uncertainties in the optimization of intensity modulated proton therapy,” *Phys. Med. Biol.*, vol. 52, no. 10, p. 2755, Apr. 2007.

[41] R. W. Mutter and N. B. Remmes, “Initial clinical experience of post-mastectomy intensity modulated proton therapy in patients with breast expanders with metallic ports,” *Practical Radiation Oncology*, vol. 7, no. 4, pp. e243–e252, Jul. 2017, [Online; accessed 20. Apr. 2023].

[42] C. M. DeCesaris, S. Mossahebi, J. Jatczak, A. D. Rao, M. Zhu, M. V. Mishra, and E. Nichols, “Outcomes of and treatment planning considerations for a hybrid technique delivering proton pencil-beam scanning radiation to women with metal-containing tissue expanders undergoing post-mastectomy radiation,” *Radiother. Oncol.*, vol. 164, pp. 289–298, Nov. 2021.

[43] Y. Kang, J. Shen, M. Bues, Y. Hu, W. Liu, and X. Ding, “Technical Note: Clinical modeling and validation of breast tissue expander metallic ports in a commercial treatment planning system for proton therapy,” *Med. Phys.*, vol. 48, no. 11, pp. 7512–7525, Nov. 2021.

[44] M. Kirk, G. Freedman, T. Ostrander, and L. Dong, “Field-Specific Intensity-modulated Proton Therapy Optimization Technique for Breast Cancer Patients with Tissue Expanders Containing Metal Ports,” *Cureus*, vol. 9, no. 9, p. e1698., Sep. 2017.

[45] L. Zhao, V. P. Moskvin, C.-W. Cheng, and I. J. Das, “Dose perturbation caused by metallic port in breast tissue expander in proton beam therapy,” *Biomed. Phys. Eng. Express*, vol. 6, no. 6, p. ., Nov. 2020.

[46] M. Zhu, K. Langen, E. M. Nichols, Y. Lin, S. Flampouri, K. D. Godette, S. W. Dutta, M. W. McDonald, and S. A. Patel, “Intensity Modulated Proton Therapy Treatment Planning for Postmastectomy Patients with Metallic Port Tissue Expanders,” *Adv. Radiat. Oncol.*, vol. 7, no. 1, p. 100825., Oct. 2021.

[47] I. Dietlicher, M. Casiraghi, C. Ares, A. Bolsi, D. C. Weber, A. J. Lomax, and F. Albertini, “The effect of surgical titanium rods on proton therapy delivered for cervical bone tumors: experimental validation using an anthropomorphic phantom,” *Phys. Med. Biol.*, vol. 59, no. 23, p. 7181, Nov. 2014.

[48] K. Kisielewicz, E. Góra, T. Skóra, B. Kiełtyka, M. Garbacz, M. Rydygier, D. Krzempek, and R. Kopeć, “Safe Proton Radiotherapy for Patients with Metallic Spine Stabilization System,” *Acta Phys. Pol. A*, vol. 142, no. 3, pp. 351–355, Sep. 2022.

[49] H. Paganetti, K. Parodi, H. Jiang, J. A. Adams, and H. M. Kooy, “Comparison of pencil-beam and Monte Carlo calculated dose distributions for proton therapy of skull-base and para-spinal tumors,” *SpringerLink*, pp. 2219–2222, 2007.

[50] A. Tourovsky, A. J. Lomax, U. Schneider, and E. Pedroni, “Monte Carlo dose calculations for spot scanned proton therapy,” *Phys. Med. Biol.*, vol. 50, no. 5, pp. 971–981, Mar. 2005.

[51] C. Shi, H. Lin, S. Huang, W. Xiong, L. Hu, I. Choi, R. Press, S. Hasan, C. Simone, and A. Chhabra, “Comprehensive Evaluation of Carbon-Fiber-Reinforced Polyetheretherketone (CFR-PEEK) Spinal Hardware for Proton and Photon Planning,” *Technol. Cancer Res. Treat.*, vol. 21, p. 15330338221091700., Jan. 2022.

[52] J. Unkelbach, T. Bortfeld, B. C. Martin, and M. Soukup, “Reducing the sensitivity of IMPT treatment plans to setup errors and range uncertainties via probabilistic treatment planning,” *Med. Phys.*, vol. 36, no. 1, p. 149, Jan. 2009.

[53] D. Pflugfelder, J. J. Wilkens, and U. Oelfke, “Worst case optimization: a method to account for uncertainties in the optimization of intensity modulated proton therapy,” *Phys. Med. Biol.*, vol. 53, no. 6, pp. 1689–1700, Mar. 2008.

[54] Y.-H. Hu, W. C. T. H. Seum, A. Hunzeker, O. Muller, R. L. Foote, and D. W. Mundy, “The effect of common dental fixtures on treatment planning and delivery for head and neck intensity modulated proton therapy,” *J. Appl. Clin. Med. Phys.*, vol. e13973., Mar. 2023.

[55] C. Oancea, K. Shipulin, G. Mytsin, A. Molokanov, D. Niculae, I. Ambrožová, and M. Davídková, “Effect of titanium dental implants on proton therapy delivered for head tumors: experimental validation using an anthropomorphic head phantom,” *J. Instrum.*, vol. 12, no. 03, p. C03082, Mar. 2017.

[56] S. Rana, C. Cheng, Y. Zheng, W. Hsi, O. Zeidan, N. Schreuder, C. Vargas, and G. Larson, “Dosimetric study of uniform scanning proton therapy planning for prostate cancer patients with a metal hip prosthesis, and comparison with volumetric-modulated arc therapy,” *J. Appl. Clin. Med. Phys.*, vol. 15, no. 3, p. 4611., May 2014.

[57] P. Farace, R. Righetto, and M. Cianchetti, “Single-energy intensity modulated proton therapy,” *Phys. Med. Biol.*, vol. 60, no. 19, pp. 357–367, Oct. 2015.

[58] W. D. Newhauser, L. Rechner, D. Mirkovic, P. Yepes, N. C. Koch, U. Titt, J. D. Fontenot, and R. Zhang, “Benchmark measurements and simulations of dose perturbations due to metallic spheres in proton beams,” *Radiat. Meas.*, vol. 58, pp. 37–44, Nov. 2013.

[59] D. Krzempek, G. Mianowska, N. Bassler, L. Stolarczyk, R. Kopec, B. Sas-Korczynska, and P. Olko, “CALIBRATION OF GAFCHROMIC EBT3 FILM FOR DOSIMETRY OF SCANNING PROTON PENCIL BEAM (PBS),” *Radiat. Prot. Dosim.*, vol. 180, no. 1-4, pp. 324–328, Aug. 2018.

[60] V. Grilj and D. J. Brenner, “LET dependent response of GafChromic films investigated with MeV ion beams,” *Phys. Med. Biol.*, vol. 63, no. 24, p. 245021., Dec. 2018.

[61] G. Liugang, S. Hongfei, N. Xinye, F. Mingming, C. Zheng, and L. Tao, “Metal artifact reduction through MVCBCT and kVCT in radiotherapy,” *Sci. Rep.*, vol. 6, p. 37608., Nov. 2016.

[62] W. Jackowiak, B. Bak, A. Kowalik, A. Ryczkowski, M. Skórska, and M. Paszek-Widzińska, “Influence of the type of imaging on the delineation process during the treatment planning,” *Reports of Practical Oncology and Radiotherapy*, vol. 20, no. 5, p. 351, Sep. 2015.

[63] C. Decoene and F. Crop, “Using density computed tomography images for photon dose calculations in radiation oncology: A patient study,” *Physics and Imaging in Radiation Oncology*, vol. 27, p. 100463, Jul. 2023.

[64] F. Fracchiolla, F. Fellin, M. Innocenzi, M. Lipparini, S. Lorentini, L. Widesott, P. Farace, and M. Schwarz, “A pre-absorber optimization technique for pencil beam scanning proton therapy treatments,” *Phys. Med.*, vol. 57, pp. 145–152, Jan. 2019.

[65] B. Arjomandy, P. Taylor, C. Ainsley, S. Safai, N. Sahoo, M. Pankuch, J. B. Farr, S. Y. Park, E. Klein, J. Flanz, E. D. Yorke, D. Followill, and Y. Kase, “AAPM task group 224: Comprehensive proton therapy machine quality assurance,” *Med. Phys.*, vol. 46, no. 8, pp. e678–e705, Aug. 2019.

[66] J. Cheung, R. J. Kudchadker, X. R. Zhu, A. K. Lee, and W. D. Newhauser, “Dose perturbations and image artifacts caused by carbon-coated ceramic and stainless steel fiducials used in proton therapy for prostate cancer,” *Phys. Med. Biol.*, vol. 55, no. 23, pp. 7135–7147, Dec. 2010.

[67] E. Mastella and S. Molinelli, “Dosimetric characterization of carbon fiber stabilization devices for post-operative particle therapy,” *Physica Med.*, vol. 44, pp. 18–25, Dec. 2017, [Online; accessed 2. May 2023].

B

Experiments using the Lynx Detector

Note: all the plots in this Appendix are normalized to the maximum value.

B.1. Experimental results: different scenarios

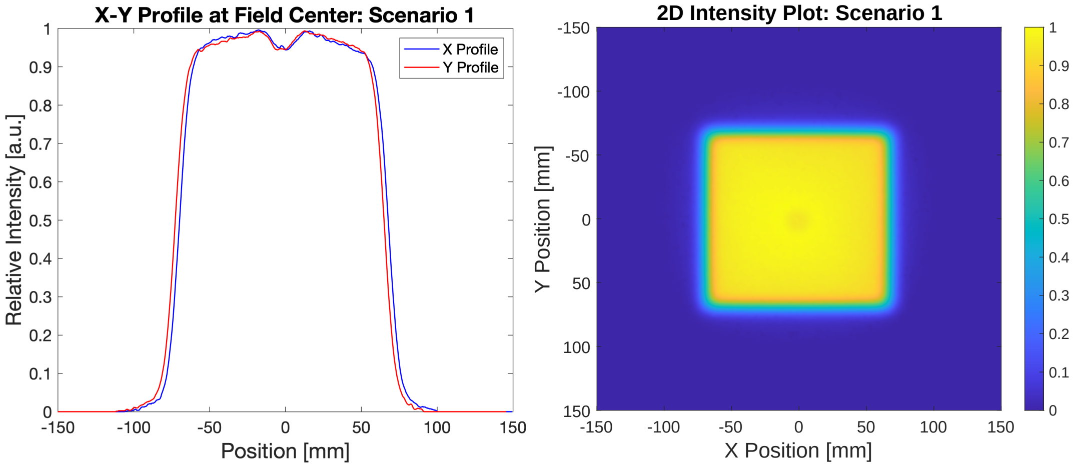

(a) (b)

Figure B.1: Scenario 1

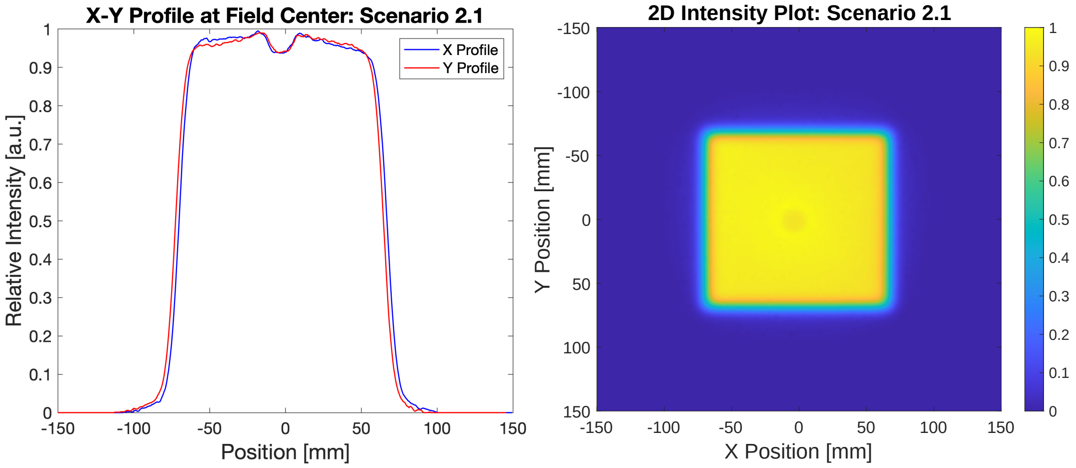

(a) (b)

Figure B.2: Scenario 2.1

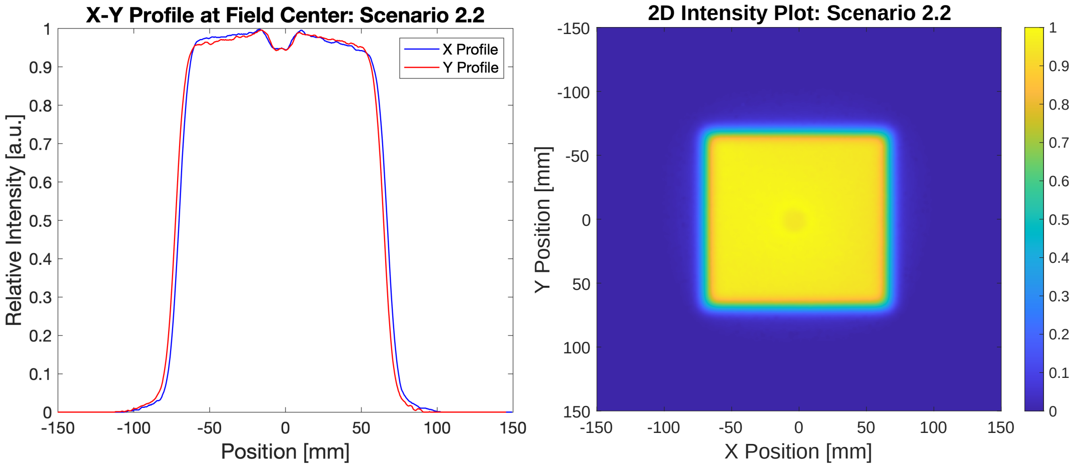

(a) (b)

Figure B.3: Scenario 2.2

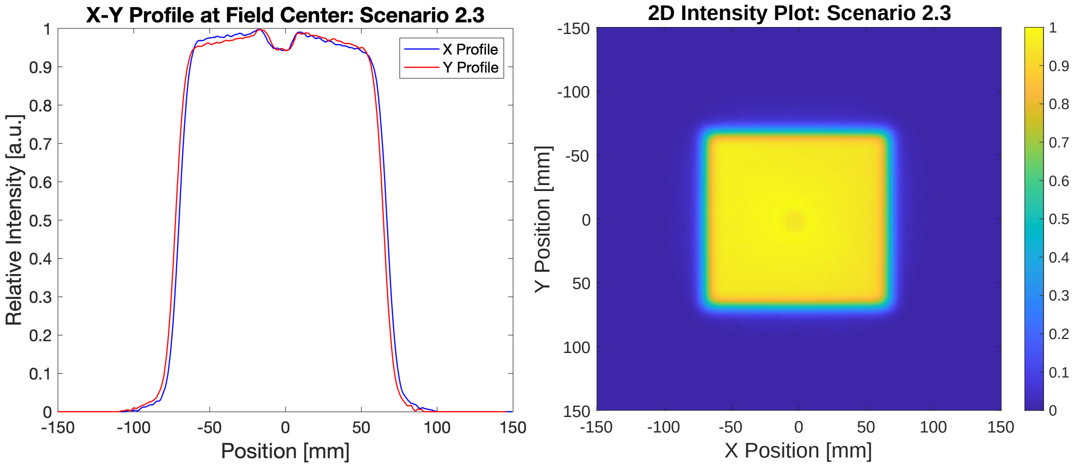

(a) (b)

Figure B.4: Scenario 2.3

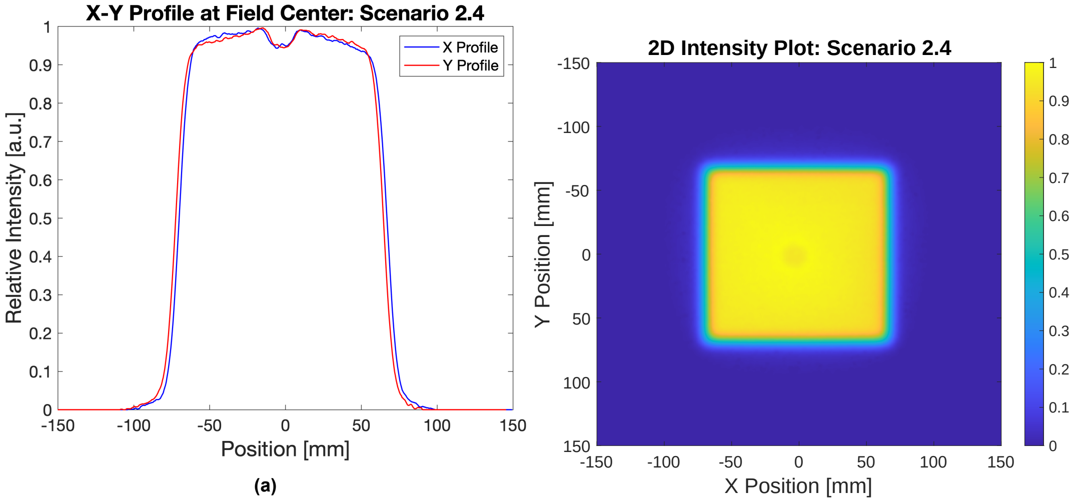

(a)

Figure B.5: Scenario 2.4

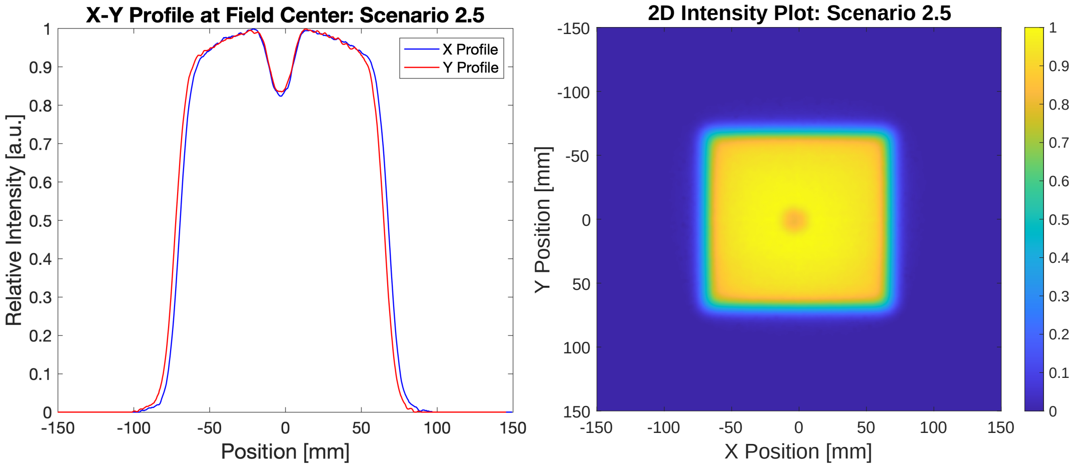

(a) (b)

Figure B.6: Scenario 2.5

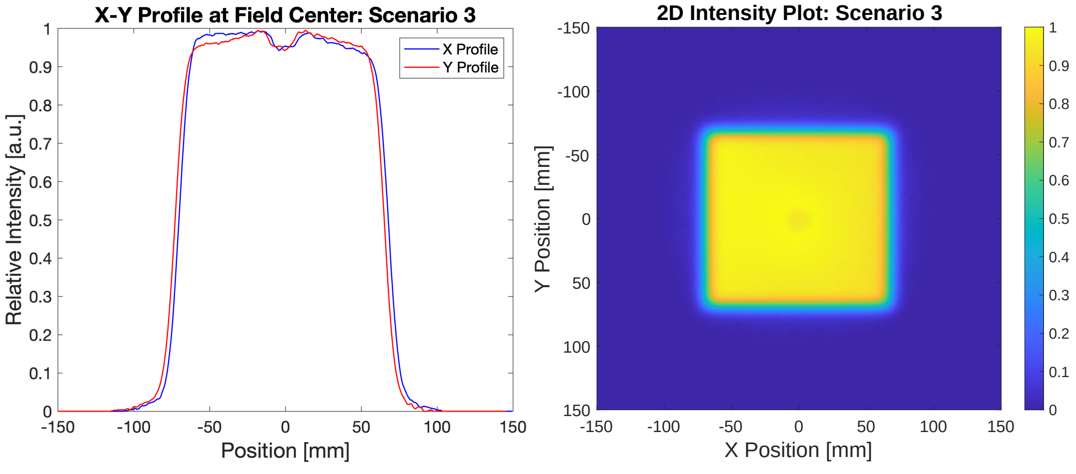

(a) (b)

Figure B.7: Scenario 3

B.2. Experimental results: Placing clip 4 cm off beam

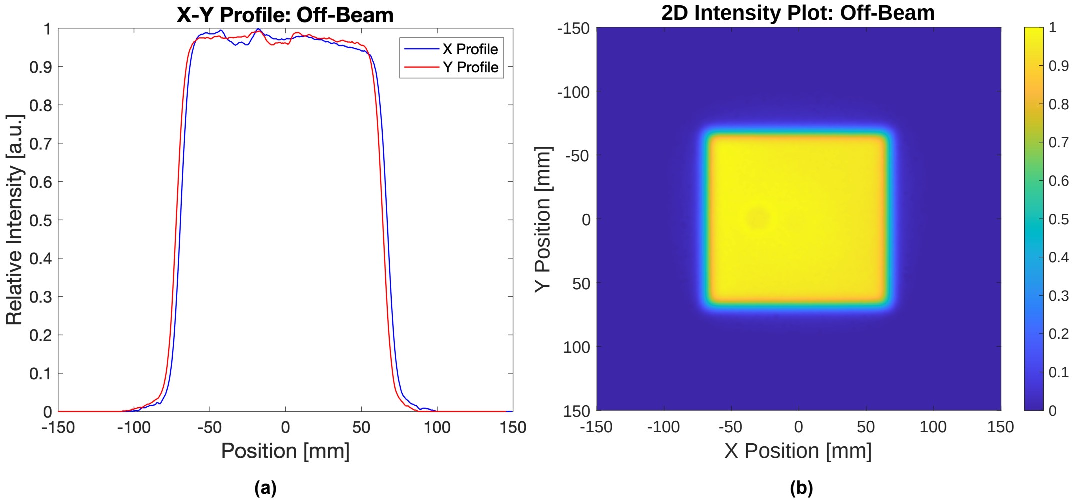

Figure B.8: Base experiment 1: 55 mm RW3 in front and no RW3 after clip

C

Experiments using gafchromic films

Figure C.1 presents the used calibration curve for the experiments presented in Section 4.1.3. The calibration data was obtained by employees at HollandPTC and was provided to be used in this thesis.

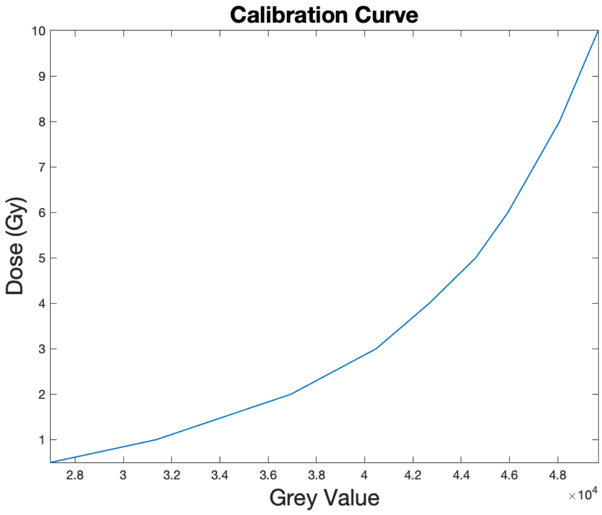

Figure C.1

D

Optimization settings

This appendix provides an overview of the supplementary optimization settings utilized in Raystation throughout the development of all treatment plans.

- Optimization settings
  - Optimization tolerance: 1.0×10^{-7}
  - Max number of iterations: 100
- Spot filtering settings
  - Iterations before spot filtering: 60
  - Minimal spot meterset [MU/fx]: 3.0000
  - Maximal spot meterset [MU/fx]: 80
  - Meterset limit margin [%]: 0
- Beam computation settings
  - Target margins: proximal layers = 2
  - Target margins: distal layers = 2

E

The delineation of the clip

This appendix extends the delineation process of the clip. The adapted protocol for the delineation of titanium clips according to HollandPTC guidelines is by using a window/level preset of L 1600 / W 700. In order to provide accurate delineation of the clip, this preset was compared with two other presets: the bone preset L 450 / W 1600 and the soft tissue preset L 40 / W 350. Figure E.1 presents the different level/window settings for a saggital and transversal plane view. Large differences in the representation of the clip are observed for the different level / window presets. There is an indication that some presets, provide an underestimation of the actual dimensions of the clip, while others provide an overestimation. To ensure that proper delineation was performed, the different level/window presets were evaluated and the knowledge of the shape and size of the clip must be used to delineate the clip.

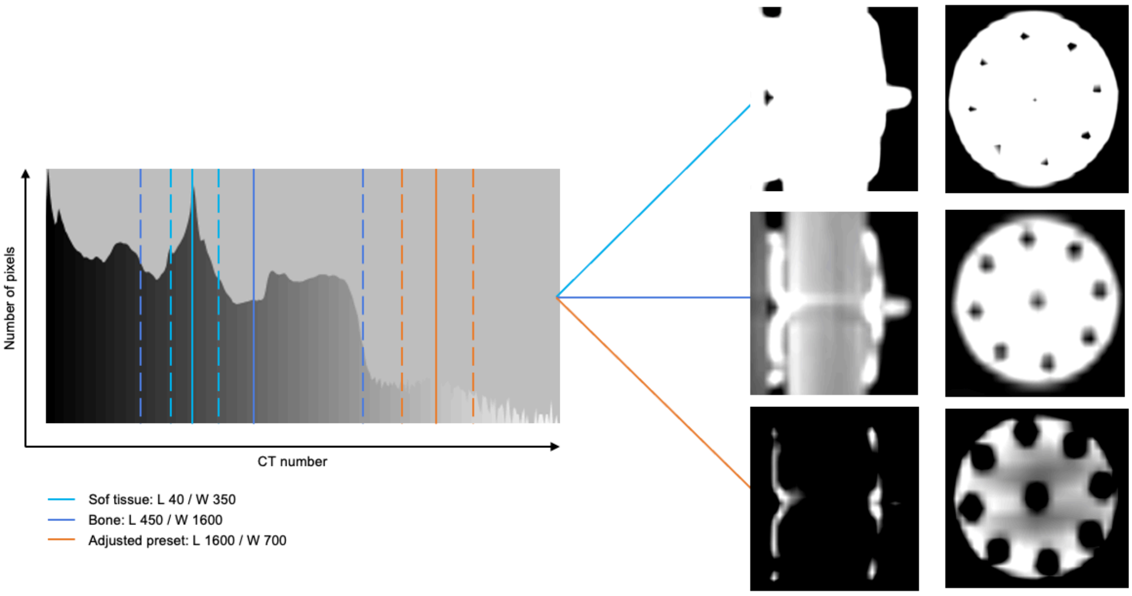

Figure E.1

F

Data processing

The location of the center of the field serves as an important tool for data analysis. Due to alignment inaccuracies during the positioning of the phantom for the experiments, it was chosen to computationally determine the center coordinates.

The center coordinates were calculated by using the built-in Matlab function ‘regionprops’. The input for this function is the region of interest. In this case, it is the part of the 2D plane in which the signal is measured. This ROI is determined by extracting the data that lies above a threshold. This is set to be 200 signal intensity values for the experimental data and 0.2 Gy for the Raystation data. The output of the function are the coordinates of the center of mass (centroid) of the ROI. The centroid is calculated as a weighted average of pixel positions within the defined ROI. The weight is based on determining if a pixel is inside or outside the defined ROI. It therefore does not directly incorporate signal intensities.

To determine whether this is a suitable method to compute the center of the field, the calculation was also performed for the Raystation data. There, the exact position of the isocenter was known: x-coordinate at 87 and y-coordinate at 174. The results are presented in Table F.2. The results show that this method determined the x- and y-coordinate of the isocenter of the Raystation data up to 1 point accurately. In addition to this, a visual assessment of the centroids projected on the 2D dose planes was performed. The 2D dose planes of the Experimental and Raystation data, for strategy 1 at all depths are presented in Figure F.1.

Based on these results, it was chosen to use this method to calculate the center coordinates. Because the experimental setup was kept constant at each depth, the average value per depth was determined, leading to the results in Table F.1.

Table F.1

Depth [mm]	Experiments Centroid X	Experiments Centroid Y	Raystation Centroid X	Raystation Centroid Y
10	285	302	87	174
30	300	302	87	174
50	295	305	87	174
60	303	306	87	174

Table F.2

Strategy	Depth [mm]	Experiments Centroid X	Experiments Centroid Y	Raystation Centroid X	Raystation Centroid Y
S1	10	284	302	87	174
S2	10	284	302	87	174
S3	10	284	302	87	174
S4	10	285	302	88	174
S5	10	285	302	88	174
S6	10	285	302	88	174
S1	30	300	303	87	174
S2	30	300	302	87	174
S3	30	299	302	87	174
S4	30	301	301	88	174
S5	30	301	301	88	174
S6	30	301	302	88	174
S1	50	295	305	87	174
S2	50	294	306	87	174
S3	50	295	305	87	174
S4	50	296	306	88	174
S5	50	296	304	88	174
S6	50	297	305	88	174
S1	60	302	305	87	175
S2	60	302	306	87	175
S3	60	302	307	87	175
S4	60	305	304	87	175
S5	60	305	305	88	175
S6	60	305	306	88	175

Figure F.1

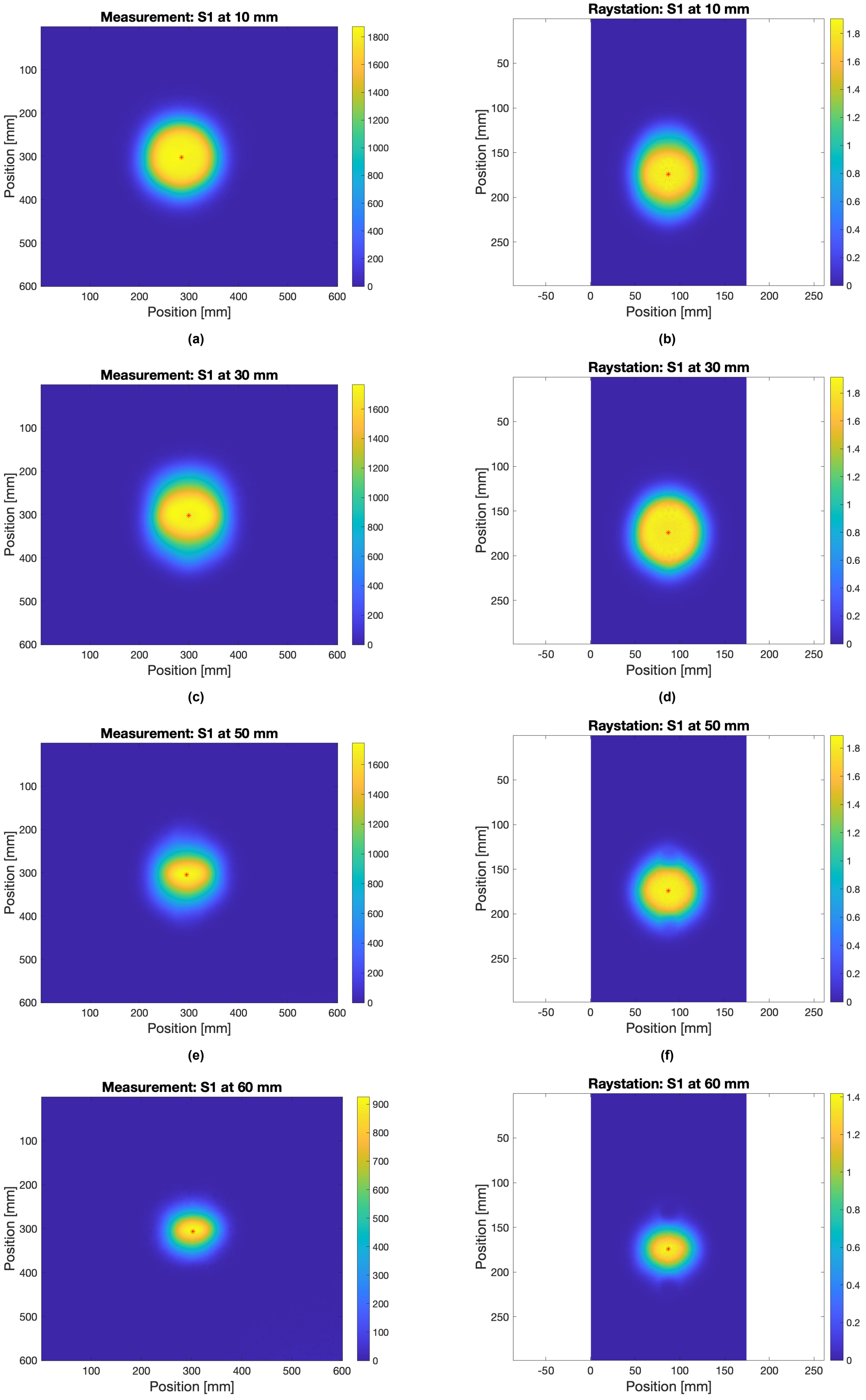

(a) (b)

(c) (d)

(e) (f)

(g) (h)

G

Experimental results: line profile through the center of field

In this appendix, an overview of the profiles, measured through the center of the radiation field along the x- and y-direction is provided for both the experimental and Raystation data. On the next page, all plots are depicted without normalization. On the page after that, all plots are normalized to their corresponding maximum value (the maximum value per line profile is used in the normalization).

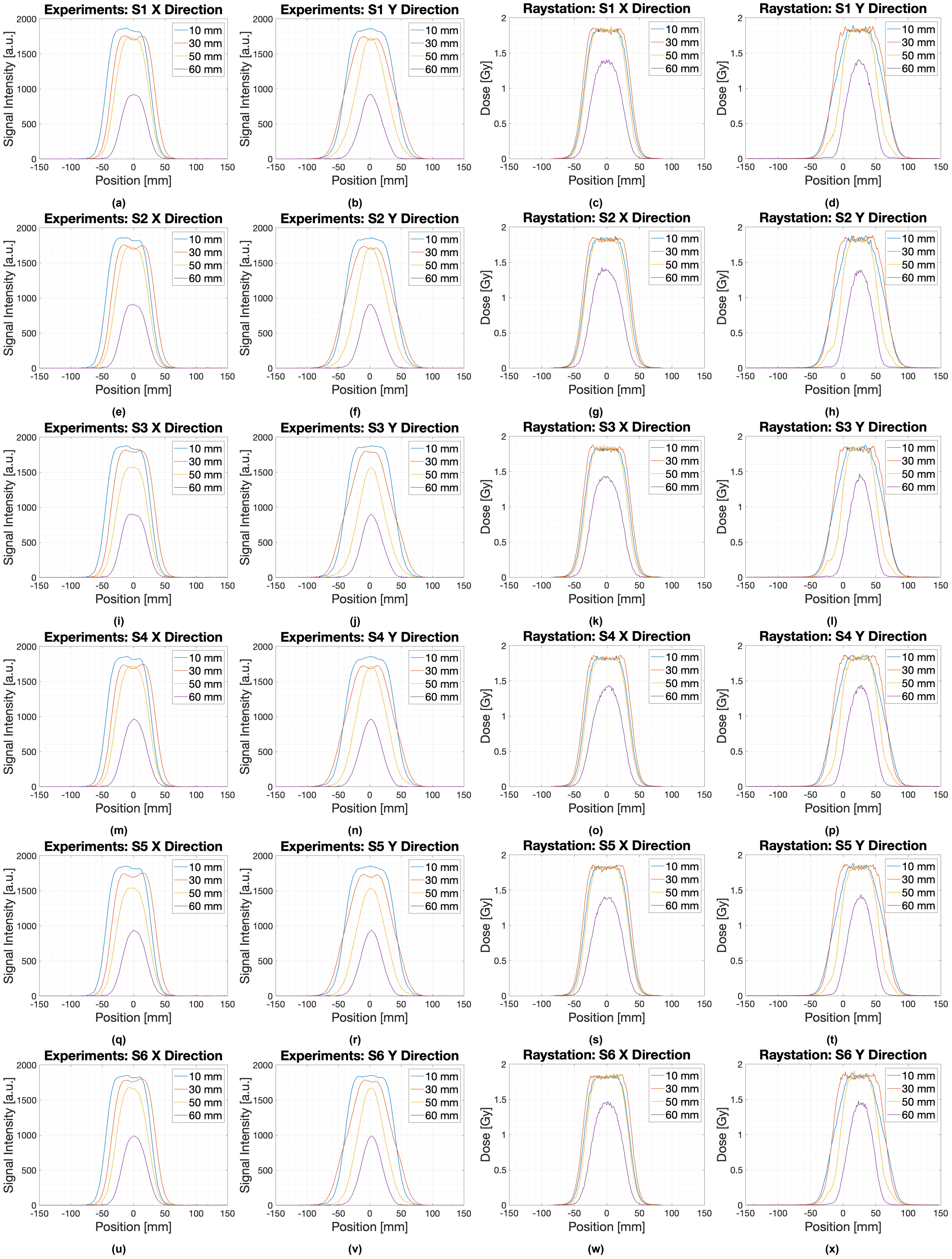

Experiments: S1 X Direction (a)

Experiments: S1 Y Direction (b)

Raystation: S1 X Direction (c)

Raystation: S1 Y Direction (d)

Experiments: S2 X Direction (e)

Experiments: S2 Y Direction (f)

Raystation: S2 X Direction (g)

Raystation: S2 Y Direction (h)

Experiments: S3 X Direction (i)

Experiments: S3 Y Direction (j)

Raystation: S3 X Direction (k)

Raystation: S3 Y Direction (l)

Experiments: S4 X Direction (m)

Experiments: S4 Y Direction (n)

Raystation: S4 X Direction (o)

Raystation: S4 Y Direction (p)

Experiments: S5 X Direction (q)

Experiments: S5 Y Direction (r)

Raystation: S5 X Direction (s)

Raystation: S5 Y Direction (t)

Experiments: S6 X Direction (u)

Experiments: S6 Y Direction (v)

Raystation: S6 X Direction (w)

Raystation: S6 Y Direction (x)

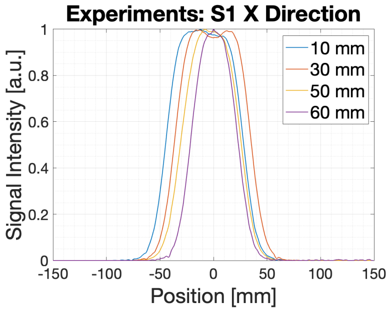

(a)

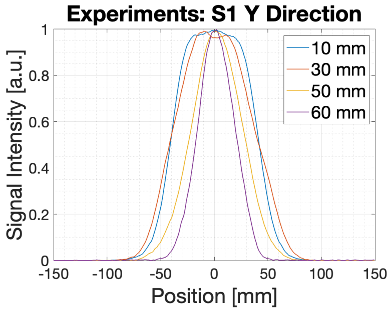

(b)

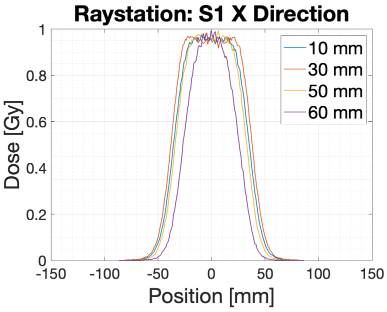

(c)

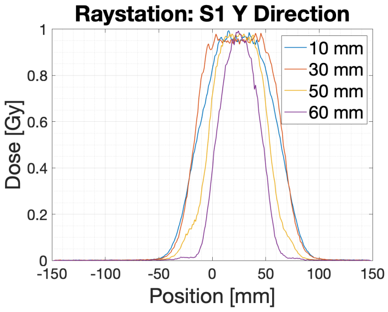

(d)

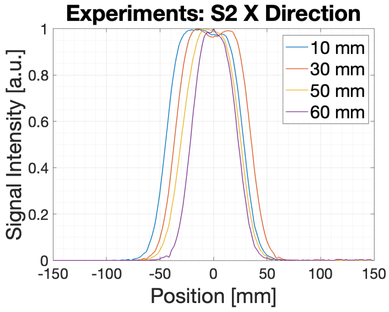

(e)

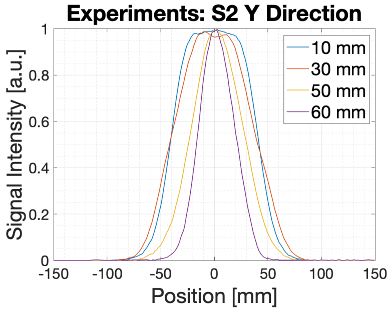

(f)

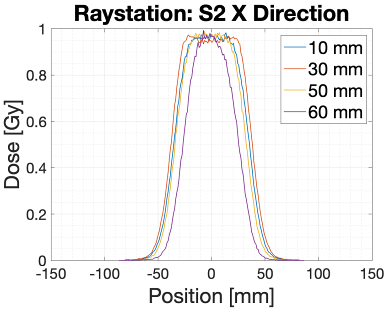

(g)

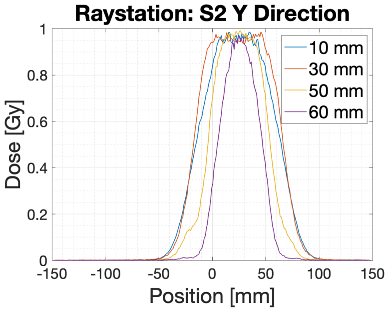

(h)

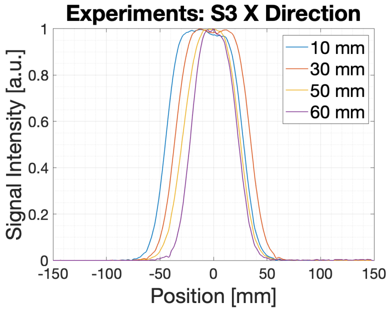

(i)

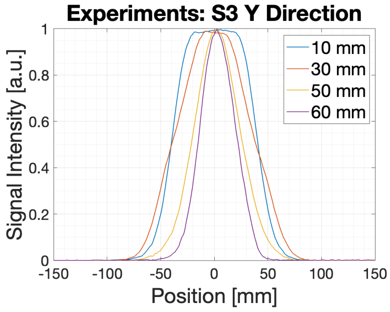

(j)

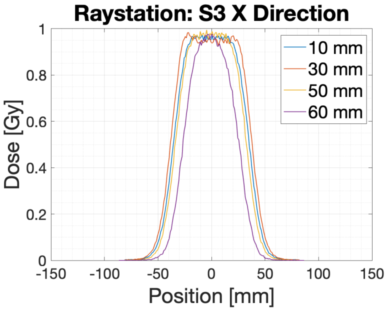

(k)

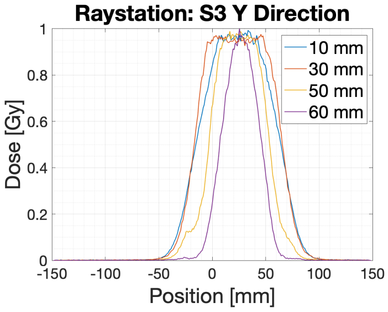

(l)

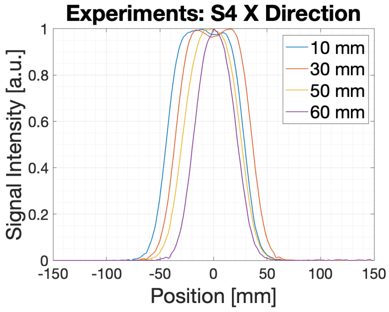

(m)

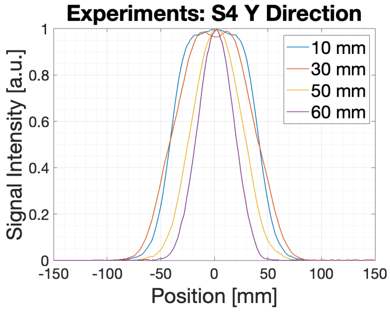

(n)

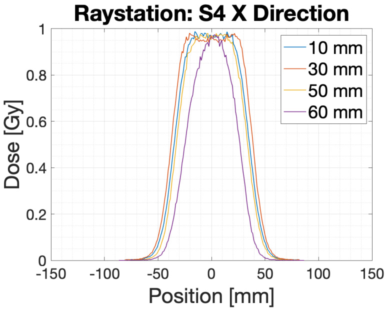

(o)

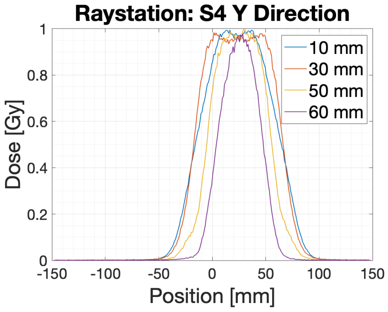

(p)

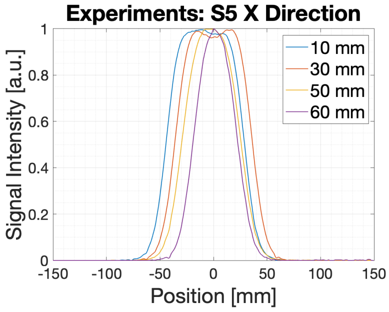

(q)

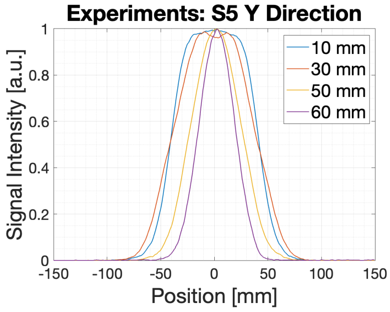

(r)

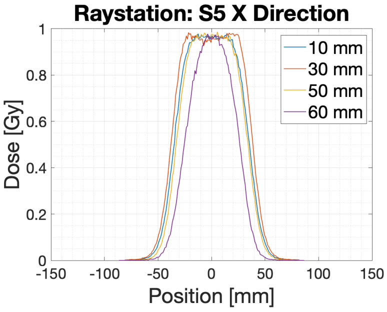

(s)

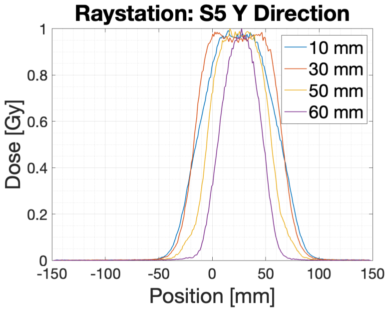

(t)

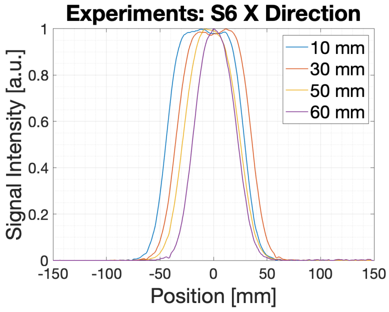

(u)

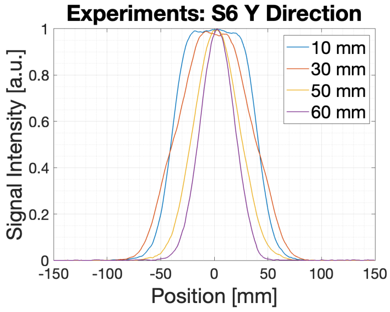

(v)

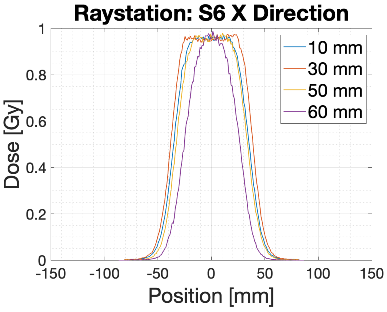

(w)

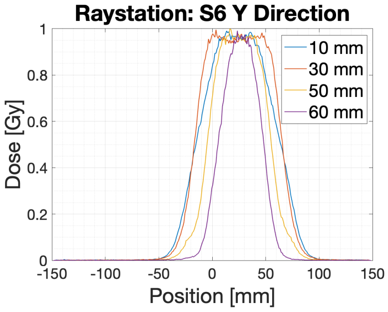

(x)

H

Experimental results: dose fall-off surrounding CTV

In addition to the CTV coverage, the treatment plans were designed based on a dose fall-off optimization function. This function is set to the external ROI and aims to minimize the dose to the tissue surrounding the CTV. In each treatment plan, the optimization function was set to optimize the dose from the high dose level, 50.4 Gy, to the low dose level, 0 Gy, over a distance of 2.7 cm. To evaluate the results regarding this optimization goal, the dose fall off over this distance was calculated at the measurement depth that overlays the CTV, i.e. at 10, 30, and 50 mm.

Since the dose is not measured in the experiments, the detected signal fall-off is compared. The signal fall-off was calculated by defining the geometrical boundaries of the CTV, just like in Section 6.3.1, and the margin surrounding the CTV. It was determined based on the line profiles that were drawn through the isocenter, in both x- and y directions. An example of a graph in which the geometrical boundaries are indicated by asterisks is presented in Figure H.1.

The signal fall-off was calculated by $\Delta y/\Delta x$, with $\Delta\ y$ being the intensity value on the CTV boundary (red asterisk in Figure H.1) minus the intensity value at the boundary of the outer margin (blue asterisk in Figure H.1), and $\Delta\ y$ being distance from CTV boundary until the end of the margin. A higher value corresponds to a steeper gradient. The signal fall-off was determined for the x- and y- line profiles, on both sides. An overview of the obtained values is presented in Figure H.3.

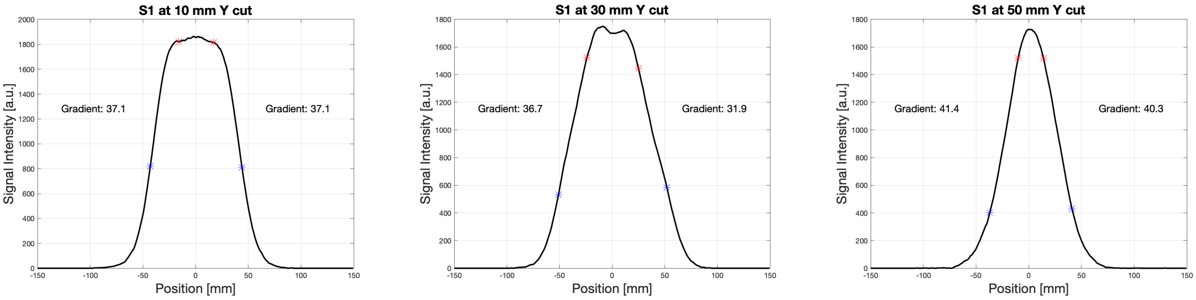

(a) (b) (c)

Figure H.1: This figure indicates how the geometrical boundaries of the CTV along the line profiles were determined. The red asterisks represent the boundaries of the CTV, whereas the blue asterisks represents the boundary of a 2.7 margin surrounding the CTV.

Figure H.2

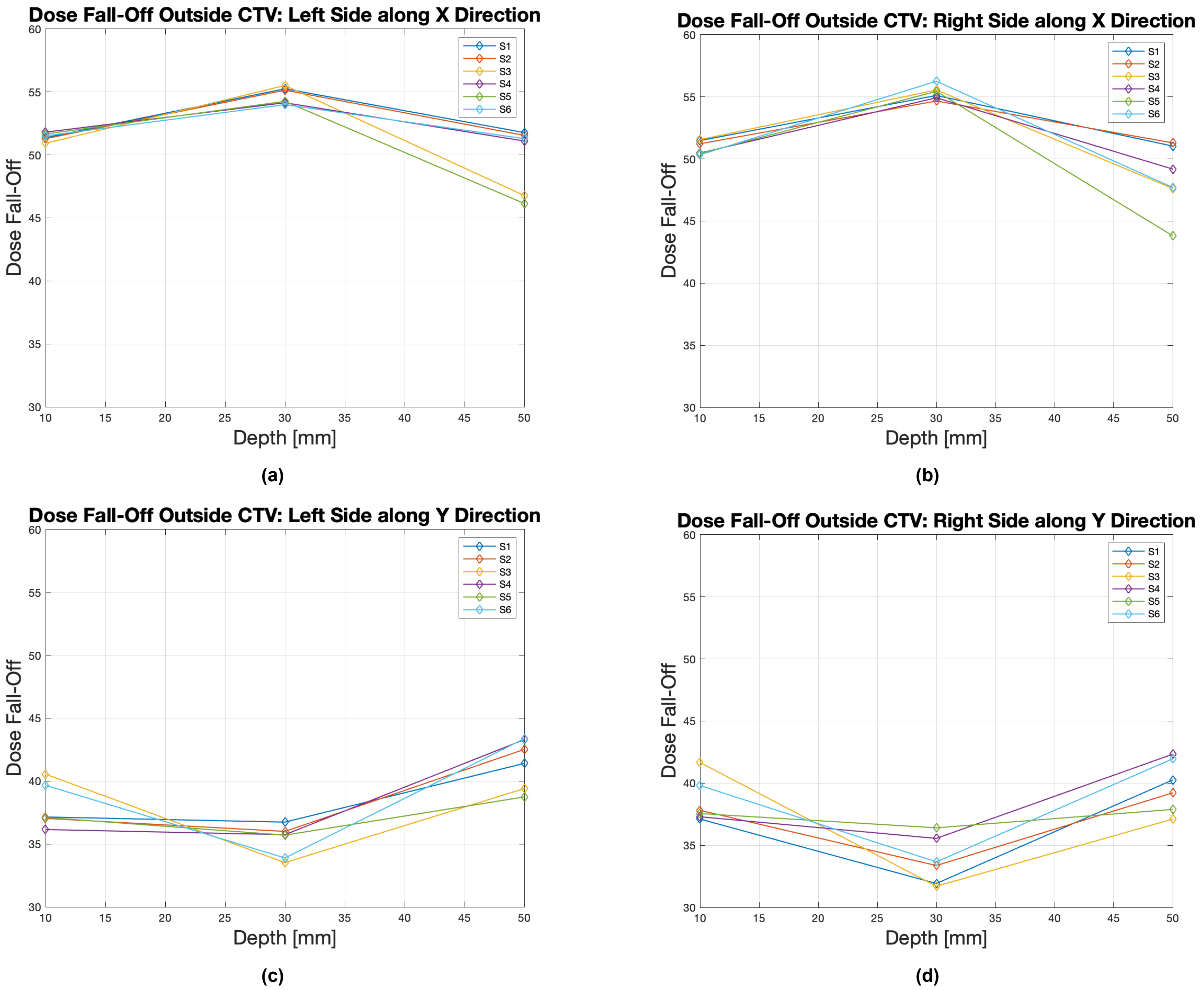

(a) (b) (c) (d)

Figure H.3: This figure provides an overview of the dose fall-off outside the CTV, calculated along the x- and y-direction.

The presented signal fall-off values provide an idea of the steepness of the lateral penumbra for each strategy. However, this metric does not incorporate the measured intensity values at the boundary sites. This is important to consider, since a steeper signal fall-off, can still result in a higher absolute measured signal.